BORON CARBIDE NANOWIRES: SYNTHESIS AND CHARACTERIZATION

by

Zhe Guan

A dissertation submitted to the faculty of
The University of North Carolina at Charlotte
in partial fulfillment of the requirements
for the degree of Doctor of Philosophy in
Mechanical Engineering

Charlotte

2013

Approved by:

_____
Dr. Terry Xu

_____
Dr. Qiuming Wei

_____
Dr. Thomas Schmedake

_____
Dr. Thomas Lucas

ABSTRACT

ZHE GUAN. Boron carbide nanowires: synthesis and characterization. (Under the direction of DR. TERRY XU)

Bulk boron carbide has been widely used in ballistic armored vest and the property characterization has been heavily focused on mechanical properties. Even though boron carbides have also been projected as a promising class of high temperature thermoelectric materials for energy harvesting, the research has been limited in this field. Since the thermal conductivity of bulk boron carbide is still relatively high, there is a great opportunity to take advantage of the nano effect to further reduce it for better thermoelectric performance. This dissertation work aims to explore whether improved thermoelectric performance can be found in boron carbide nanowires compared with their bulk counterparts.

This dissertation work consists of four main parts. (1) Synthesis of boron carbide nanowires. Boron carbide nanowires were synthesized by co-pyrolysis of diborane and methane at low temperatures (with 879 °C as the lowest) in a home-built low pressure chemical vapor deposition (LPCVD) system. The CVD-based method is energy efficient and cost effective. The as-synthesized nanowires were characterized by electron microscopy extensively. The transmission electron microscopy (TEM) results show the nanowires are single crystalline with planar defects. Depending on the geometrical relationship between the preferred growth direction of the nanowire and the orientation of the defects, the as-synthesized nanowires could be further divided into two categories: transverse fault (TF) nanowires grow normal to the defect plane, while axial fault (AF) ones grow within the defect plane. (2) Understanding the growth mechanism of as-

synthesized boron carbide nanowires. The growth mechanism can be generally considered as the famous vapor-liquid-solid (VLS) mechanism. TF and AF nanowires were found to be guided by Ni-B catalysts of two phases. A TF nanowire is lead by a hexagonal phase catalyst, which was proved to be in a liquid state during reaction. While an AF nanowires is catalyzed by a solid orthorhombic phase catalyst. The status of a catalyst depends mainly on temperature. (3) Observation of “invisible” defects in boron carbide nanowires. The planar defects can only be seen under a transmission electron microscope when the electron beam is within the defect plane. Furthermore, there are only two directions within that plane, along which the orientation of defect can be told and clear TEM results can be taken. The challenge is that the TEM sample holder is limited to tilt ±30° in each direction. A theory was developed based on lattice calculation and simulation to tell the orientation of defect even not from those unique directions. Furthermore, it was tested by experimental data and proved to be successful. (4) Preliminary exploration of structure-transport property of as-synthesized boron carbide nanowires. In collaboration with experts in the field of thermal science, thermal transport properties of a few boron carbide nanowires were studied. All measured nanowires were either pre-characterized or post-characterized by TEM to reveal their structural information such as diameter, fault orientations and chemical composition. The obtained structural information was then analyzed together with measured thermal conductivity to establish a structure-transport property relation. Current data indicate that TF ones have a lower thermal conductivity, which is also diameter-dependent.

ACKNOWLEDGEMENTS

I would like to express my deepest appreciation to my advisor, Dr. Terry Xu. Her attitude about academic integrity is a good example to the students. Being a professor who truly cares about her students, she taught me not only how to operate the equipments, but also how to summarize data, manage time, and make plans. She helped me to develop those good habits that can benefit me throughout my whole career. I would like to thank Dr. Haitao Zhang for his generous help on the training of various equipments. I also want to express my gratitude to Dr. Jon Merkert, Dr. Lou Deguzman, and Dr. Alec Martin. Without their help on the characterization tools, this work cannot move on smoothly. I am grateful to our collaborators, Dr. Deyu Li's group, in Vanderbilt University. The micro-device they developed makes it possible to study the structure and property on the same nanowires. I am thankful to my groupmates Dr. Baobao Cao, Dr. Xiaoxia Wu, Youfei Jiang, and Dr. Timothy Gutu for their help and efficient cooperation.

The equipments supplied by Center of Optoelectronics and Optical Communications and mechanical engineering at UNC Charlotte are gratefully acknowledged. I would like to thank the electron energy loss spectroscopy (EELS) provided by University of South Carolina. I appreciate the funding supplied by Graduate & Professional Student Government (GPSG) and National Science Foundation (NSF).

Most importantly, I want to thank my parents who trust and support me all the time. At last, I appreciate the time I spent with my friends at Charlotte.

TABLE OF CONTENTS

CHAPTER 1: INTRODUCTION

This dissertation work is motivated by the idea that boron carbide nanowires could be promising high temperature thermoelectric materials with enhanced thermoelectric performances compared to their bulk counterparts. The main objectives of the work are to synthesize boron carbide nanowires, perform thorough materials characterization on as-synthesized nanowires, explore their growth mechanisms to facilitate future controlled synthesis, and obtain preliminary results on structure-transport property relations.

In this chapter, background information on the need of better thermoelectric materials in current energy-related research, research status on the thermoelectric properties of bulk boron carbides, and how boron carbide nanowires can have improved thermoelectric properties are reviewed and discussed.

1.1 Energy Overview

Energy is related to our daily lives, since it is needed to keep facilities running everywhere. According to the "Annual Energy Review 2010",[1] the energy consumption is in an uptrend from 1949 to 2010 (Figure 1), and most of the energy consumption comes from the traditional energy (petroleum, coal, and natural gas). The major problems with the fossil fuels are that they are not renewable and the resultant environmental issues, such as global warming and air pollution. Although nuclear energy has been widely used to provide electric power, there are still some concerns about the safety of the nuclear

power plants, since the generated high-level radioactive wastes are stored individually in each nuclear plant and keep accumulating.

Renewable energy is the solution for the potential energy crisis. But the total energy consumption from all kinds of renewable energy currently only makes up a small portion (~8%). The good thing is that there is a high growth rate globally for the wind and solar energies within this decade due to the improved technology and increased power plant installations.[2,3]

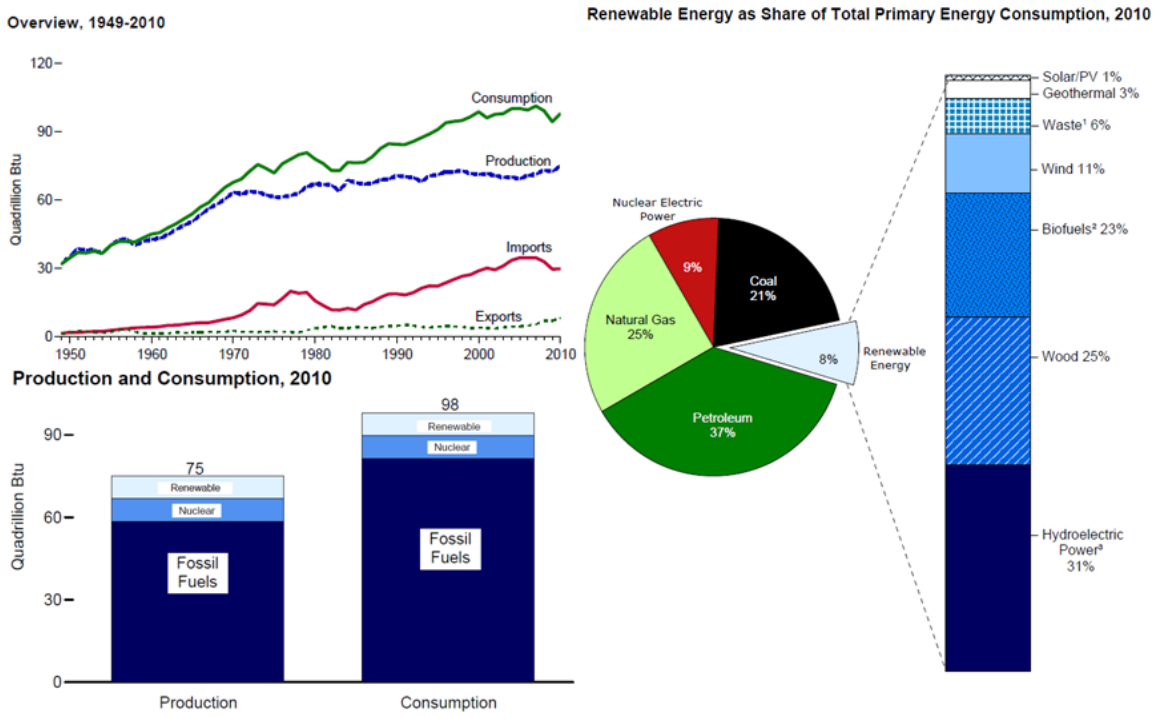

Figure 1.1 Energy consumption in the year of 2010 within United States.[1]

1.2 Thermoelectric Effect

1.2.1 Background

In addition to energy sources shown in Figure 1, heat can also be used to generate electricity due to the Seebeck effect, which is one of the thermoelectric effects, discovered by Thomas Seebeck in 1821. He noticed that the compass needle was deflected when one junction of the circuit made of two dissimilar metals was heated.[4] This phenomenon indicates a current flow through the metals. The voltage produced was found to be proportional to the temperature difference between the junctions.

$$V = S\Delta T = S(T_h - T_c) \tag{1.1}$$

where S is the Seebeck coefficient, T_h and T_c are the temperatures from the hot and cold junctions, respectively.

In 1843, Jean Peltier found that the temperature would change if current was applied through two dissimilar metals.[5] This Peltier effect is the reverse of Seebeck effect. And a comprehensive explanation was given by Lenz in 1838, showing that heat could be absorbed or released at the junction depending on the direction of the current flow through two metals.[6] Similar to the Seebeck effect, the heat change is proportional to the current flow and the coefficient is known as the Peltier coefficient.

Based on the Seebeck effect and the Peltier effect, William Thomson predicted and observed that when there is a current flow in a homogeneous material with a temperature gradient, heat could be absorbed or released. The heat change is proportional to the current and temperature gradient. This is known as the “Thomson effect”.[7]

Later, it was Edmund Altenkirch who established the initial theory of thermoelectric effects for electric generator and refrigerator between 1909 and 1911.[8,9] It

was believed that in addition to a large Seebeck coefficient, a good thermoelectric material should have a high electrical coefficient to minimize Joule heating and a low thermal conductivity to maintain the temperature difference. According to Wiedemann-Franz Law, at a given temperature the ratio of the electrical conductivity to the thermal conductivity of a metal is a constant. It is the free electrons that contribute to the electrical conductivity and most of the thermal conductivity in metals. For semiconductors, the thermal transport is realized by lattice vibration or "phonon". Thus, a higher Seebeck coefficient is the only thing that needs to be considered for thermoelectric applications based on metals. However, there are more choices for the case of semiconductors since the ratio of the electrical conductivity to the thermal conductivity can be altered.

After tens of years' study on semiconductor thermoelectric materials, aiming at improving the thermoelectric performance, Abram Ioffe developed the famous concept "figure of merit" to evaluate the convention efficiency of a thermoelectric material. The figure of merit, *Z*, can be presented in the equation below.

$$Z = \frac{S^2\sigma}{\kappa} \tag{1.2}$$

in which σ and κ are the electrical conductivity and the thermal conductivity, respectively. Since the unit of Seebeck coefficient is volts per Kelvin ($V \cdot K^{-1}$), the term figure of merit, *Z*, has units of reciprocal Kelvin (K^{-1}) and its value varies with temperature. Therefore, the nondimensional figure of merit *ZT* is more widely used. A good thermoelectric material is expected to have a higher *ZT* value (>3).

When a device is built based on thermoelectric materials, the efficiency of the device needs to be taken into consideration. A simplified case, when S, σ, κ, and Z are not dependent on temperature, the maximum efficiency can be written as[10]

$$\eta = \frac{\Delta T}{T_h} \cdot \frac{\sqrt{1 + Z\bar{T}} - 1}{\sqrt{1 + Z\bar{T}} + T_c/T_h} \tag{1.3}$$

where T_h and T_c are the temperatures at the hot end and cold end, respectively. $\bar{T}$ is the average temperature, $\bar{T} = (T_h + T_c)/2$. Like other engines, the efficiency is limited by the Carnot efficiency, $\Delta T/T_h$, and a larger temperature difference is preferred. More importantly, the selection of materials also determines the overall efficiency. The materials for hot and cold ends need to be selected in such a way that the temperatures at which their maximum figure of merit values can be found are greatly different. Also, there is another term when there is a large temperature called compatibility factor

$$s = \left(\sqrt{(1 + ZT)} - 1\right)/ST \tag{1.4}$$

It means the transport of electrons and phonons could react differently when there is a huge temperature gradient. This factor should not change too much with temperature for the hot and cold end materials. Otherwise, the overall efficiency of the device might be reduced.

So far, some common applications of the thermoelectric materials are thermocouples, generators (Seebeck effect), or coolers/heaters (Peltier effect). Thermoelectric generators have been used in vehicles to convert the waste heat into electricity in order to increase the fuel efficiency. Another type of thermoelectric generator called radioisotope thermoelectric generator (RTG) captures the heat produced

from the radioactive decay. It is mostly used in the spacecraft or satellites due to the long life span of the radioactive source material.

1.2.2 Thermoelectric Materials

The main concern on thermoelectric materials is to have a higher *ZT* value. A large *S* is favorable, so that the generated voltage will be large at a given temperature difference. A large σ is needed to prevent the Joule heating, which can heat up the cold side of the thermoelectric device. A lower κ will be helpful to maintain the temperature difference at both ends.

Due to the low electrical conductivity, insulators are not a good choice as for thermoelectric applications. Metals have good electrical conductivity, but low Seebeck coefficient. Also the electrical conductivity is proportional to the thermal conductivity according to the Wiedmann-Franz law. That leaves less room for improving the *ZT* value of metals. However, in semiconductors thermal conductivity comes from the contribution from both electrons (κ_e) and phonons (κ_p). The major part κ_p is not proportional to electrical conductivity, providing more options to enhance the *ZT*. Therefore, most of popular thermoelectric materials are found to be semiconductors.

Figure 1.2 shows the dependence of each parameter on carrier concentration. It can be seen that the increasing σ will lead to a lower *S* and a higher κ as well. So a compromise needs to be reached if we want to maximize the *ZT* value. The ideal situation is to find the maximum power factor ($S^2\sigma$) while keeping a lower κ, especially the contribution from the phonon part.

Slack came up with the idea of “phonon-glass electron-crystal” (PGEC).[11] That means the material acts like a crystal for the electron transport while having a low

thermal conductivity like the glass. Since κ_p does not change along with other parameters, finding a lower thermal conductivity becomes an effective way to enhance the *ZT* value. To reduce the lattice thermal conductivity, it is necessary to increase phonon scattering by complex unit cells,[12] point defect,[13,14] rattling atoms,[15] or boundaries.[16]

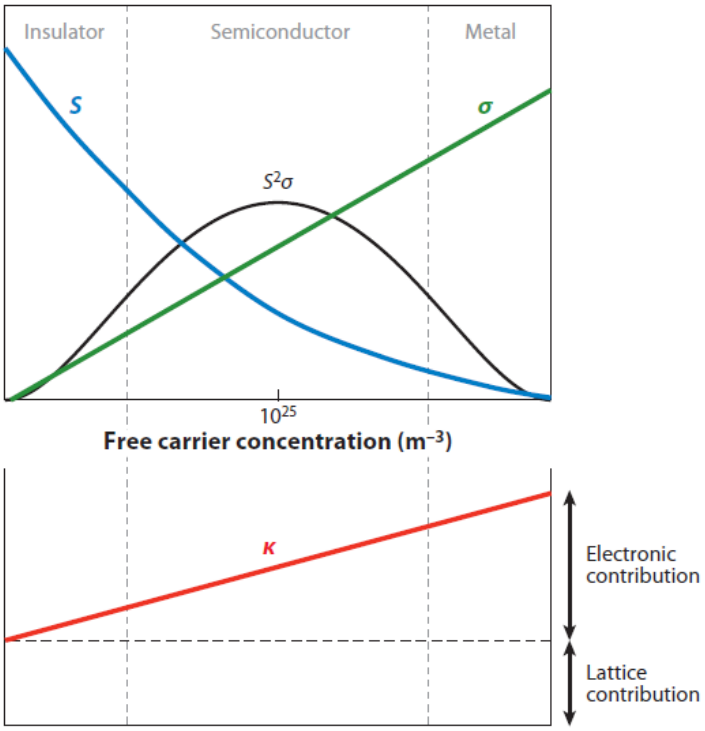

Figure 1.2 Dependence of Seebeck coefficient (S), electrical conductivity (σ), power factor ($S^2\sigma$), and thermal conductivity (κ) on the carrier concentration.[17]

The widely studied traditional thermoelectric materials include bismuth telluride (Bi_2Te_3), antimony telluride (Sb_2Te_3), lead telluride (PbTe), silicon germanium (SiGe), and their alloys. As shown in Figure 1.3, the maximum *ZT* values for those traditional thermoelectric materials are close to 1. This *ZT* value is too low to have them

commercialized, and it has to be at least about 4 to be comparable to other technologies.[18] However, progress of enhancing *ZT* is quite slow in the 20th century.[19] It was the quantum effect that inspired the studies of low-dimensional thermoelectric materials, which leads to the breakthrough of *ZT*.

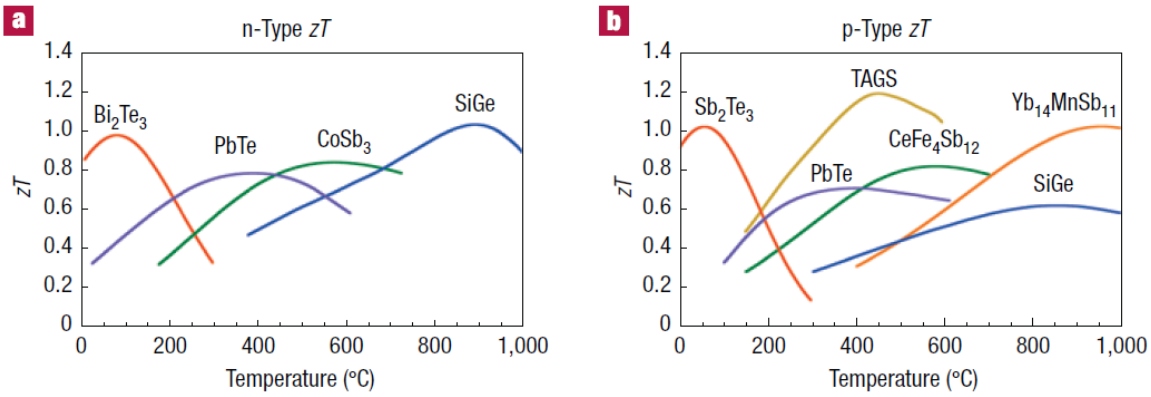

Figure 1.3 Figure of merit values from typical thermoelectric materials.[20]

1.2.3 Advantages of Low-Dimensional Thermoelectric Materials

It was first predicted theoretically by Hicks et al. that the increase of figure of merit could be achieved by using a quantum well or superlattice (SL).[21,22] The quantum effect helps to enhance the figure of merit in two ways. First, it increases of Seebeck coefficient[23] due to the increased density of states (DOS) near the Fermi level.[24,25] Second, the additional layers will provide more phonon scattering boundaries to reduce thermal conductivity.[21] Ideally, if the quantum width is smaller than the phonon's mean free path and larger that the electron's mean free path, a reduced thermal conductivity can be expected without affecting the electrical conductivity.[19] Later, Hicks et al. were able to support their theory by fabricating a PbTe/$Pb_{1-x}Eu_xTe$ quantum well.[26]

Since there are different transport properties within the superlattice, its in-plane (along the film plane)[27-31] and cross-plane (perpendicular to the film plane)[27] thermoelectric performances have been studies. Calculation shows that phonon scattering mechanisms are different in those two cases.[32] Experimental data based on Si/Ge superlattice indicates that from the cross-plane direction both thermal conductivity and electrical conductivity are much lower compared with that from in-plane direction.[33] However, study based on superlattice made up by Bi_2Te_3/Sb_2Te_3 shows that the cross-plane electrical conductivity can be comparable to the in-plane value, depending on the layer thickness and superlattice period. Meanwhile, the cross-plane thermal conductivity is lower than the in-plane value, giving the lowest κ_p=0.22 $Wm^{-1}K^{-1}$.[27] Other work focusing on the decrease of thermal conductivity by superlattice structures have been reported on GaAs/AlAs[34] and Si/Ge.[35] However, there are still other concerns about superlattice structures, such as thermal current through barrier layers and tunneling effect, which will reduce figure of merit of superlattice.[36]

Hicks et al. also predicted that when the dimension goes down to one-dimensional materials or quantum wires, figure of merit could be improved, depending on the width of the nanowire.[21,37] According to the thermoelectric measurements on silicon nanowires, the increased figure of merit is mainly attributed to the dramatically reduced thermal conductivity.[38,39] The fabrication of "superlattice nanowires"[40,41] provides more options for the design of material structure to achieve an even smaller thermal conductivity. The nature of superlattice nanowire can be considered as an elongation of superlattice in the cross-plane direction while with quantum confinement in two in-plane directions. Thus, it is reasonable to expect that superlattice nanowires will have a lower thermal conductivity

than those common 1D and 2D thermoelectric materials. Although the calculated thermal conductivity from superlattice nanowires shows big reductions,[42,43] systematic experimental measurements are needed to figure out the structure-property relationship.

1.2.4 Summary

All the efforts of studying thermoelectric materials focus on improving the efficiency or increasing the *ZT* value. Basically, researches in this field are heading to two directions. Finding new materials (or alloys and composites) is one way. Although the highest *ZT* for bulk materials is around 1, there is something in common for those materials. That is the lower thermal conductivity.[20] Thus, ideas such as alloying, complex unit cells or extra boundaries seem to be the guide, as discussed in section 1.2.2. The other way, apparently, is based on the nano effect. People have found greatly improved *ZT* values (~3.5 at 575 K for PbSeTe/PbTe quantum dot superlattice,[44] ~2.4 at 300 K for Bi_2Te_3/Sb_2Te_3 superlattice,[27] and ~2.2 at 800 K for bulk $AgPb_mSbTe_{2+m}$[45]) by the means of nano effect. However, the mechanism of the improvement has not been fully explored. That leaves us the opportunity to discover how the improved *ZT* value depends on the various structures (defects or diameters of the nanowires) of the same material.

1.3 Bulk Born Carbides as Promising High Temperature Thermoelectric Materials

Boron carbide (B_4C) is usually used as armor or neutron absorber, but its potential application as a high-temperature thermoelectric material has drawn more attention recently.[46-50] It has been predicted that a much higher figure of merit value ($ZT>>1$) could be achieved.[46] This good thermoelectric performance comes from the unique structure of boron carbide.

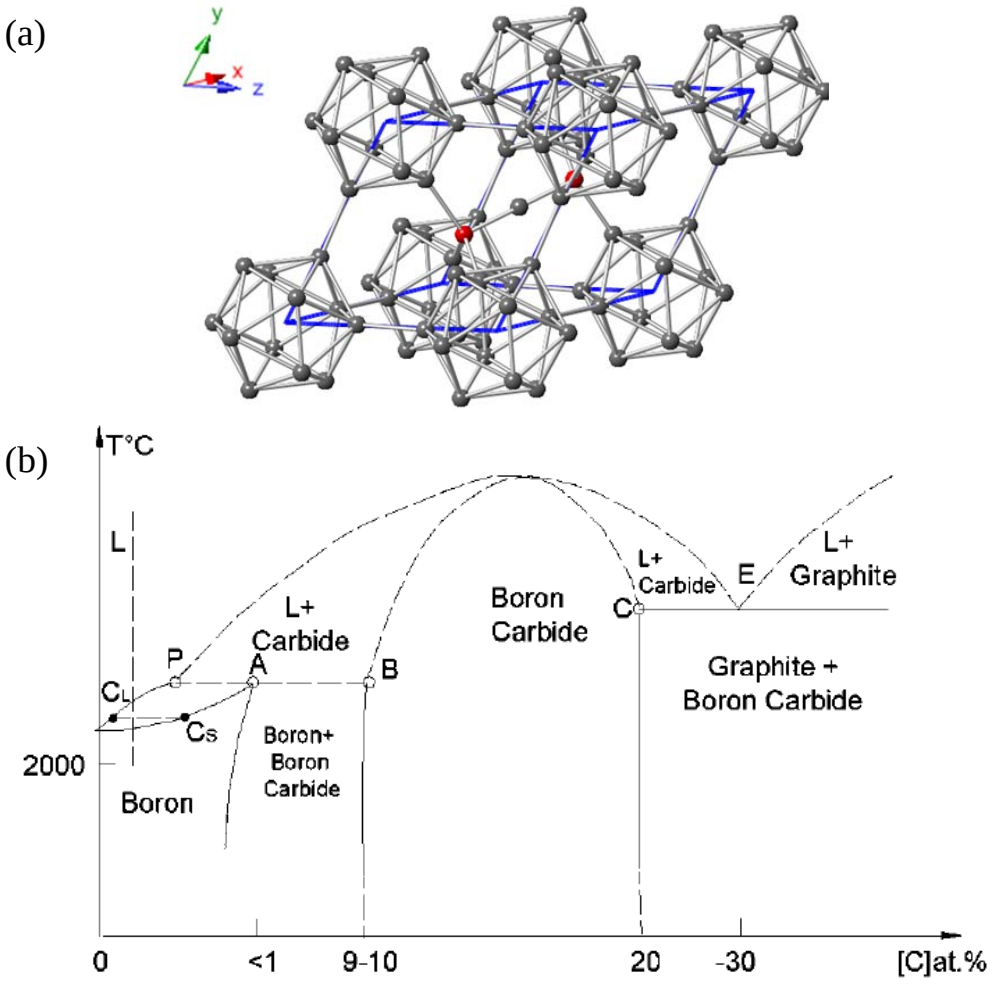

Figure 1.4 (a) Rhombohedral unit cell of boron carbide. (b) Phase diagram of boron carbide.[51]

As shown in Figure 1.4 (a), B_4C has a rhombohedral unit cell with a twelve-atom icosahedron at each corner and a C-B-C chain at the longest body diagonal.[52] It is generally believed that there are eleven boron atoms and one carbon atom in each icosahedron. Since the icosahedra are shared by eight neighbor unit cells, the contribution for each unit cell comes from one icosahedron ($B_{11}C$) and the C-B-C chain. That is why the chemical formula of boron carbide is written as B_4C (or $B_{12}C_3$). However, boron

carbide also has a wide range of composition variation with carbon atomic percentage from 8.8% to 20%.[52] The boron-carbon phase diagram is given in Figure 1.4 (b). This composition disorder is due to the replacement of carbon atoms by boron within the C-B-C chain. As carbon concentration decreases, the chain becomes C-B-B or B-B-B.[50,52-54] Further carbon reduction can be achieved by replacement within the icosahedra, leading to the unit cell with B_{12} icosahedra and a C-B-B chain.[53,54]

1.3.1 Seebeck Coefficient of Boron Carbide

Since boron carbide is a p-type semiconductor, the Seebeck coefficient is positive within its composition variation range. Studies of Seebeck coefficient have been focused on its relationship with temperature and composition.[46,47,49,55,56] As shown in Figure 1.5, the Seebeck coefficient increases with temperature when temperature is lower, but the effect of temperature is not consistent at higher temperatures.[49] It is generally large (above 100 μV/K) at room temperature and the highest value can reach ~300 μV/K. Within the composition range, the lowest Seebeck coefficient can be found around 13.3% atomic percent of carbon ($B_{13}C_2$).[47,56] But it was also reported that the dependence of temperature is not clear based on the measurement on single crystalline boron carbide.[57]

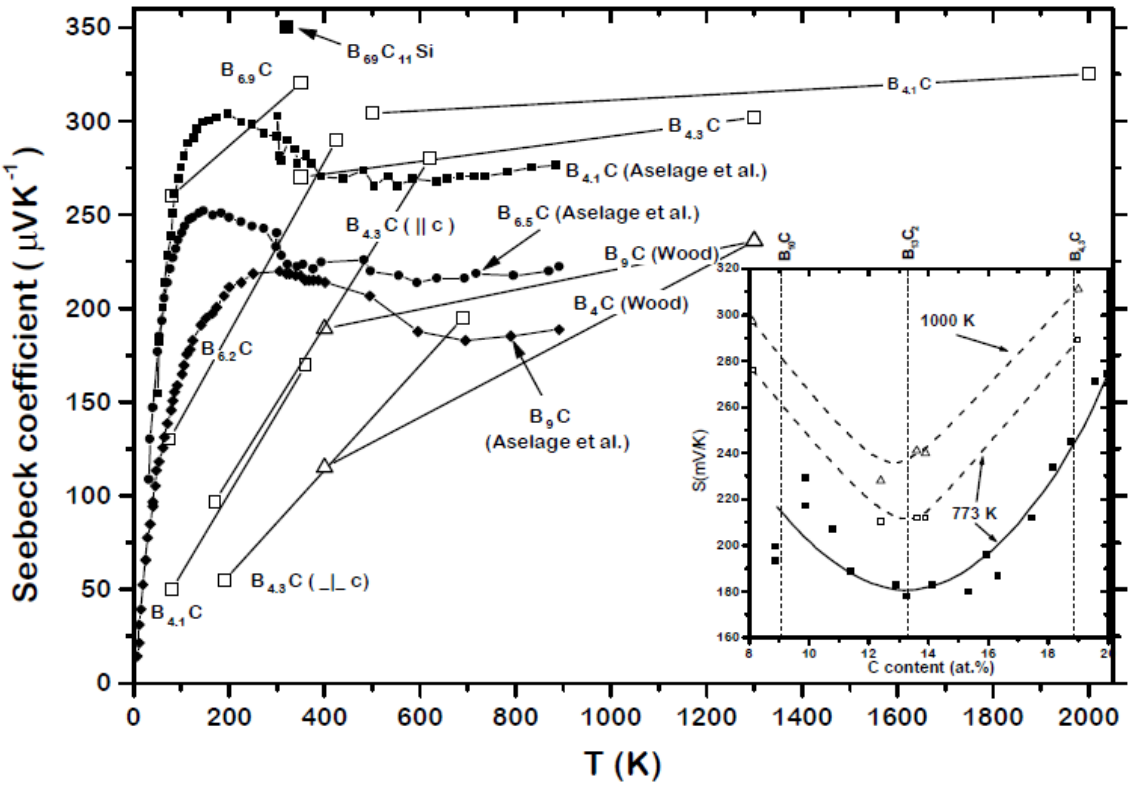

Figure 1.5 Summary of Seebeck coefficient with different temperature and carbon concentration.[49]

1.3.2 Electrical Conductivity of Boron Carbide

The electrical conductivity mechanism of boron carbide has been widely studied.[50,55,58-61] Interests on the transport properties come from the fact that its electrical conductivity increases with temperature and the intrinsic composition variation. There are mainly two mechanisms debating with each other: “small polaron hopping” mechanism brought up by Wood and Emin,[61] and Werheit’s theory with emphasis on defects.[58-60]

The carriers are considered as small polarons, and they move by hopping between carbon-containing icosahedra ($B_{11}C$). The dependence of electrical conductivity on temperature is not Arrhenius-type at lower temperatures, and it is sensitive to

composition variation. However, it becomes Arrhenius-type relation when temperature goes up and the activation energy (~0.16 eV) is reached.[50,55,61]

$$\mu \propto T^{-1}\exp(-E_A/kT) \quad (1.3)$$

where μ is the mobility and E_A is the activation energy. It was mentioned that the highest conductivity with weakest temperature dependence was found within $B_{13}C_2$ (13.3% carbon).[47,55]

However, Werheit disagreed with the polaron theory.[59] He emphasized the fact that there are lots of intrinsic defects (*e.g.*, twins and stacking faults) within boron carbide, which leads to a high electron deficiency in the conduction band. He mentioned that Wood's theory was based on an idealized crystal structure that does not exist. Werheit's theory has considered the effect of defects and the resulting localized levels above valence band.

Clearly, more work needs to be done experimentally and theoretically to discover the electrical transport mechanism of boron carbide.

1.3.3 Thermal Conductivity of Boron Carbide

As mentioned in the previous section, thermal conductivity comes from two parts. First, heat can be transported with carrier flow. In the case of Wood's polaron hopping theory, heat is conducted when carriers are "hopping" between the icosahedra. However, it was pointed out that the contribution of this part is smaller than that from the second part, lattice contribution.[62]

The dependence of thermal conductivity on temperature and composition is plotted in Figure 1.6. With a higher carbon concentration ($B_{4.1}C$), the thermal conductivity decreases with increasing temperature. However, in the other three cases,

when carbon concentration is reduced, thermal conductivity becomes much lower, and it is not sensitive to temperature anymore. This phenomenon was explained by assuming main contribution of thermal conductivity comes from the lattice vibration through the 3-atom chain.[53,62] Given that the C-B-B chain, resulting from the reduction of carbon concentration, is softer than the C-B-C chain, the disorder can lead to the lower thermal conductivity.

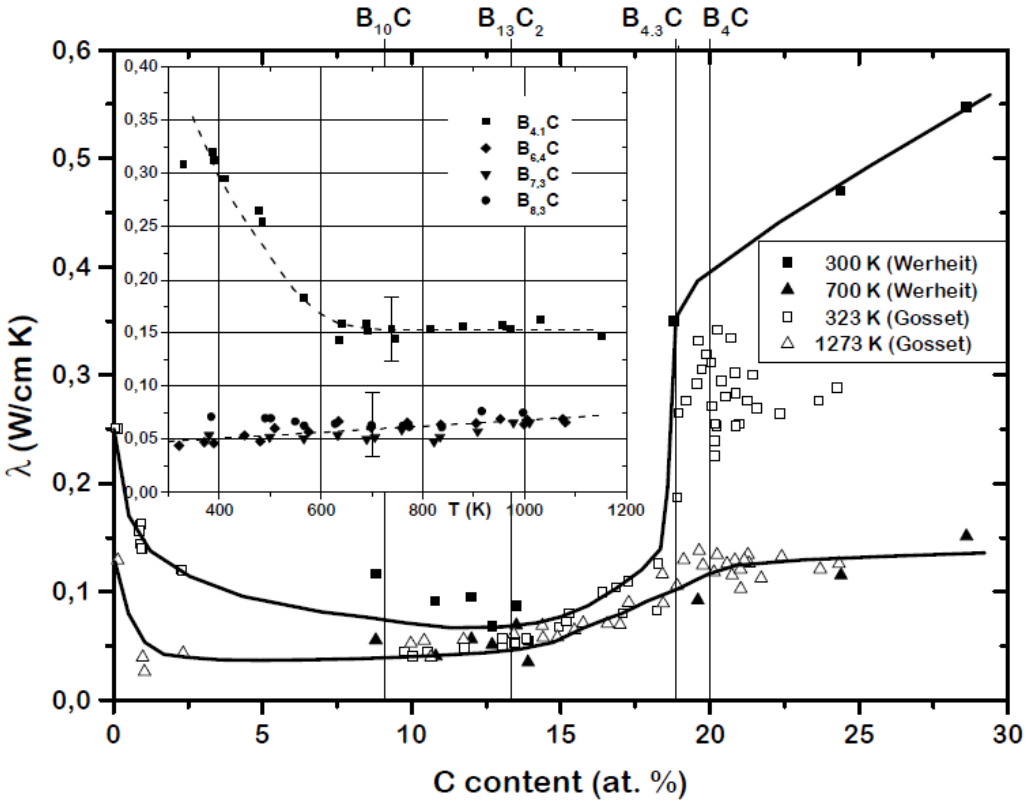

Figure 1.6 Dependence of thermal conductivity on temperature and carbon concentration.[49]

1.3.4 Thermoelectric Properties of Boron Carbide

As discussed above, boron carbide has a thermally activated electrical conductivity, a large Seebeck coefficient, and a low thermal conductivity. As a result, boron carbide has a large figure of merit (*ZT*), especially at high temperatures (*ZT*> 1 at 2000 K), as plotted in Figure 1.7.

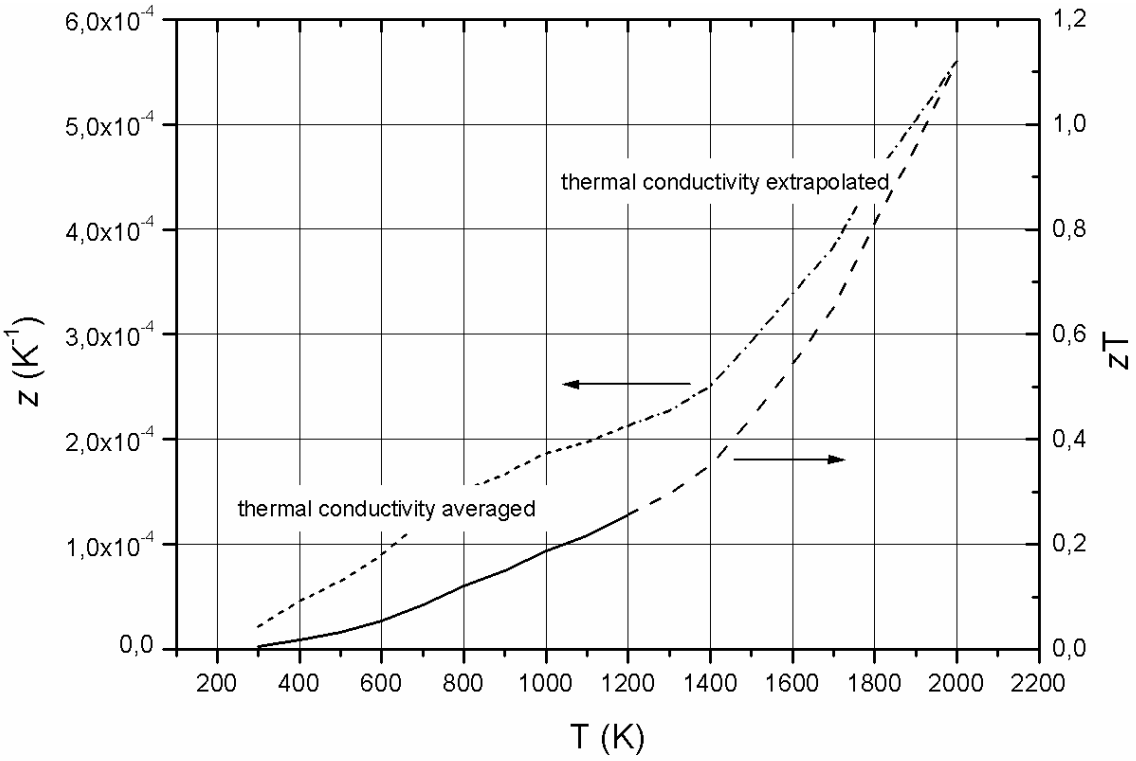

Figure 1.7 The plot of *Z* and *ZT* with temperature. The value below 1200 K was calculated based on experimental data, while the value above 1200 K was linearly extrapolated.[49]

1.3.5 Intrinsic Planar Defects within Boron Carbide

Planar defects such as twins and stacking faults are easily formed within bulk boron carbide or particles.[63-76] Detailed information about planar defects was revealed by Mackinnon *et. al.* via HRTEM images.[68,69] It is clear from their HRTEM images and diffraction patterns that there are extensive twins with $(001)_r$ (*r* represents the rhombohedral index) being the defect plane. The high defect density can be proved by the short twin widths, from ~0.9 nm to ~16.7 nm and the streaks in the diffraction pattern.[68] Twins can be observed from boron carbides synthesized by hot-pressing,[68,69] spark plasma sintering,[71,72] high temperature heating,[73] hot extrusion,[74] and pulsed electric current sintering.[75,76] It is obvious that the twins can show up no matter which synthesis method is used. The reason for the intrinsic twins in $(001)_r$ plane is that the it is the closed-packed plane with lowest energy. It was suggested that the density of twins would be reduced by increasing synthesis temperature up to 2100 °C from 1300 °C.[72] The presence of twin planes may further reduce the thermal conductivity and lead to an anisotropic thermoelectric property in boron carbide.

1.3.6 Summary

So far, bulk boron carbides are usually synthesized by carbothermal reduction at an extremely high temperature (1400-2400 °C).[52] The existence of intrinsic defects can only be found in a few literatures[63-76] and the formation mechanism of those defects is poorly understood. Although bulk boron carbides appear to be a good high temperature thermoelectric material based on the thermoelectric measurements, it is still hard to build the structure-property relationship without a thorough understanding about the structure being measured. For example, whether there are intrinsic defects, and the effect of the

orientations of planar defects on thermoelectric properties need to be addressed. Thus, a clear idea about the structure of boron carbide will have a better answer to the puzzle we are facing. Also, it is necessary to know whether the thermoelectric performance of boron carbide can be improved due to the nano effect.

1.4 Boron Carbide Nanowires as a Better Thermoelectric Material

Given that bulk boron carbide is a good high temperature thermoelectric material, it is reasonable to expect the further enhancement of figure of merit for boron carbide nanowires due to the quantum confinement effect as briefly discussed in section 1.2.3. However, most of the measured thermoelectric properties from bulk boron carbide are from poorly characterized polycrystalline samples, which makes them hard to interpret. That calls the need for synthesizing well-defined single crystalline boron carbide nanowires to discover the structure-transport property relationship. In addition, the nature of intrinsic defects makes it interesting to explore its anisotropic influence within nanowires.

1.4.1 Current Research Status of Synthesis of Boron Carbide Nanowires

Boron carbide nanowires have been synthesized by some groups.[77-84] Usually, the method is carbothermal reduction, which is widely used for synthesis of bulk boron carbide. In this method, boron, carbon, and boron oxide powders are mixed with specific ratio. Sometimes Fe_3O_4 powders can be involved to make iron the catalytic material. Boron carbide nanowires can be obtained after the mixture is heated up to very high temperatures (1100-1800 °C) for a few hours. Most synthesized nanowires were identified as rhombohedral B_4C, but it was also reported that a metastable orthorhombic

B_8C nanowires could be synthesized by vapor sources.[83] Interestingly, Li and coworkers used cotton T-shirt as the carbon source to grow B_4C nanowires.[84]

The growth mechanism of boron carbide nanowires from those methods is considered as vapor-liquid-solid (VLS) because of the catalytic material at the tip.[78-80,85-88] However, defect cannot be observed in most of the work. Information about defect and growth direction is summarized in Table 1.1. There are several claimed growth directions, and twins could not be observed most of the time.

Table 1.1 Summary of the growth directions and existence of defect in the as-synthesized boron carbide nanowires (subscript *h* and *r* represent the hexagonal and rhombohedral indexes).

	Growth direction	Defect or not/Twin plane?
1[85]	$\perp (001)_r$	Yes/$(001)_r$
2[77]	$[021]_h$ or $[104]_h$	No
3[80]	$[003]_h$	No, but streaks in DP
4[87]	$[101]_h$	No
5[86]	$[101]_h$	No
6[84]	Along $[001]_h$	No
7[81]	$[001]_r$	Yes/$(001)_r$

1.4.2 Measured Properties of Boron Carbide Nanowires

The as-synthesized B4C nanowires were subjected to several tests to discover their physical properties.

The room temperature photoluminescence spectrum showed the peak position at 638 nm, which is a blue-shift from the peak from bulk boron carbide (~795 nm).[80] It was also indicated that boron carbide nanowires had a high field emission current (1.5 μA at a voltage of 80 V) with an enhancement factor of ~10^6.[87] The mechanical properties of

boron carbide nanowires have been tested by bending. Unlike the bulk material, B4C nanowires were proved to be very flexible with the ability to have a deformation ratio of 89% without fracture.[86]

1.5 Summary

Improving thermoelectric performance by using nanomaterials has been proven to be a promising method. With bulk boron carbide being a good high temperature thermoelectric material, it is of great interest to see if the *ZT* value can be improved by boron carbide nanowires due to nano effect. The synthesis of boron carbide nanowires have been reported by a few groups. However, the intrinsic defects and the thermoelectric properties are rarely talked about.

In this dissertation, there are three main issues to be addressed. The first one is the synthesis of boron carbide nanowires with a lower temperature in a low pressure chemical vapor deposition system. The second is the discussion of the growth mechanism of as-synthesized nanowires with different fault orientations. The third is the observation and model construction of “invisible” planar defects based on transmission electron microscopy. Last but not least, the measured thermal conductivity of the as-synthesized nanowires will be briefly reported. This preliminary data shines insights to build the structure-transport property relationship and understand the effect of intrinsic defects in boron carbide nanowires.

CHAPTER 2: EXPERIMENTAL TOOLS

In this chapter, the main synthesis tools and characterization tools used for this dissertation work are discussed, including the working principles, features of the tools, and the operation parameters.

2.1 Magnetron Sputtering

Magnetron sputtering was used to coat thin films of catalytic materials on as-cleaned substrates before the synthesis of nanowires. Like thermal evaporation or electron beam evaporation, magnetron sputtering is a physical vapor deposition technique. But different from evaporation, the magnetron sputtering does not require a high temperature to melt the target material, so there is no problem with magnetron sputtering when the target material has a high melting point.

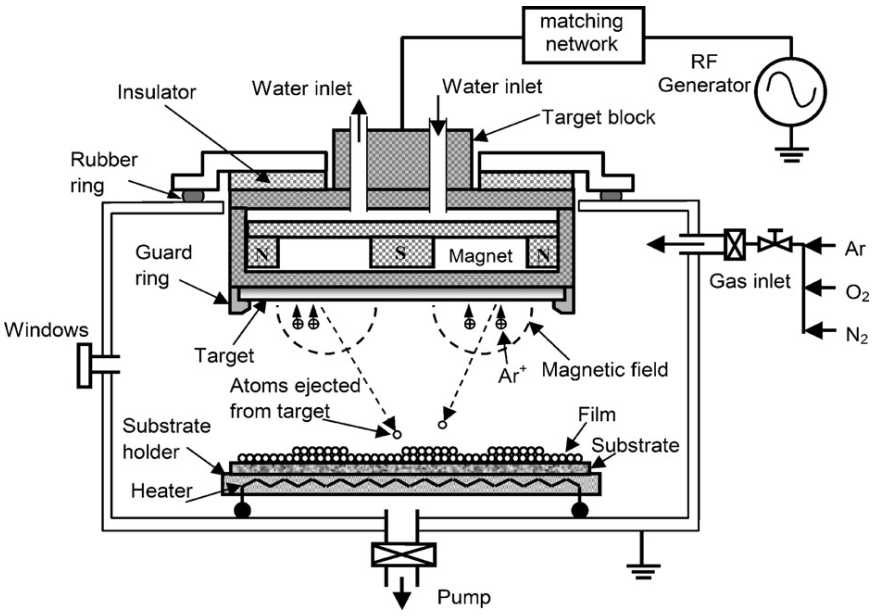

Figure 2.1 Schematic drawing of the magnetron sputtering chamber.[89]

As schematically shown in Figure 2.1, a high potential is created between the target (cathode) and the substrate to ionize the argon gas. The ionization leads to the glow of the plasma (glow discharge), which can be seen from a window to tell if it is working properly. The plasma ions are then accelerated by the high potential to strike the target, knocking out the target atoms that are deposited on the substrate. A high vacuum will help to prevent collisions between the target atoms on the way to the substrate. During interaction between the plasma and the target plane, secondary electron will also be emitted. A magnetic field is applied close to the target in a way that those secondary electrons can be confined to the vicinity of the target. The electrons, in turn, increase the ionization efficiency of the argon atoms and the deposition efficiency. The high potential can be maintained by direct current (DC) or radio frequency (RF) mode depending on the target material. The DC mode works well with the conductive target. However, if the target material is an insulator, charges will build up from the ion bombardment. It prevents the ion acceleration or even stops the bombardment. The RF mode with a high frequency (~ 13.56 MHz) can be used to solve this problem.[90] At such a high frequency, heavy ions will not follow the switching power anymore. They are guided to the target by the sheath voltage. However, electrons will follow the RF frequency to neutralize the built-up positive charges.

In this dissertation work, a Denton Vacuum Desk IV magnetron sputtering machine was used. Ni and Fe are common catalytic materials to be coated. The coating thickness is calibrated by a quartz crystal microbalance (QCM). The common thickness coated is 2 nm with a coating rate of ~0.1 nm per second.

2.2 Low Pressure Chemical Vapor Deposition System (LPCVD)

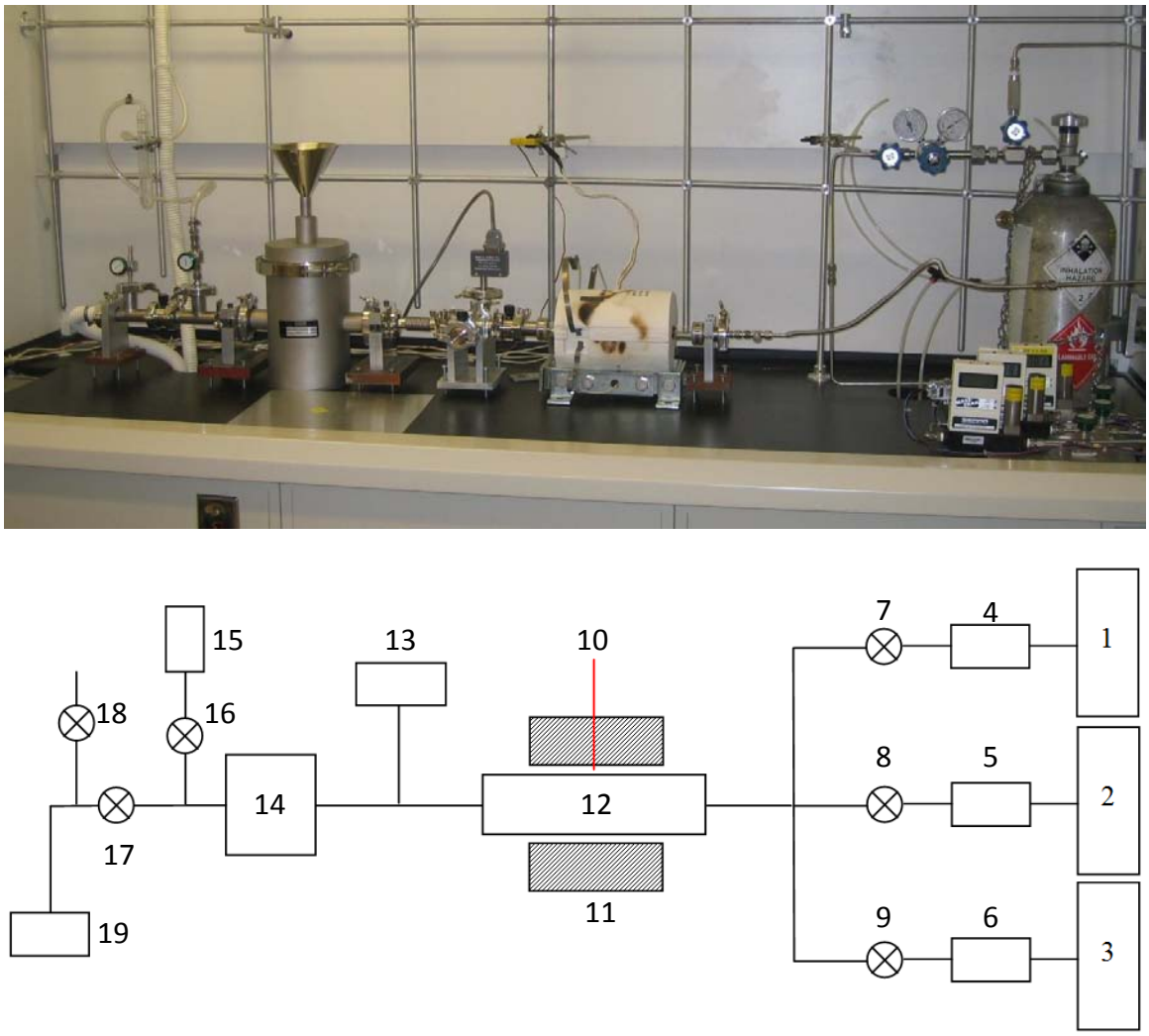

Figure 2.2 Picture and schematic drawing of the LPCVD system. 1-3: Gas cylinders for B_2H_6, CH_4, and Ar; 4-5: Mass flow controllers; 7-9: Valves; 10: Thermocouple; 11: Heating elements; 12: Furnace tube; 13: Pressure gauge; 14: Vacuum trap; 15: Bubbler; 16-18: Valves; 19: Vacuum pump.

Boron carbide nanowires were synthesized by co-pyrolysis of diborane (B_2H_6) and methane (CH_4) inside a home-built LPCVD system, as shown in Figure 2.2. The

vapor sources are introduced into the system from the right side, carried by argon (Ar). Flow rates of B_2H_6, CH_4, and Ar are controlled by mass flow controllers individually. Reaction takes place in the quartz (or alumina) tube when it is heated by the two pieces of heaters around it. The heating zone of the heaters is 20 cm. The temperature at the center of the heater is measured and controlled by a thermocouple, whose sensor is placed between the heater and the tube. The temperature controller connection is given in Figure 2.3. A target temperature can be set in the temperature controller, which also receives information about current temperature through thermocouple. It is actually a proportional-integral-derivative controller (PID controller) that controls the power switch, solid state relay.

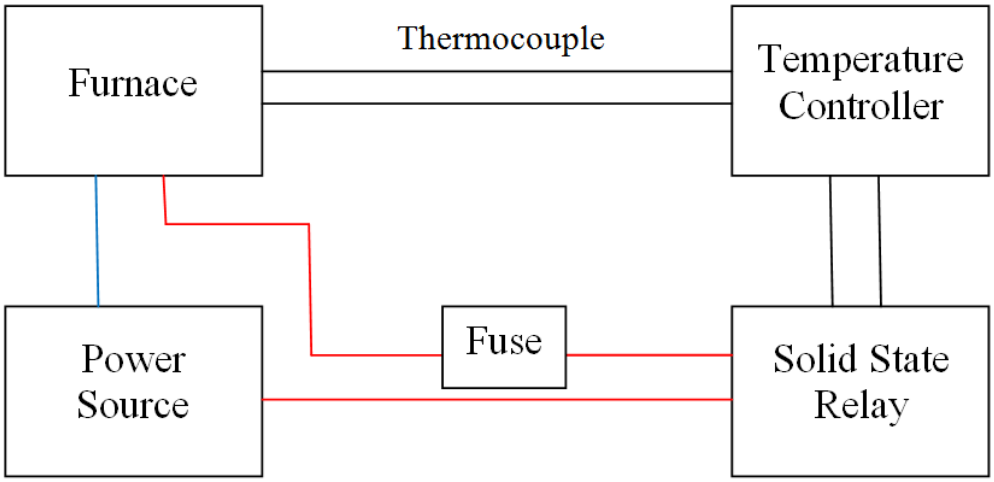

Figure 2.3 Schematic diagram of temperature controller connection.

A pressure gauge placed downstream reads the pressure of the reaction chamber. A vacuum trap is connected behind the reaction chamber in order to have a better vacuum

by condensing additional vapors inside the system. It also prevents the oil vapor entering the chamber from the mechanical pump. A bubbler is used to release the pressure when venting the chamber. At the end of the line there is a mechanical pump to provide vacuum for the whole system.

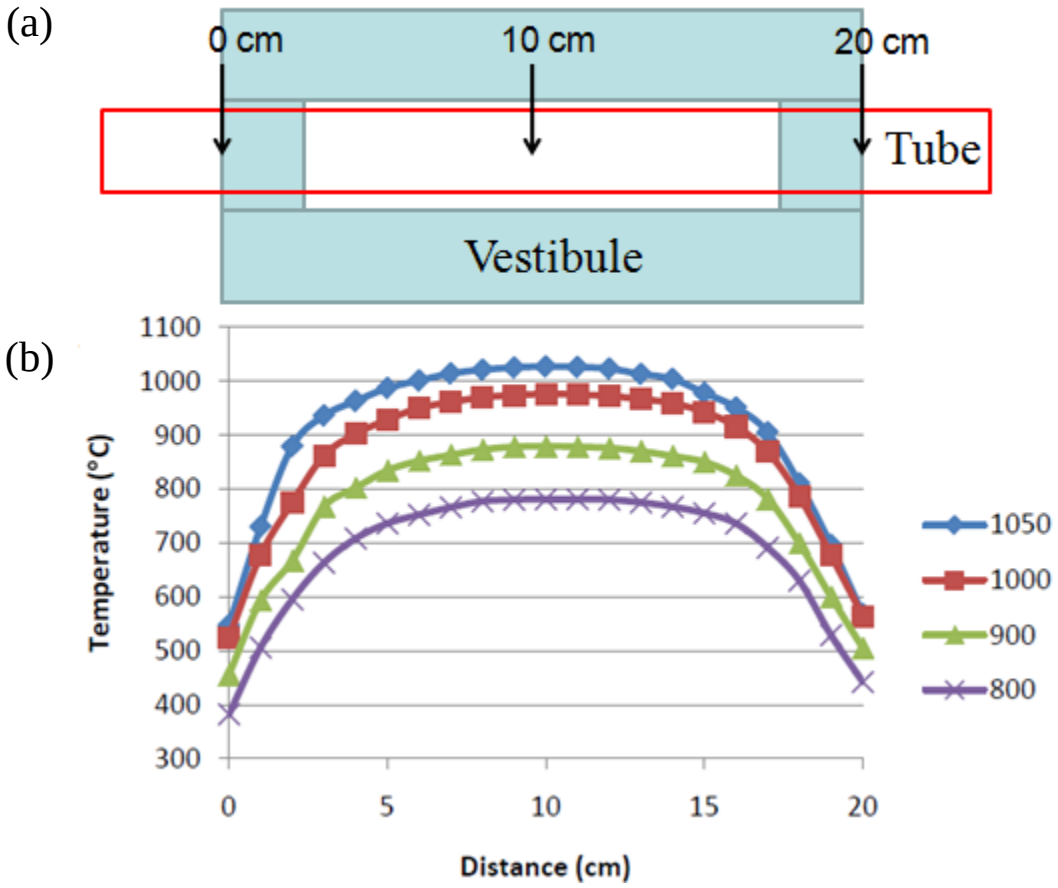

Figure 2.4 (a) Schematic drawing about the furnace, showing the positions in the heating zone. (b) Temperature profiles measured by thermocouple at different setting temperature.

The heating temperature is the highest at the center of the furnace and goes down as the position moves away to the ends. Moreover, the temperature measured by the

temperature controller is actually the temperature between the tube and the heating elements (outside the tube). In order to have a clear idea of the true temperature during reaction, a thermocouple was used to measure the temperatures inside the tube while maintaining the setting temperature at desired testing values. The maximum heating temperature of this LPCVD system is 1050 °C and the testing temperatures are 800, 900, 1000, and 1050 °C. As shown in Figure 2.4 (b), the highest temperatures appear at the distance of 10 cm (center of the tube) and the true values are slightly lower than the setting temperatures.

After the camber is vented to the atmospheric pressure, three substrates with lengths of 25 mm were put into the furnace tube at locations where the left edges of the substrates were aligned as 13.5, 16, and 18.5 cm from the left end of the heating zone (Figure 2.4). When the chamber is pumped down to ~9 mTorr, heating is started while introducing Ar gas (15 sccm). Temperature is heated up to 1050 °C in 50 minutes. Wait another 5 minutes to stabilize the temperature. Reaction gases (B_2H_6 and CH_4) are then sent to the chamber with flow rate 15 sccm for each of them. After 45 minutes, power is turned off and reaction gases are stopped. The furnace is cooled down naturally while maintaining the 15 sccm Ar flow.

2.3 X-Ray Diffraction (XRD)

As a nondestructive characterization method, XRD is widely used to identify crystal structure. X-ray is produced by the X-ray tube (Figure 2.5). Electrons are generated in the cathode by thermionic emission, while a high voltage is maintained between the cathode and the anode target to accelerate the electrons. When electrons with

high energy hit the metal target, most of the energy is converted to heat with only 1% converted as X-ray radiation.

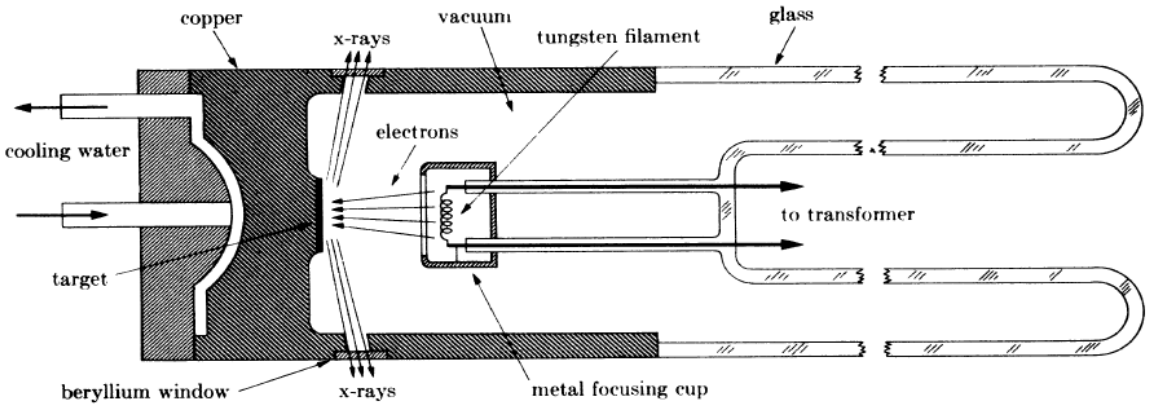

Figure 2.5 X-ray tube structure.[91]

There are two types of X-rays: continuous X-ray and characteristic X-ray (Figure 2.6). The incoming electrons may encounter single or multiple collisions, which emit energies due to the deceleration of electrons. If the electron gives up all its kinetic energy by one collision, all the kinetic energy (eV) will be converted to the generated X-ray with the highest energy. This type of X-ray has the shortest wavelength λ_{SWL}, which is shown in the X-ray spectrum as the short wavelength limit.

$$\lambda_{SWL} = \frac{hc}{eV} \tag{2.1}$$

in which, *h* is the Plank constant, *c* is the speed of light, *e* is the charge of an electron, and *V* is the voltage applied. But if the electron undergoes several collisions, only part of its kinetic energy will be converted each time. Therefore, the emitted X-ray will have a lower energy or a higher wavelength, which leads to the continuous X-ray spectrum with

higher wavelengths than λ_{SWL}. It is known from equation 2.1 that the value of λ_{SWL} will be reduced when a higher voltage is applied. That explains the left-shifting nature of the continuous X-ray spectrum when the voltage keeps rising. Sometimes the continuous X-rays are called “bremsstrahlung”, which means “braking radiation” in German.

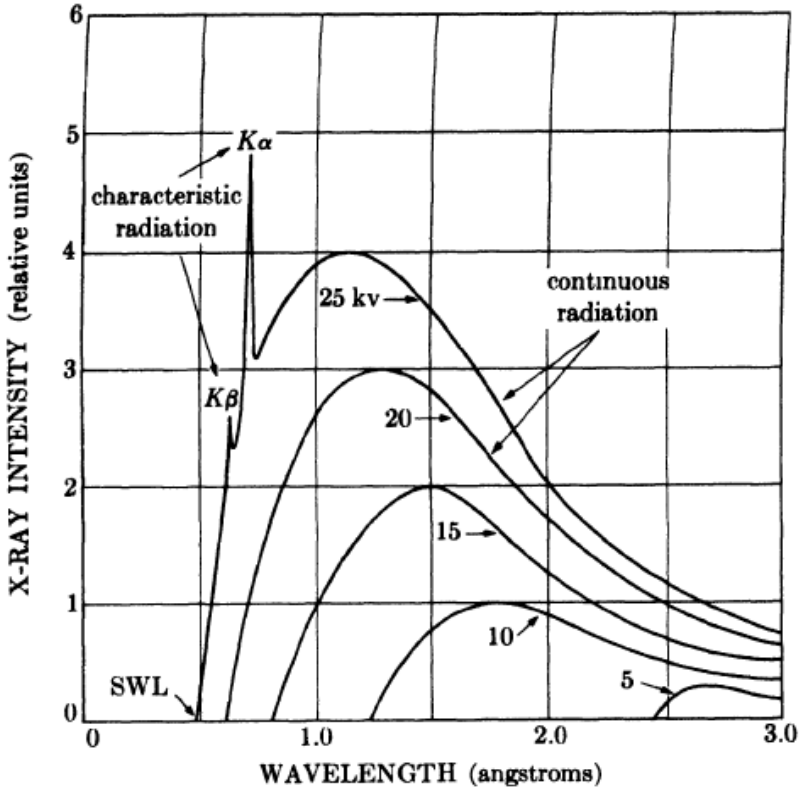

Figure 2.6 Continuous X-ray and characteristic X-ray.[91]

If the applied voltage is high enough, the incoming electrons will have sufficient energy to knock off the inner shell electrons from the target metals, leaving a hole in the inner shell. As a result, electrons from outer shell will fill the vacancy and the energy difference between those electron levels will be emitted in the form of X-ray radiation.

Figure 2.7 shows the emission of K_α characteristic X-ray. Since each atom has its unique electron levels, the emitted X-rays are called characteristic X-rays. Depending on energy differences between electron levels, the emitted X-rays are called K_α, K_β, L_α, L_β, etc. The strong and sharp K_α line makes it possible to capture it for X-ray diffraction.

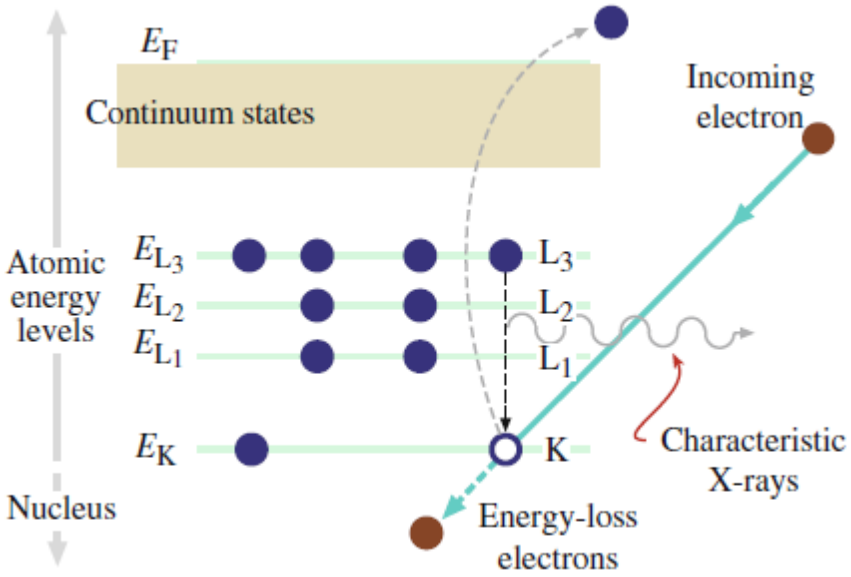

Figure 2.7 The principle of generating K_α characteristic X-rays.[92]

A nickel filter is placed in the path of X-ray to block the K_β emission, making it monochromatic. When the incident beam hits the crystalline material, diffraction happens and the intensity of the diffracted beam can be enhanced from some specific diffraction angles according to Bragg's law.

$$2dsin\theta = n\lambda \qquad (2.1)$$

λ is the wavelength of the incident X-ray, which is about 0.154 nm for copper K_α beam, d is the spacing between certain atomic planes, θ is the angle between incident beam and the scattering plane, and n is an integer. Thus by measuring the diffraction angle θ, the spacing of each corresponding atomic plane can be calculated.

In this work, the as-synthesized boron carbide nanostructures were analyzed by X'Pert Pro from PANalytical. The SiO_2/Si substrates carrying as-synthesized boron carbide nanowires were put on the stage by double sided tape. Voltage and current were set as 45 kV and 40 mA, respectively. To align the substrates with the X-ray beam, 2θ scan and Z scan were performed using the optics listed in "alignment mode" from Table 2.1. Optics were changed based on "scanning mode" after alignment. The 2θ-θ scan was carried out with a range of 10-140°, a step size of 0.05°, and a scan rate of one second per step.

Table 2.1 Settings of optical components for alignment and scanning.

	Optics	Alignment mode	Scanning mode
Incident beam	Divergence slit	Slit Fixed 1/32	Slit Fixed 1/2
	Beam attenuator	Cu/Ni 0.2/0.02 mm manual	Automatic
	Filter	None	Ni 0.02 mm
Diffracted beam	Receiving slit	Parallel Plate Collimator Slit	Parallel Plate Collimator Slit
	Collimator	Parallel Plate Collimator 0.27	Parallel Plate Collimator 0.27
	Soller slit	Soller Slit 0.04 rad	Soller Slit 0.04 rad

2.4 Scanning Electron Microscope (SEM)

SEM is a convenient and powerful method to provide structure and composition analysis for the tiny structures down to the nanoscale. It utilizes electron beam as a probe to examine the specimen. The electron source is produced by applying a high voltage on the filament made of tungsten or LaB_6. Generally, the accelerating voltage is less than 50 kV. The beam path is controlled by the electromagnetic coils along the column, so that it can be focused on the position of interest. When the incident electron beam hits the specimen, several interactions occur, generating other radiations that contain useful information about the specimen (Figure 2.8 (a)).The incident electron can be scattered elastically or inelastically. In the case of an elastic scattering, the electron is deflected by Coulomb interaction and there is no energy change (backscattering electrons). On the other hand, part of the incident electron's energy can be transferred to the specimen, which leads to the generation of secondary electron, Auger electron, or X-ray radiation.

Each type of generated radiation comes from different depths under the specimen's surface. In Figure 2.8 (b), the volume under sample's surface is called interaction volume, which indicates the position where certain radiation is generated. The beam is controlled to scan the viewing area, and by capturing the generated secondary electrons or backscattered electrons, topography or composition images can be formed. As the interaction volume of secondary electrons is close to the surface, SEM is sensitive to the specimen's morphology.

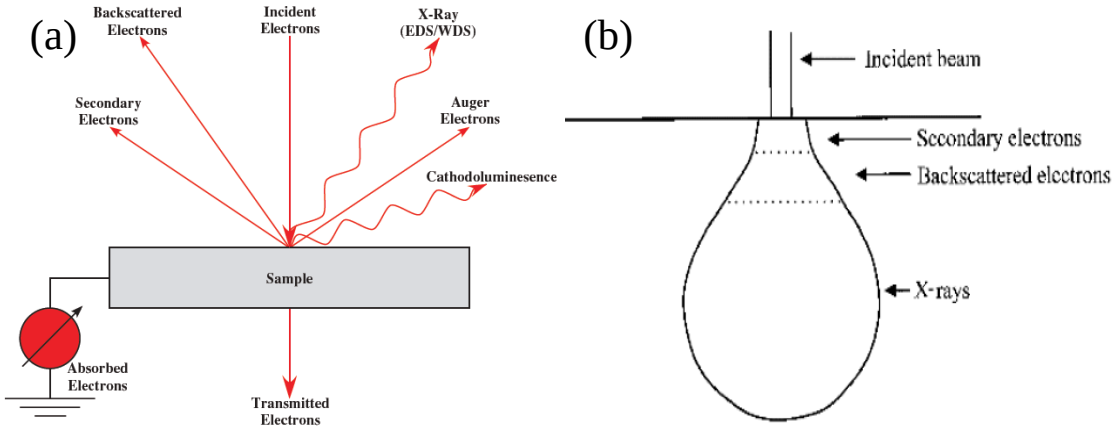

Figure 2.8 Electron-matter interactions[93] and the interaction volume[94].

In this work, the SEM used to characterize boron carbide nanowires is JSM-6480 from JEOL with a tungsten thermionic electron gun. This SEM system is equipped with an energy dispersive X-ray spectroscopy (EDS) detector to perform compositional analysis. Generally, an accelerating voltage of 10 kV and a working distance of 10 mm are selected to take images. A higher accelerating voltage (20 kV) is needed for the EDS spectrum to generate the characteristic X-rays.

2.5 Transmission Electron Microscope (TEM)

Another powerful characterization tool used is TEM. Like in the SEM, a TEM also uses electrons to form images. However, it is using the transmitted electrons instead of the scattered ones. In other words, all the pixels are formed at the same time. The resolution of a microscope can be written as

$$d = \frac{0.61\lambda}{\mu sin\beta} \tag{2.2}$$

λ is the wavelength of incident electrons, μ is the refractive index of the viewing medium, and β is half of the collection angle. Sometimes the term $\mu sin\beta$ is called numerical

aperture. Since a higher accelerating voltage gives more energy to the incident electrons, the wavelength becomes smaller and the resolution is smaller. TEM is using a much higher accelerating voltage (several hundred kV), so its resolution is much better than SEM images.

Again, the electron is generated by tungsten or LaB_6 filament and controlled by condenser lenses, intermediate lenses, and objective lenses. Electrons from all the directions are transmitted at the same time. The ones with parallel beam path will end up with diffraction spots on the back focal plane that close to objective aperture (label in 2.9). Thus a diffraction pattern (DP) can be obtained by using the image at back focal plane. Beneath the back focal plane, there is the image plane near the select area diffraction aperture. Electrons transmitted from the same position converge at this level, which can be used to form TEM images.

There are some issues need to be considered when using TEM. First, the specimen needs to be thin enough, so the electron beam can be transmitted. This is not a problem for us because the diameters of the boron carbide nanowires are within 100 nm. Second, the TEM image is a projection view. It could be misleading when talking about crystal directions based on the TEM images. Third, some specimen can be damaged by the high energy electron beam.

A JEM-2100 TEM from JEOL with a LaB_6 filament (thermionic electron gun) was used to characterize boron carbide nanowires. The accelerating voltage was set as 200 kV. A JEOL double tilt specimen holder was used for nanowires on the TEM copper grids. But for the nanowires that have gone through thermal measurements, a Gatan “646 double tilt analytical holder” was used because the micro device cannot be put into JEOL

holder. TEM images and diffraction patterns were captured by a CCD camera (SC1000 ORIUS TEM CCD camera from Gatan) and the DigitalMicrograph software. Data were further processed by CorelDRAW software for post-analysis (measurement of diameter and fault density).

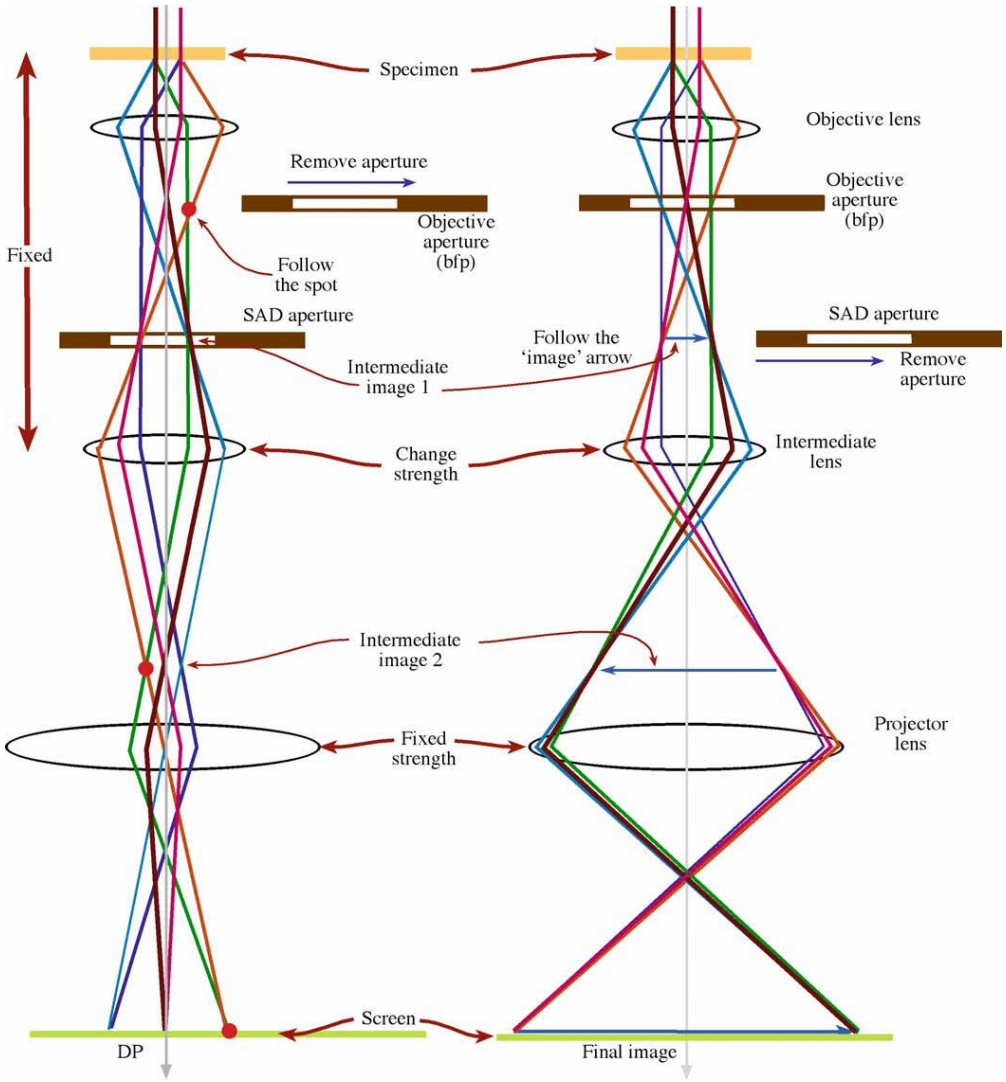

Figure 2.9 The beam paths of two basic TEM mode.[92]

2.6 Energy Dispersive X-ray Spectroscopy (EDS)

The EDS detector is usually equipped with SEM or TEM to analyze the composition of the tested specimen. As mentioned previously, characteristic X-rays can be generated when the electrons hit the specimen. Since those X-rays carry information about the energy levels from the electron shells within the atoms, they can be used to analyze the composition of the specimen. Usually an EDS system is composed of an X-ray detector to convert the collected X-rays to electronic signals and a signal analyzer to display the data into a histogram in terms of X-ray energies, which are determined by the electronic signals from the detector.

An X-ray detector is usually made of a lithium-drifted silicon crystal, which is able to absorb incoming X-rays and create electrons and holes. The detector is cooled by a liquid nitrogen reservoir while absorbing X-rays. The amount of generated electron-hole pairs within the crystal is proportional to the energy of the absorbed X-rays. When a bias voltage is applied on the gold layers located at both ends of the silicon detector, the generated carriers lead to a current flow (pulse) within the detector. The pulse signal is converted to the voltage signal, which is then analyzed by a multichannel analyzer with each channel representing a certain X-ray energy level. A histogram can be drawn based on the stacking X-ray signals in terms of energy. By looking at this histogram, users will be able to tell the composition.

From section 2.3, we know that the emitted X-rays include not only characteristic X-rays, but also continuous X-rays. Noises and the continuous X-rays contribute to the background signals of an X-ray spectrum. Increasing the process time can help to

enhance the signal/noise ratio. However, the trade-off of doing that is that it takes a longer time to collect the signals.

To prevent contamination to the detector, a window (typically beryllium) is placed in front of the detector. But the beryllium window will absorb the X-rays with long wavelength, although the window is very thin. That makes it hard to detect the light elements (boron, carbon, etc.) accurately. To solve this problem, some modern X-ray detectors are equipped with ultra thin polymer windows or even windowless.

The Oxford Instruments EDS Systems (for SEM or TEM) were used in this work. They are capable to detect boron signals since a Be window is used. For the EDS equipped with SEM, a higher acceleration voltage (20 kV), a larger spot size (40-50), and a larger aperture (size 3) are used to excite the X-rays from samples. There are three working modes: spot, line, and mapping. In the case of spot mode, electron beam is focused on a selected spot, where characteristic X-rays are generated for analysis. An EDS spectrum containing all the detected elements is generated in the spot mode. In the line scan mode, the electron beam is moved along the path of a selected line. In addition to the EDS spectrum, the quantity of each element along the line is displayed by a curve, so that the trends at interface or concentration gradients can be easily seen. If further composition information about whole area is needed, the mapping mode can be used. The electron beam scans the selected area and composition information is given pixel by pixel, which generates a composition map for each existing element. Mapping is very helpful because it allows the user to compare element maps with the SEM image, so it is clear to see the element distribution. But the drawback of the mapping mode is that it talks a long time to finish the scan.

Since samples used for TEM are tiny, so taking the EDS spectrum needs more time (~100 seconds). Sometimes the holder also needs to be tilted to the +X direction (about +20°) to adjust the sample surface to the X-ray detector, so that it can have a better collection.

2.7 Electron Energy Loss Spectroscopy (EELS)

Although the advanced EDS system is able to analyze light elements, it is hard to achieve the quantity analysis accurately due to two reasons. First, the long-wavelength X-ray radiations emitted by light elements can be easily absorbed by not only the window of the detector, but also the specimen itself. Second, light elements are more likely to emitted Auger electrons rather than characteristic X-rays from the excited state. As mentioned in section 2.3, electron beam with sufficient energy can bring the atom to the excited state by knocking out the inner shell electron. The vacancy is then filled by the electron from outer shell with a higher energy. This energy difference can be emitted as characteristic X-rays. However, the energy difference can also be used to eject another electron, which is called Auger electron. Auger electron and characteristic X-ray are competing with each during the relaxation process. The ratio of characteristic X-ray decreases for elements with smaller atomic number, which makes it even more difficult to detect light elements by EDS.

EELS captures the transmitted inelastically scattered electrons for analysis, so there is no need to worry about the emitted characteristic X-rays. The spectrometer is a magnetic prism located below the TEM column (Figure 2.10 (a)). An entrance aperture limits the collection angle of the transmitted electrons beam, which is deflected by a magnetic prism to the detector. The magnetic prism is designed in such a way that the on-

axis beam and off-axis beam can be focused on a point in the dispersion plane. The inelastically scattered electrons (dotted curves in Figure 2.10 (b)) have lost some energy and are further deflected by the magnetic field than the zero loss beams. The amount of the deflection depends on the energy loss of the electrons. Thus, a spectrum can be obtained on the dispersion plane with intensity and energy loss being the y-axis and x-axis, respectively.

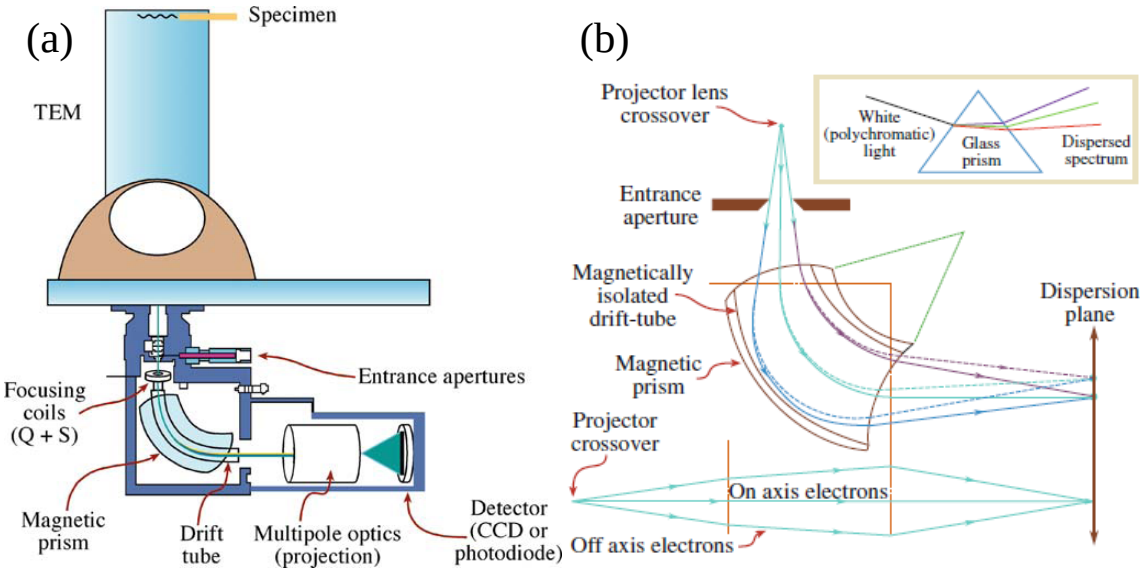

Figure 2.10 Schematic drawing of EELS spectrometer and the electron beam diagram. The solid curves in (b) indicate the beam paths of the zero-loss beam, while the dotted curves are the paths for inelastically scattered electrons[93]

As shown in Figure 2.11, an EELS spectrum consists of two parts: low energy loss region and high energy loss region. There are generally four types of inelastic scattering that contribute to the EELS spectrum: phonon excitations, electron transitions, plasmon excitations, and inner-shell ionizations. The first three interactions and the zero

loss peak fall into the low energy loss region, while the inner-shell ionizations are the main features in the high energy loss region. The boundary of the two regions is ~50 eV. In the low energy loss region, the zero loss peak results from those electron with no energy loss. Phonon excitations are very close to the zero loss peak, which makes it hard to detect. The electron transitions happen within or between electron shells with low energy loss. The plasmon peak comes from the longitudinal oscillations of the weakly bound electrons. In the high energy loss region (>50 eV), the sharp edges superimposed on the background signals are related to the inner shell ionization of the existing atoms. Those ionization edges are used to analyze the composition of the specimen. As the energy loss increases, the intensity of the spectrum decreases.

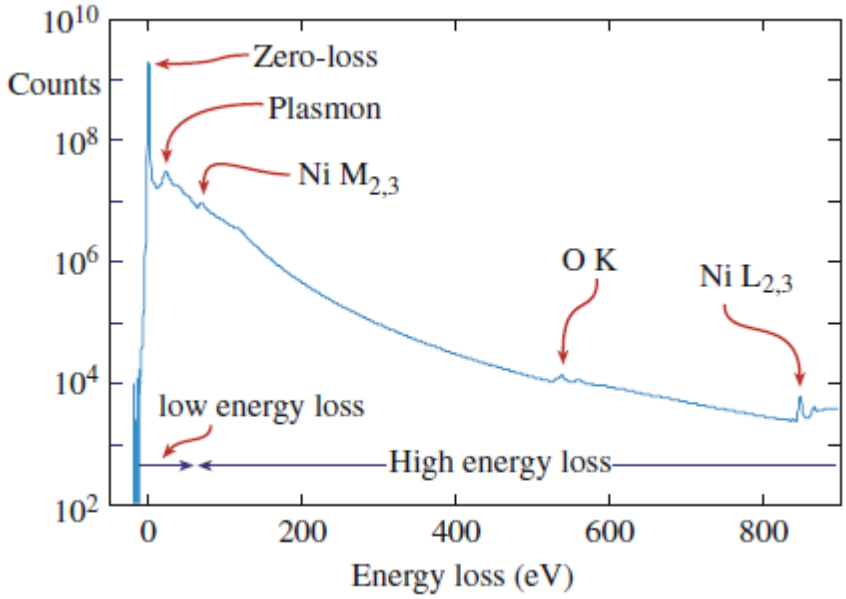

Figure 2.1An EELS spectrum showing the low energy loss region and high energy loss region.[92]

EELS spectra were collected at the Electron Microscopy Center in University of South Carolina by a JEOL JEM-2100F scanning transmission electron microscope equipped with a Tridiem Gatan Imaging Filter (Model 863). The electron energy loss spectrometer is second-order corrected, third-order optimized to allow for a large entrance aperture without significant loss of energy resolution. Point resolution of the microscope is 0.19 nm while the energy resolution is 1 eV.

CHAPTER 3: SYNTHESIS OF BORON CARBIDE NANOWIRES

In this chapter, the synthesis of boron carbide nanowires by co-pyrolysis of diborane (B_2H_6) and methane (CH_4) in a low pressure chemical vapor deposition (LPCVD) system at temperatures below 1000 °C is reported. The CVD-based method is energy efficient and cost effective. The lowest synthesis temperature was found to be 879 °C, which is significantly lower than those reported for carbothermal reduction. The reaction time (*e.g.*, 45 minutes to produce ~5 μm long nanowires) is also shorter than that for carbothermal reduction. The as-synthesized nanowires were characterized to have single crystalline boron carbide cores and thin amorphous oxide sheaths. Planar faults of different morphologies, including both transverse faults and axial faults, were observed and thoroughly characterized. These boron carbide nanowires allow for studies of the effects of crystalline defects and boundaries on transport properties at nanoscale, and could lead to further enhanced thermoelectric performance.

3.1 Synthesis

Boron carbide one-dimensional (1D) nanostructures were synthesized by co-pyrolysis of B_2H_6 and CH_4 at elevated temperatures in a LPCVD system. Typical synthesis conditions are described here. Silicon (Si) wafers with one-micron-thick thermally grown silicon dioxide (SiO_2) purchased from University Wafer were cut into small pieces (10 mm × 25 mm). These SiO_2/Si substrates first went through a three-step cleaning process, including (i) ultrasonic cleaning by certified ACS grade acetone and

methanol (Branson Ultrasonic Cleaner; 70W, 3 minutes), (ii) blow drying by compressed nitrogen, and (iii) oxygen plasma cleaning (Kurt J Lesker: Plasma-Preen 862; oxygen flow rate: 1.94 standard cubic feet per hour, 425 W, 3 minutes). The cleaned substrates were then coated with a 2 nm-thick nickel (Ni) thin film using magnetron sputtering (Denton Vacuum: Desk IV TSC). The coated substrates were subsequently loaded into a quartz boat, and placed in a desired position in the quartz tube of the LPCVD system. The whole system was first evacuated to a pressure of ~7 mTorr, after which the quartz tube was ramped up to 1050 °C (center position temperature measured outside the quartz tube by a thermocouple) in 50 minutes. A constant flow of 15 sccm (standard cubic centimeters per minute) Ar (Linde: 99.999% UHP) was maintained during the whole experiment. To synthesize boron carbide 1D nanostructures, 15 sccm B_2H_6 (Voltaix; 5% Ultra High Purity B_2H_6 in research grade Ar) and 15 sccm CH_4 (Linde Gas; compressed methane) were introduced to the quartz tube for 45 minutes at 1050 °C. The typical reaction pressure was ~440 mTorr.

After reaction, the quartz tube was cooled down to room temperature naturally in ~5 hours. The substrates were then taken out and characterized by Scanning Electron Microscopy (SEM; JEOL JSM-6480), and Transmission Electron Microscopy (TEM; JEOL JEM-2100 LaB_6 microscope) including electron diffraction, high resolution TEM (HRTEM) and Energy Dispersive X-ray Spectroscopy (EDS; Oxford Instruments: with a super atmospheric thin window X-ray detector which is capable of detecting boron).

3.2 Characterization of the As-Synthesized Nanowires

A schematic drawing of the furnace and the products on different locations are given in Figure 3.1. Since the heating temperature is measured and controlled by a

thermocouple at the center of the tube furnace, the reaction temperature inside the tube is the highest at the center and drops to the lowest at the ends of the tube, as shown by the solid curve. Source gases (B_2H_6 and CH_4) and carrier gas (Ar) are introduced from the right inlet. Most of the B_2H_6 gets decomposed when entering the heated tube, resulting in the higher concentration of boron-containing species at the inlet (dotted curve). The concentration profile of carbon-containing species produced by decomposition of CH_4 is shown by the dashed curve.

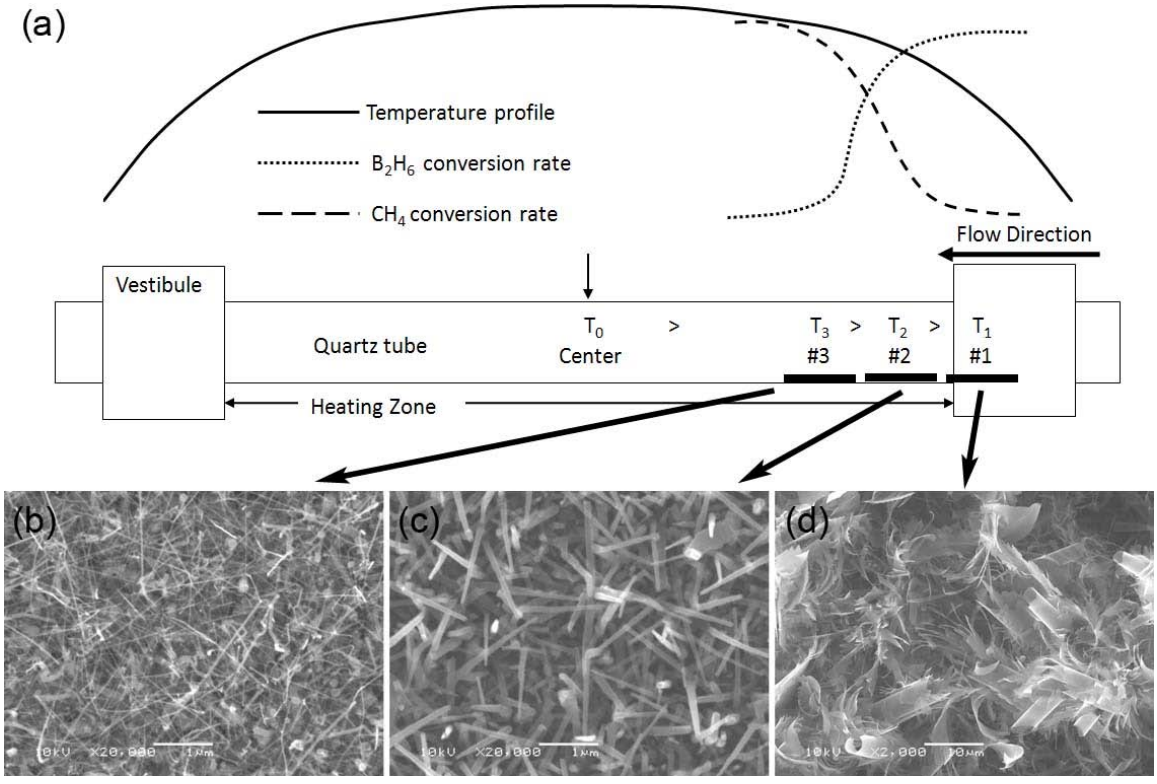

Figure 3.1 (a) A schematic drawing of the furnace tube, temperature profile and concentration profile of reaction species. Products on different substrates are (b) boron carbide nanowires on #3 (c) boron carbide nanorods on #2, and (d)α-tetragonal boron nanoribbons and nanoplatelets on #1.

Substrates are put close to the right inlet in different temperature regions. Due to the unique combination of temperature and the decomposition rate of B_2H_6 and CH_4, three different types of crystalline nanostructures could be synthesized. They are (1) boron carbide nanowires with high aspect ratio in the temperature range of 964–977 °C (Figure 3.1 (b)), (2) tapered short boron carbide nanostructures in the temperature range of 908–931 °C (Figure 3.1 (c)), and (3) α-tetragonal boron nanoribbons and nanoplatelets in the temperature range of 630–750 °C (Figure 3.1 (d)).

In this dissertation work, the focus is on the nanowires with high aspect ratio shown in Figure 3.1 (b), and results are discussed below and in chapters afterwards.

3.2.1 Identification of As-Synthesized Nanowires

Figure 3.2 (a) is an SEM image of as-synthesized nanowires having diameters between 15 and 90 nm and lengths up to 10 μm. In order to find out detailed crystallographic information of these nanowires, more than one hundred of them were studied by TEM. Typical results are presented in Figure 3.2 (b). Inset I in Figure 3.2 (b) is a low magnification TEM image of a part of a nanowire. The catalytic material at the tip of the nanowire is clearly revealed. The HRTEM image (Figure 3.2 (b)) of the area enclosed by the black rectangle in inset I shows that the nanowire has a single crystalline core and a 0.5–2 nm thick amorphous sheath. The image also reveals the existence of planar defects such as twins and stacking faults in the nanowire. Inset II is the corresponding selected area electron diffraction pattern recorded along the [010] zone axis. The streaks in the diffraction pattern further confirm the existence of planar defects in the nanowire. On the basis of the HRTEM imaging and electron diffraction pattern analysis, the nanowire was found to have a rhombohedral boron carbide lattice. As

mentioned before, boron carbide is a solid solution with carbon composition varying between 8.8 and 20 at.%. According to the Joint Committee on Powder Diffraction Standards (JCPDS) database, there are at least seven rhombohedral boron carbides such as B_4C, $B_{10}C$ and $B_{13}C_2$. These boron carbides with different chemical formulas share identical crystal structure and similar lattice parameters of variation less than 1.5%. Based on the TEM results, it is difficult to accurately distinguish phases between various boron carbides. However, the calculated lattice constants for this particular nanowire are closer to values for $B_{13.7}C_{1.48}$ according to the JCPDS 01-071-0363. The growth direction of the nanowire was found to be perpendicular to the (001) plane. Figure 3.2 (c) reveals the EDS results of compositional information in the core, sheath and tip of the nanowire. The existence of B, C, O and Si was found in both the core and sheath. (Note: the Cu signal comes from the supporting Cu grid and is not a component of the nanowire). The higher O:B (or O:C) ratio observed from the sheath indicates that the periphery of the nanowire is rich in O. The inset shows the results from semi-quantitative analysis of atomic percentage of B and C in cores of five nanowires. A typical EELS spectrum is given in Figure 3.2 (d). The analyzed quantification shows a variation of boron composition of 84–88 at.%. EELS results are consistent with that from EDS. Variation of compositions can be seen from both EELS and EDS. That is due to the fact that boron carbide is a solid solution with carbon atomic percentage varying between 8.8–20% and cannot be described by a simple fixed chemical formula (although B_4C is being widely used as the chemical formula of boron carbide). The catalytic material is composed of B, C, O, Ni and Si. A very small amount of Si exists in both the core and the sheath. In

general, the Si might come from the SiO_2/Si substrates, quartz boats and quartz tubes used for LPCVD synthesis.

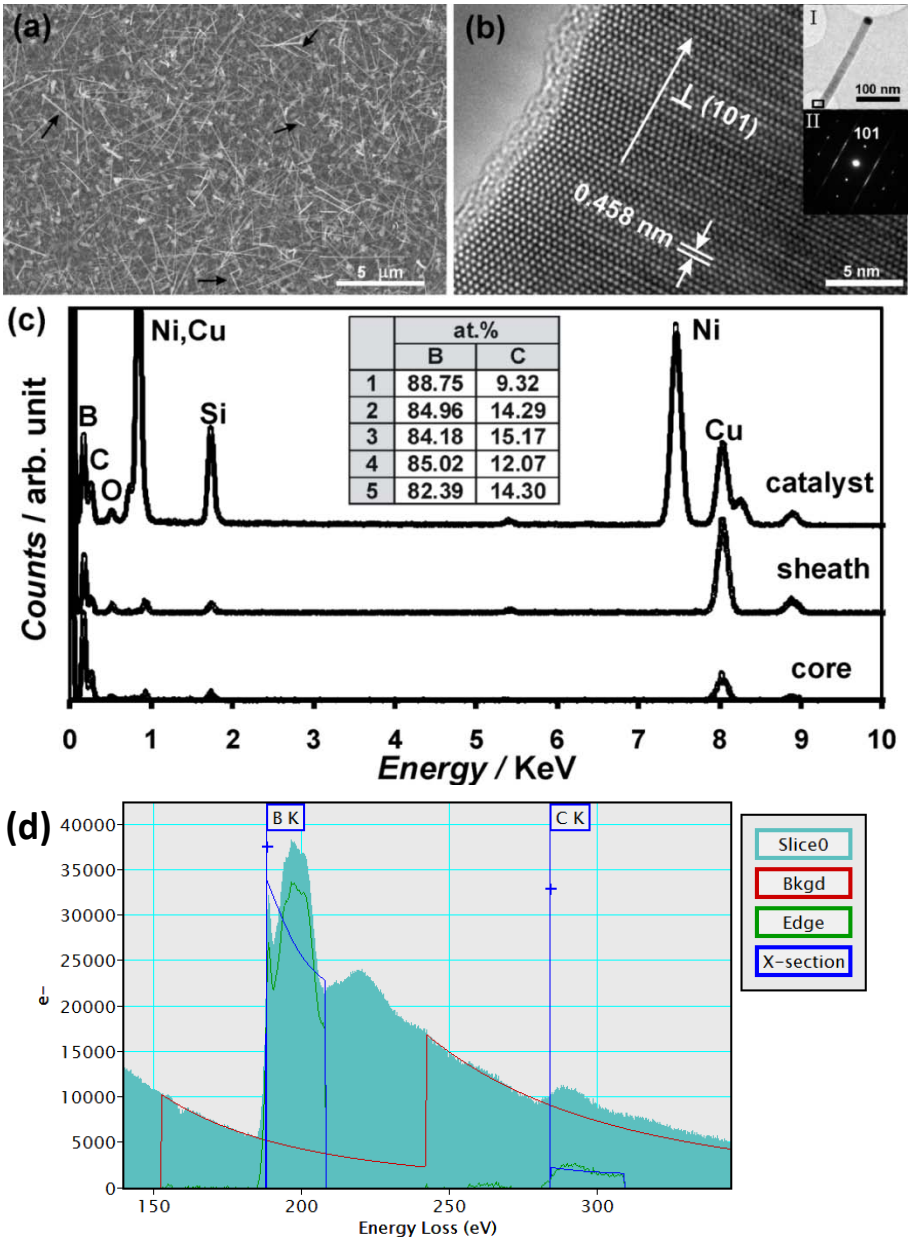

Figure 3.2 Materials characterization of as-synthesized nanowires. (a) An SEM image shows both straight and kinked nanowires (pointed by black arrows). (b) TEM results show the nanowire has a single crystalline core and a 0.5–2 nm thick amorphous oxide sheath. The growth direction of the nanowire is perpendicular to (001) plane. (c) EDS results show the compositional information within the core, sheath and catalyst of a nanowire. The inset is a summary of atomic percentage of B and C in five different nanowires. (d) EELS spectrum taken from one nanowire.

A histogram of diameters is created according to the first ninety-two characterized nanowires (Figure 3.3). The diameters were determined by the sizes of the catalyst before reaction, when most of catalysts have diameters between 30–60 nm.

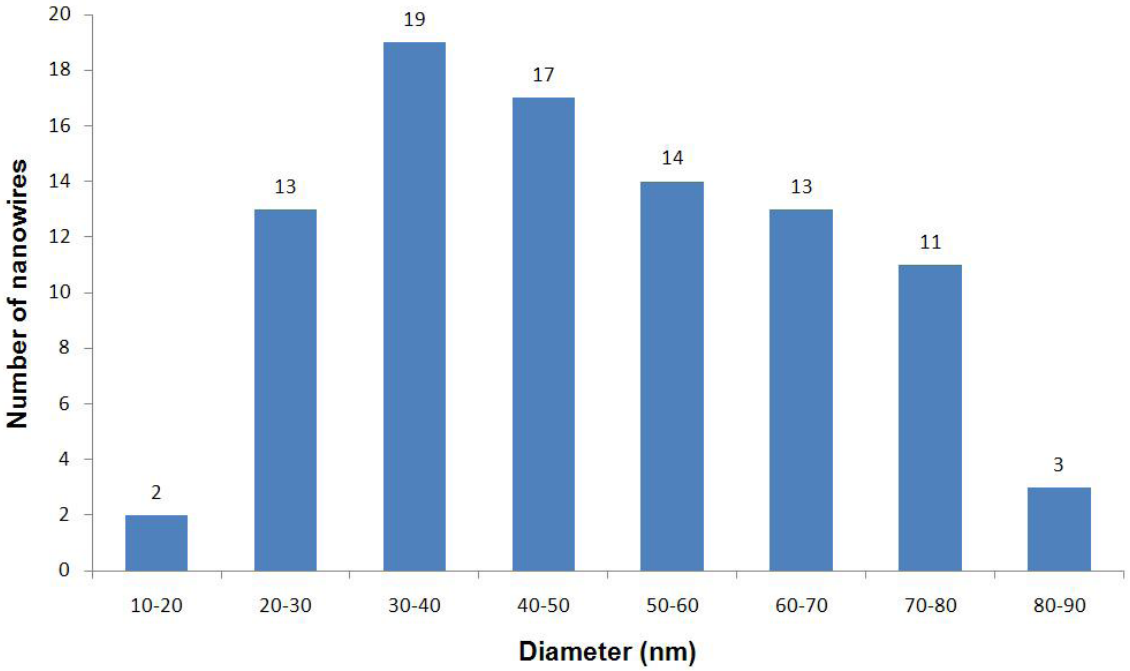

Figure 3.3 A histogram of diameters of as-synthesized boron carbide nanowires. A total of 92 nanowires were analyzed by TEM characterization. Their diameters were between 15 and 90 nm. The average diameter was ~48.5 nm, and the standard deviation was ~17.6 nm.

3.2.2 Effects of Experimental Parameters

Other than the standard experiment mentioned in the experimental section (i.e., using Ni as the catalytic material, 15 sccm B_2H_6 + 15 sccm CH_4 +15 sccm Ar gas flow, 1050 °C furnace center temperature, 45 minutes reaction time), a set of controlled synthesis experiments were carried out to explore the growth mechanism and optimize the growth conditions of boron carbide nanowires. (i) *Catalytic Materials*. Figure 3.4 (a) and (b) illustrate that growth of nanowires occurred only when catalytic materials such as

Ni were used. As revealed by TEM analysis, Ni was commonly found at tips of nanowires. This result indicates that the growth of these nanowires can be attributed to the vapor-liquid-solid (VLS) mechanism.[95] Both Ni and Fe were found to be effective catalytic materials to grow boron carbide nanowires. (ii) *Reaction Time*. With other parameters (*i.e.*, catalytic material used, reaction temperature and the gas flow rate) unchanged, the reaction time was varied from 5 to 120 minutes. No growth of nanowires was observed when the reaction time is less than 15 minutes. Between 15 and 80 minutes, a longer reaction time led to more and longer nanowires (Figure 3.4 (c) and 3.4 (d)). However, further increasing the reaction time to 120 minutes mainly resulted in coarsening of nanowires, instead of more and longer nanowires. The optimal reaction time was found to be 80–90 minutes, producing nanowires with a mean diameter of ~ 50 nm and an average length of 10 μm. (iii) *Reaction Temperature*. The center temperature of the furnace was varied from 900–1050 °C with an interval of 50 °C. Growth of nanowires was not observed until the center temperature was greater than or equal to 950 °C. When the center temperature was set as 950 °C (Figure 3.4 (e)), nanowires were found in the 879–885 °C temperature zone region. When the center temperature was set as 1050 °C (Figure 3.4 (f)), nanowires were observed in the 964–977 °C region. Independent of the prescribed furnace center temperatures, the growth region is always approximately 1.5 mm long. However, a higher center temperature could lead to production of more and longer nanowires. To the best of our knowledge, the observed growth temperature (min. 879 °C) in this study is the lowest temperature used to synthesize crystalline boron carbide nanowires by vapor-based and carbothermal reduction techniques.[96] (iv) *Ratio between B_2H_6 and CH_4*. The effect of amount of gas

precursors was studied by changing the flow ratio between B_2H_6 and CH_4. Nanowires can be synthesized when the ratio of flow rate between B_2H_6 and CH_4 is less than five. For instance, keeping the flow rate of B_2H_6 as 15 sccm, the growth of nanowires was stopped when the flow rate of CH_4 was less than 3 sccm. As shown in Figure 3.4 (g) and (h), a higher CH_4 flow (*i.e.*, lower B_2H_6/CH_4 ratio) can facilitate the growth of boron carbide nanowires. (v) *Materials of the Substrate and the Reaction Tube*. When the substrate was changed from SiO_2/Si to sapphire and the reaction tube was simultaneously changed from quartz to alumina, Al-doped boron carbide nanowires can be synthesized. As discussed previously,[97] the pyrolysis of B_2H_6 might yield highly reactive boron and hydrogen, interacting with substrate and reaction tube and producing gas phase Si-containing species (such as SiH_x radicals, x=1 to 3) or Al-containing species. These Si (or Al)-containing species could in turn serve as dopants and produce doped boron carbide nanowires.

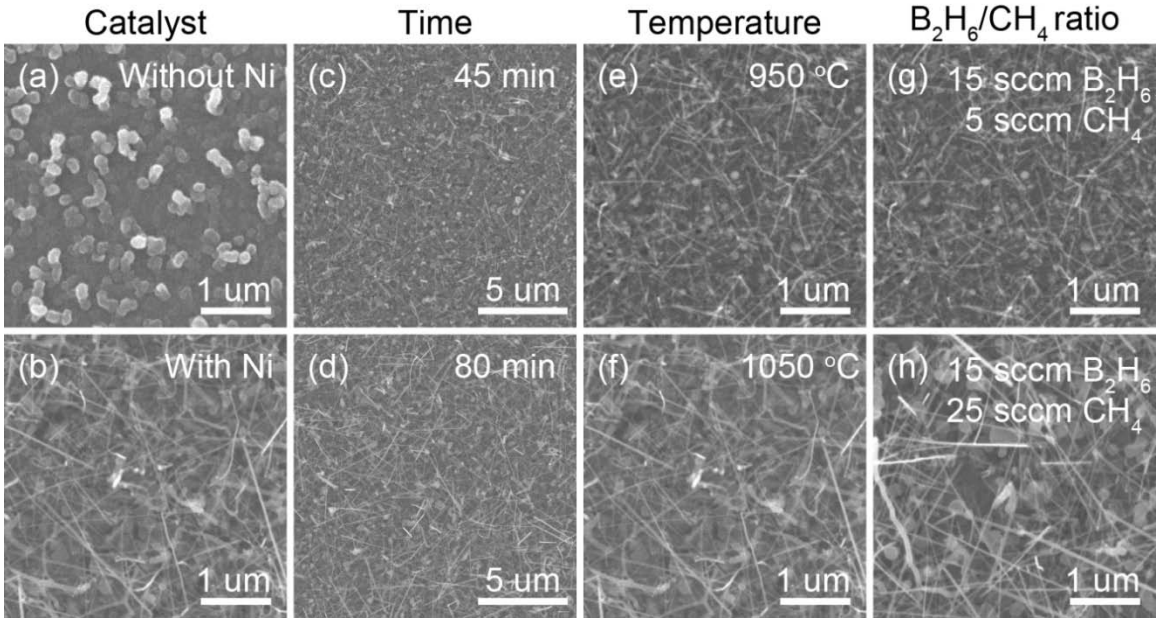

Figure 3.4 Results of controlled synthesis experiments illustrate effects of catalytic materials, reaction time, temperature and flow rate ratio between B_2H_6 and CH_4 on growth of boron carbide nanowires.

3.2.3 Orientation of Planar Defect

The crystal structure of boron carbide can be viewed as a rhombohedral distortion of the cubic close packing (ccp) of B_{12} or $B_{11}C$ icosahedra.[98] The (001) planes of the rhombohedral cell are considered as the close-packed planes in the ccp arrangement. They are stacked by a sequence of ...ABCABC… as illustrated in Figure 3.5 (a). If this normal stacking sequence is disturbed, planar defects such as stacking faults and twins can be formed. Due to its relatively lower stacking fault energy,[99] twins and stacking faults are commonly observed in bulk boron carbide, such as sintered samples[100-102] and boron carbide particle reinforced metal matrix composites.[103] For example, a high density of (001) twins and stacking faults were observed from hot-pressed $B_{13}C_2$ samples.[101] A follow-up simulation work on HRTEM imaging showed that the twin plane passes through the center of the icosahedron instead of being translated half-way between the rows of icosahedra parallel to (001) plane.[102] The introduction of a (001) twin plane through the icosahedron distorts the inter- and intra-icosahedral bonding, which could lead to increased bipolaron hopping and affect relevant transport properties.[102] Twins formed in bulk boron carbide are usually deformation twins.[100,103] Their formation can be partly attributed to the localized stress state induced during complicated synthesis processes (e.g., milling, hot pressing).[103] Observation of twins and stacking faults have also been reported for some boron carbide low-dimensional nanostructures, such as whiskers,[104-106] nanowires,[81,107,108] platelets[104] and sheets.[109] However, no detailed and systematic documentation such as those discussed below can be found.

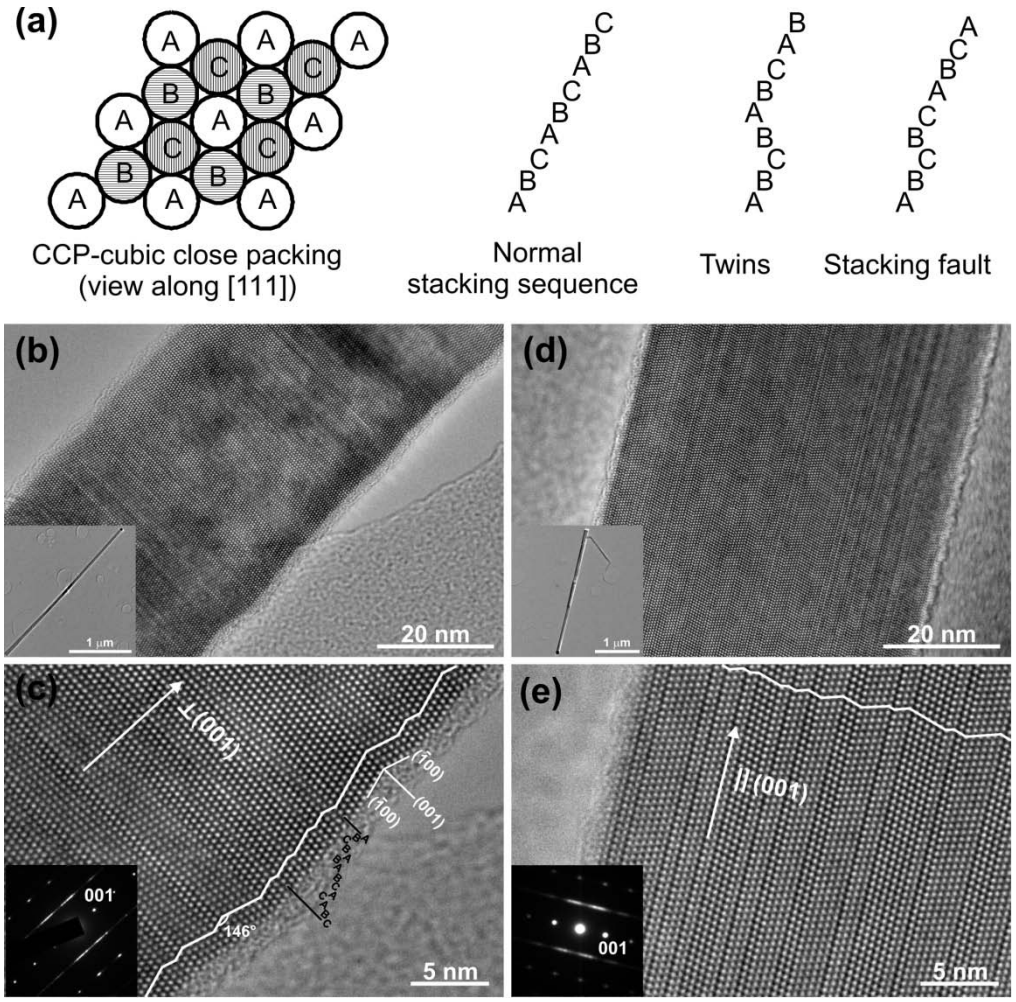

Figure 3.5 (a) Schematic drawing about the cubic close packing structure and the stacking sequences for normal crystal, twins, and stacking fault. (b)-(e) Atomic structure of TF and AF nanowires.

In the present work, more than one hundred nanowires were carefully examined by TEM. To reveal whether the nanowire has structural defects or not, wide angle of tilting was done on each nanowire during TEM examination. Based on the geometrical relationship between the fault plane and the growth direction of the nanowire, the faults can be categorized into transverse faults (fault plane ⊥ nanowire growth direction) and axial faults (fault plane || nanowire growth direction). Figures 3.5 (b) and (c) show a

nanowire with transverse faults in which variable width twins and stacking faults are revealed. The faults have atomic sharp boundaries, indicating they are not deformation faults but growth faults.[103] The white line helps the visualization of the zigzag facets on the wire side surface. These facets are (100) planes. The marked rotation angle is approximately 146°, twice of the inter-planar angle between (001) and $(\bar{1}00)$ planes (73°). The two crystallographic equivalent planes: (001) and $(\bar{1}00)$ have highest planar density in the rhombohedral lattice. Therefore, they are with lowest surface energy and can be energetically more favorable to form during growth. For a portion of the nanowire, the disturbance of stacking sequence is labeled. The new stacking sequence is ABCBABABCA/CABC where the representative microtwinned region is underlined and one intrinsic stacking fault is illustrated by /. Figures 3.5 (d) and (e) show a nanowire with axial faults. Similar to transverse faults, these axial faults consisted of variable width twins and stacking faults. The side surfaces are (001) planes. No clear five-fold cyclic twinning structures as reported previously for boron suboxide[110] and boron carbide nanowires[81] were observed in our nanowires.

3.3 Summary

The approach to synthesize boron carbide nanowires at a low temperature has been discussed. Interestingly, two orientations of planar defects can be observed under TEM. Since the two orientations of planar defects would have different impacts on the properties of boron carbide nanowires, it is very important to know the growth mechanism for each of them and if the defects exist in all nanowires.

CHAPTER 4: GROWTH MECHANISM

In order to achieve the controlled growth and tell the structure-property relationship, the formation mechanism for the boron carbide nanowires, including two orientations of planar defects (TF and AF), needs to be fully understood. In this chapter, the growth mechanism for TF and AF nanowires will be discussed, along with the catalytic materials, growth directions, and kinking structures.

4.1 Growth Mechanisms for 1D Nanostructures

There are some classic methods to grow 1D nanostructures, such as vapor-liquid-solid (VLS), vapor-solid (VS), and solution based methods.

4.1.1 Vapor-Liquid-Solid (VLS) Method

The VLS technique was first introduced by Wagner and Ellis to grow Si whiskers.[95,111] Before reaction, Au nanoparticles are deposited on the substrate to form Au-Si alloys, whose melting point is much lower at the eutectic composition. As shown in Figure 4.1, when the vapor source ($SiCl_4$ and H_2) enters the reaction chamber at a temperature above the eutectic temperature, Si is dissolved into the liquid Au-Si alloy from the vapor state. The amount of Si is higher at the catalyst surface, so diffusion of Si happens from the catalyst surface to the liquid-solid interface. As a result, Si is precipitated at the interface from of the supersaturated alloy and the one-dimensional (1D) nanostructures are formed. The name VLS is derived from the states of source materials during growth.

Catalyst is the key factor in a VLS growth. It must be selected in such a way that the grown material and the catalyst can form an alloy with a lower eutectic temperature (below the maximum heating temperature of the furnace), although it has been reported that the melting point of Au particles is reduced when the diameter goes to nanoscale.[112] Therefore, the absorption, diffusion, and precipitation of the source material can happen within the catalyst, as shown in Figure 4.1 (c). Sometimes, the catalyst can also be in a partial-molten or solid state at lower temperature. As a result, it becomes faceted, instead of a hemispherical shape (Figure 4.1 (d)). It is considered as a vapor-solid-solid (VSS) growth in this case. The surface diffusion plays an important role because diffusion through the catalyst is limited by the solid catalyst. Since it is the catalyst that leads the growth of nanowire, the diameter of the nanowire is basically determined by the diameter of the catalyst.

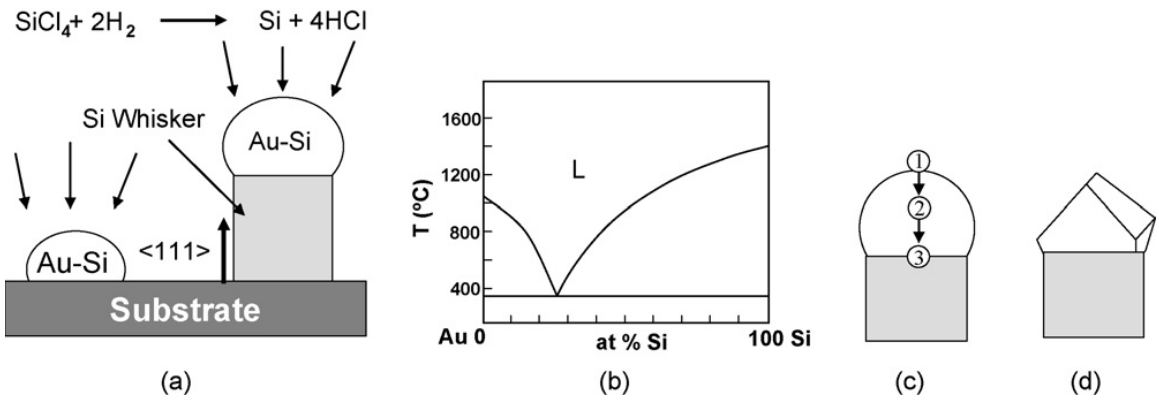

Figure 4.1 VLS growth of Si nanowires (a) Growth procedure. (b) Phase diagram of Au-Si system. (c) The absorption, diffusion, and precipitation of the source material. (d) Growth from a solid-state catalyst.[113]

4.1.2 Vapor-Solid (VS) Method

Similar to the VLS, the VS method is also using vapor sources to grow nanowires, but without catalyst being involved. This method is widely used to grow metal oxide nanowires. The vapor sources can be created by thermal evaporation or chemical reaction. For example, growth of 1D metal oxide nanostructures was reported by heating the commercial metal oxide powders at a high temperature.[114] A temperature gradient is critical because the source material needs to be heated at the temperature slightly lower than its melting point and the temperature of substrate needs to be even lower for the deposition of the vapor sources. Other experimental parameters, such as flow rate, pressure, and evaporation time, are also important not only for the growth, but also for controlling the morphology of the product. Since there is no catalyst to lead the growth, various morphologies of the product have been found.[115] It was believed that the degree of supersaturation has a major impact on the morphology of the product. Whiskers tend to grow under a lower supersaturation, while bulk crystals result from higher supersaturation.[116]

Without catalysts, the ways 1D nanostructures grow are different from that of VLS. Deposition an atomic layer at once is rarely seen because it needs more energy. Thus, the 1D nanostructures grow by the help of atomic steps, screw dislocations, and twin boundaries (Figure 4.2). The basic idea is to introduce more nucleation sites which absorb the vapor sources. So the crystal growth happens due to the propagation of those sites.

Sometimes, additional materials are mixed with the source powders to help to generate the vapor sources.[117] In the case of growing ZnO nanowires, carbon powders

can be added with ZnO to reduce ZnO to Zn. The generated Zn is vaporized and condensed into droplets in the lower temperature region. As shown in Figure 4.2 d, those droplets can act as catalyst for the nucleation of ZnO. This method is called “self-catalytic growth”.

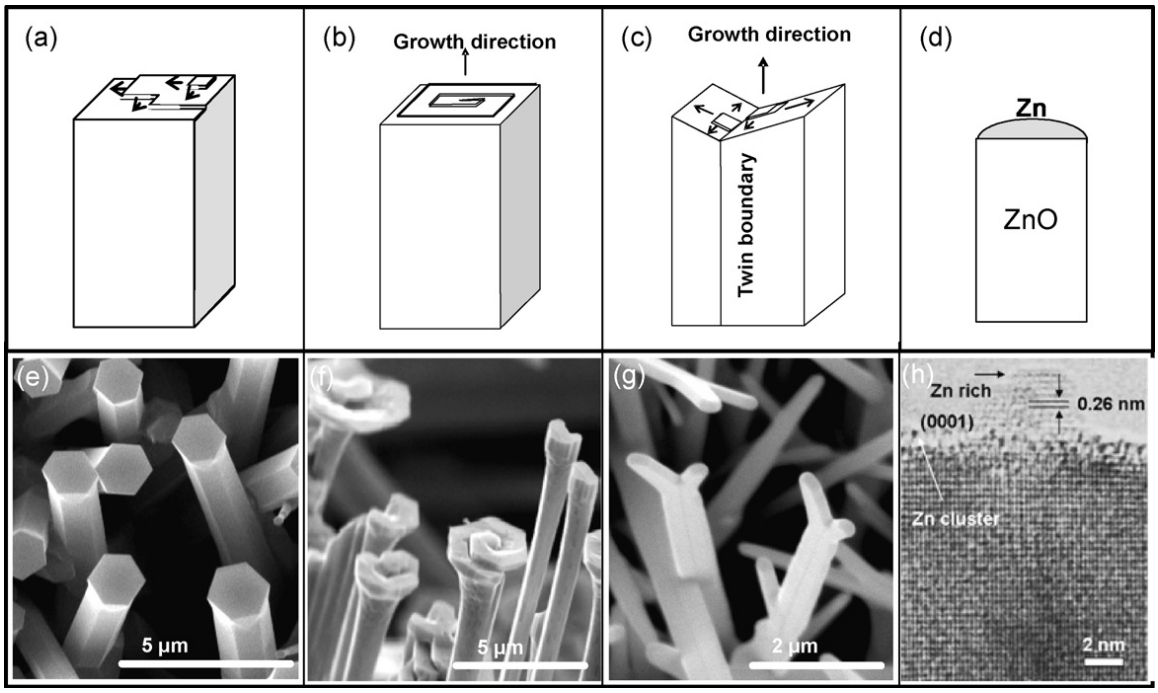

Figure 4.2 Approaches for the growth of the 1D nanostructures using VS method. (a) and (e) Atomic step growth. (b) and (f) Growth results from screw dislocation. (c) and (g) Twining induced growth. (d) and (d) Self-catalytic growth.[113,118]

4.1.3 Solution-Based Methods

1D nanostructures can also be synthesized by reactions in the solution. The solution method is considered to have the advantages of mass production and low cost, with the drawback of relatively poor crystallinity. The common ways of growing 1D

nanostructures in the solution are metal-catalyzed solution-liquid-solid (SLS) growth[119,120] and template-oriented growth.[121,122]

The growth mechanism of SLS growth is similar to the VLS growth. The source molecules generated by reaction with solution are absorbed by the metal catalysts, which leads the growth subsequently. Si nanowires with uniform diameters within 5 nm were observed by SLS growth due to the available smaller size of the Au particles (~2-3 nm in diameter).[119]

Another way to grow nanowires in solution is to use template, such as anodized alumina membranes and polymer porous membranes, to direct the growth.[121,122] After deposition, the template needs to be removed, and the as-synthesized nanowires are usually polycrystalline.[116] Surfactants can also be used to guide the 1D growth. They can be attached on specific surfaces of the crystal, so that growth of those surfaces is prevented. The surfactants, acting as a soft template, can be removed afterwards to obtain the nanowires (Figure 4.3).

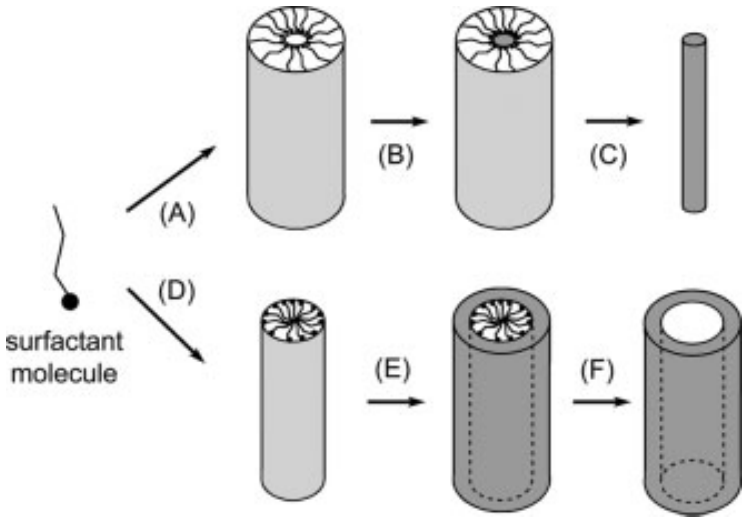

Figure 4.3 Nanowires growth caused by surfactants. (A) Surfactant form a cylindrical micelle. (B) Growth of nanowire within the micelle. (C) Removal of the micelle. (D)-(F) Similar to the process in (A)-(C), surfactants with the “heads” facing outwards lead to the growth of a tube.[116]

4.2 Catalyst

Substrate should have a major impact on the epitaxial growth. But the boron carbide nanowires are not epitaxially grown. That is why catalyst is discussed first.

As mentioned in chapter 3, the boron carbide nanowires grow via the VLS mechanism. The catalyst is critical for the growth control. The best way to investigate how the catalyst leads to the growth is to use *in situ* TEM to take real time images.[123-127] By looking at the evolution of the catalyst (liquid or solid) and the propagation of the interface, the dynamic growth process can be better revealed. Videos can also be taken under TEM to record the growth process.[125,126] However, due to the limitation of the TEM used in this work, images were taken after growth.

4.2.1 Shape and Interface

Careful TEM work was done on hundreds of nanowires. By looking at the shapes and interfaces of the catalysts, the states (liquid or solid) during reaction can be determined, although the catalysts being observed during TEM are the ones after reaction.

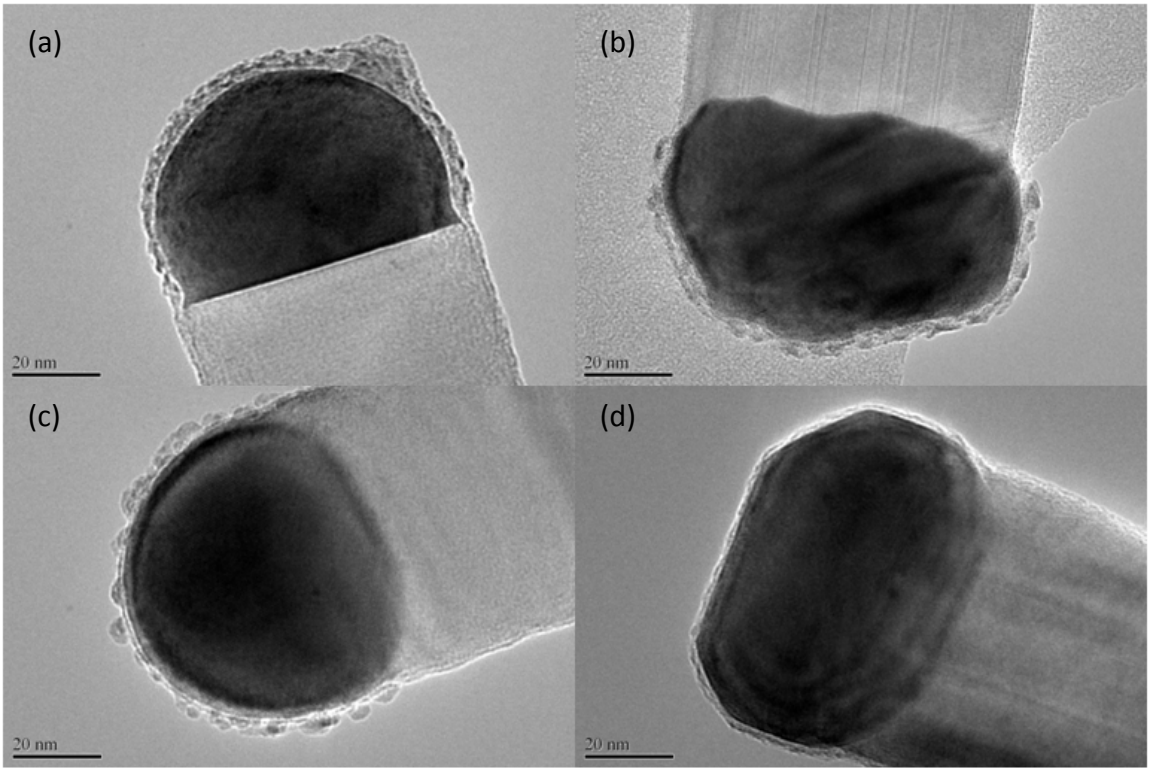

Figure 4.4 Shapes of catalysts and interfaces for the TF and AF nanowires. (a) Well tilted TF nanowire. (b) Well tilted AF nanowire. (c) TF nanowire viewed from a random direction. (d) AF nanowire viewed from a random direction.

According to the TEM results on catalysts (Figure 4.4 (a)), when the zone axis is tilted to the [010] direction (the direction when planar defect can be clearly seen), TF nanowires tend to have a hemispherical-shaped catalyst and a flat interface. That indicates the growth happened via layer-by-layer deposition at the interface and the catalyst was in a molten state during the growth. The interface is (001) plane with planar defects, which means growth is realized by the stacking of the defect plane. Consequently, when there is a twin plane or stacking fault, it leaves a zig-zag shape wire boundary, as given in Figure 3.5. On the other hand, when viewed from [010] direction, most of the AF nanowires have irregular-shaped catalysts and a zig-zag interface (Figure 4.4 (b)). It

looks like an “irregular” shape, but actually the zig-zig interface is composed of several segments along the original and twinned (100) planes of the boron carbide. The propagation of those (100) planes leads to the growth. The faceted catalyst is believed to be in the solid or partially molten state during growth. However, if the viewing directions are tilted away from [010] direction of the nanowires, the interfaces are not that clear anymore, but the spherical or faceted shape can still be seen, as shown in Figure 4.4 (c) and (d). Thus, the TF nanowires grow via VLS mechanism, whereas AF ones grow via VSS mechanism. Both TF and AF nanowires can be found in the same batch.

The reason of the co-existence of both TF and AF nanowires might be the fluctuation of local temperature during growth. The solidification process has been recorded by *in situ* TEM observation.[125,128-130] It was shown clearly that the hemispherical-shaped liquid catalyst became faceted when temperature was decreased. Similar phenomenon has been seen in our experiments. At a higher heating temperature (1050 °C), both TF and AF nanowires can be found. When temperature was reduced to 950 °C, most of the nanowires are found to be AF. Therefore, temperature is the important factor that controls the states of catalyst and the orientations of planar defect. Another reason might be the fluctuation of source materials. With a phase diagram in mind, when the composition shifts away from the eutectic point, the liquid state alloy would solidify. However, it needs to be verified by systematic work in the future.

4.2.2 Phase Identification

Given that the TF and AF nanowires are guided by liquid and solid catalysts, respectively, it is very important to identify the phases of the catalysts. EDS and diffraction patterns were used to figure out the structures of the catalysts. When it comes

to the identification of an unknown material, one single diffraction pattern is far from enough. A series of diffraction patterns need to be taken systematically. The strategy is that an EDS spectroscopy can be taken to indicate the existing elements in the catalyst, then the specimen needs to be tilted within a specific lattice plane, usually the low index one, so that a series of diffraction patterns can be taken with the same tilting direction. When several low index zone axes are found within that specific plane, diffraction patterns can be analyzed and a material can be found to match all the patterns. Based on the indexation of each diffraction pattern, the angle for each tilting step can be theoretically calculated. This theoretical angle is compared with the actual tilting angle from TEM readings. If all the theoretical angles match the actual angles, the material found in the previous step can be verified. If the angles do not match, it means the assigned material is incorrect.

EDS results show that boron and carbon can be found in the catalysts. Also, if quartz tube and boat are used, abundant silicon can be found in the catalyst. To minimize the possible elements in the crystalline phase, data used in this section are all taken from the nanowires synthesized with alumina tube and boat. Thus, the phase to be identified can be any combination of Ni, B, C, and perhaps O.

Following this strategy mentioned above, a lot of efforts were put to take diffraction patterns on the catalysts from TF nanowires. Surprisingly, the diffraction patterns do not match any of the record in the JCPDS database, but one of the diffraction pattern does look like the pattern of a hexagonal lattice from [001] direction. Because there is no available record matching these patterns, we assume this is a hexagonal phase and try to see if it can be proved. One major challenge is that the specimen holder is

limited to tilt ± 30° in each direction, so that the diffraction patterns cannot cover all the lower index zones each time. What we did was to take all the obtainable patterns on each catalyst from TF nanowires and try to find the same pattern from the data taken on different nanowires to connect patterns. By doing this, we might draw a diffraction map including all the lower zone axes. Fortunately, the map of diffraction patterns given in Figure 4.5 can be drawn by connecting the diffraction patterns from several sections. Based on the measured *d*-spacing in the diffraction patterns, the catalyst for TF nanowires is identified as a hexagonal nickel boride phase with a=8.2 Å and c=3 Å.

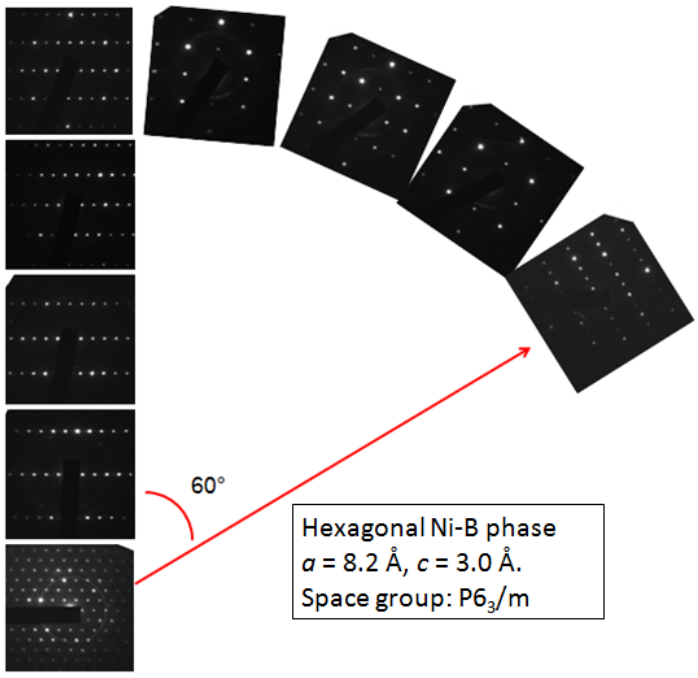

Figure 4.5 A series diffraction pattern taken on the unknown catalyst, confirming the hexagonal lattice structure.

In the case of the catalysts on AF nanowires, same strategy was applied. Those catalysts are found to be nickel boride (Ni_4B_3) with an orthorhombic structure.

As mentioned in 4.2.1, most of the orthorhombic phase can be found with a lower synthesis temperature (950 °C). If the temperature is increased to 1050 °C, more hexagonal phase catalyst shows up. That can be attributed to the difference of the melting temperatures for those two phases. The melting temperature of orthorhombic phase is 1018 °C, while the hexagonal phase might have a lower melting temperature. Therefore, the orthorhombic phase becomes solidified first and leads to the growth of AF nanowires when the temperature is decreased. The synthesis temperatures and catalyst statuses for TF and AF nanowires are summarized in Table 4.1.

Table 4.1 Dependence of TF and AF nanowires on the growth condition, especially the catalyst.

	TF	AF
Synthesis temperature	1050 °C	950 °C
Catalyst shape	Hemispherical	Faceted
Catalyst state	Liquid	Solid or partially molten
Catalyst phase	Hexagonal	Orthorhombic
Interface	Flat	Zig-zag

4.3 Growth Directions

Although nanowires prefer to grow in the direction that minimizes the total energy, they have been observed to grow in different directions.[131] Researches focusing on the growth direction of nanowires show that it is dependent on nanowire's diameter,[132-136] synthesis temperature,[137,138] total pressure,[139,140] and partial pressure of the

source materials.[141-143] In this study, the first 130 characterized nanowires were selected to see the diameter distributions for TF and AF nanowires (Figure 4.6). The nanowires being characterized under TEM were randomly chosen. There are 59 TF and 71 AF nanowires totally and most of the nanowires have diameter between 30-90 nm. There is no clear diameter-dependent growth direction, indicating that the growth direction of boron carbide nanowires is mainly controlled by the state of catalyst, which depends on temperature and pressure.

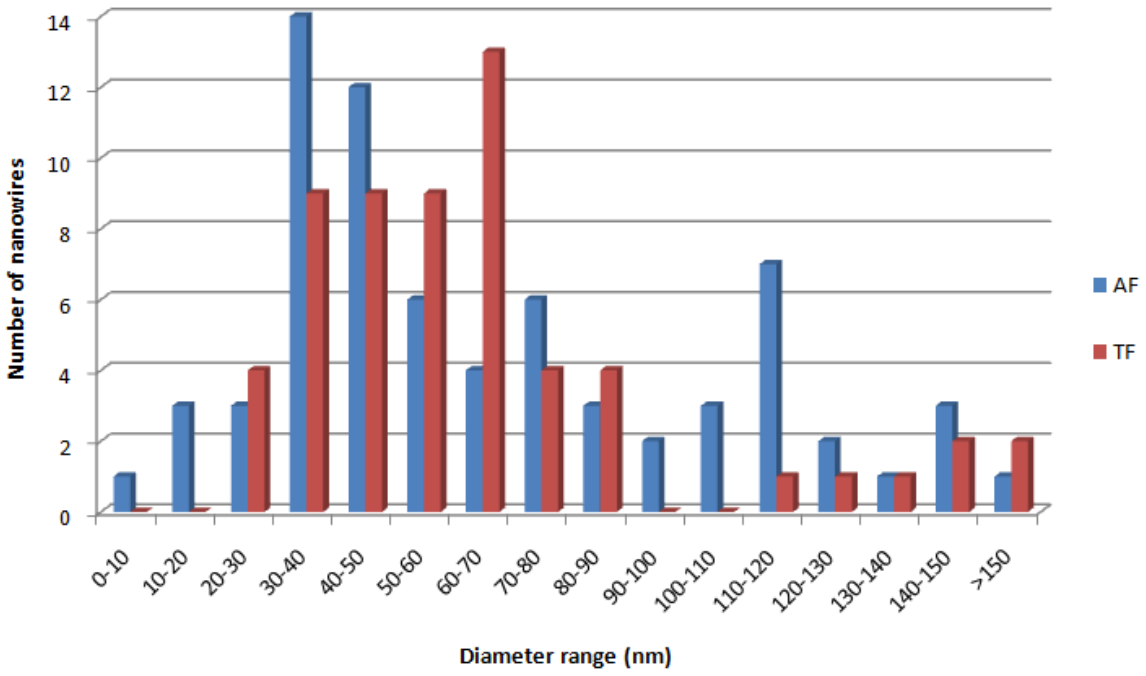

Figure 4.6 Diameter distributions of TF and AF nanowires.

It is known from chapter 3 that TF nanowires grow perpendicular to the (001) plane and AF nanowires grow parallel with (001) plane. But the actual growth directions need to be specified to better understand the growth mechanism and to help the further

study given in the next chapter. Although the term “growth direction” is frequently used to explain the growth of 1D nanostructures, sometimes it is not used correctly.[144] The situation is caused by two problems.

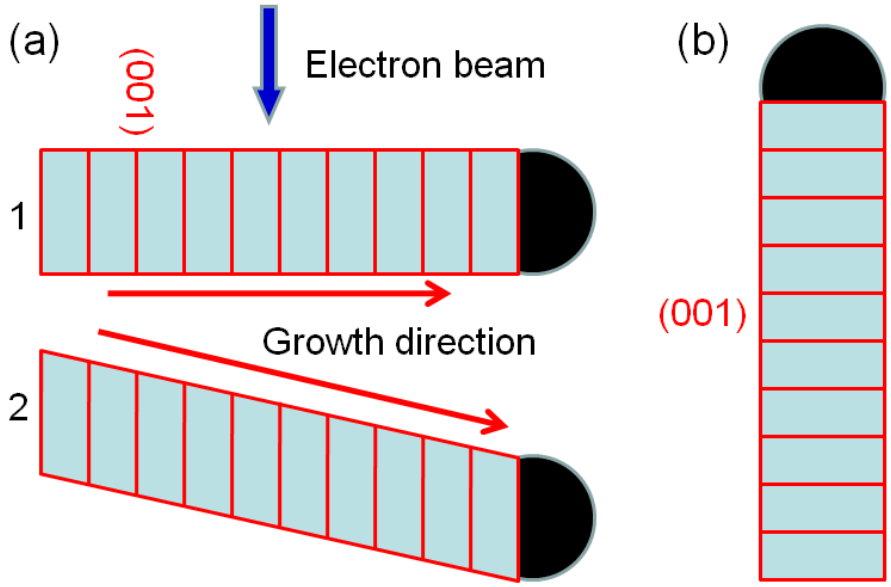

Figure 4.6 Illusive “growth direction” happens when the growth direction is not perpendicular to the incoming electron beam.

First, a TEM image is actually a projection image from the crystal according to the orientation it is placed inside TEM. The growth direction is correct only when it is perpendicular to the electron beam. Like the schematic drawings given in Figure 4.6, there are two nanowires with different growth directions. Assume that the nanowire-catalyst interfaces for the two nanowires are the same plane (*e.g.*, (001) plane in a cubic lattice). From the labeled electron beam direction, what we see on the screen is the same (Figure 4.6 (b)). Therefore, [001] direction could be considered as the “growth direction”

for nanowire 2 by mistake. This happens all the time whenever conclusions are drawn based on the diffraction pattern from one single direction. To solve the problem, the diffraction patterns have to be taken from two or more zone axes.

The second problem arises from the misunderstanding of the seven crystal systems. For example, assume the nanowire 1 in Figure 4.6 has a cubic structure. Then its growth direction, normal to the (001) plane, is [001] direction. But the situation when direction is the normal direction for the plane with the same index only works with cubic structure. The growth direction of a nanowire with any other crystal systems cannot be indexed this way. Take the rhombohedral boron carbide crystal for example (Appendix I), the normal direction for (001) plane is $[\overline{0.292}, \overline{0.292}, 1]$, instead of [001]. In reality, the determination of growth direction usually involves the comparison of the TEM image with its diffraction pattern. If the nanowire is verified to be perpendicular to the electron beam (nanowire 1 in Figure 4.6), and the image of nanowire is passing the (001) diffraction spot in the pattern, the more accurate way to describe the growth direction would be: it is normal to the (001) plane. It needs to be extremely careful when talking about growth direction based on the diffraction spots.

In the case of TF nanowires, TEM images and diffraction patterns were taken along [1-10] and [010] directions while it was tilted within the defect plane (001). It can be seen from Figure 4.7 that when the nanowire is tilted within (001) plane, its growth direction is always the normal direction of the (001) plane. It means that the normal direction of (001) plane is the true growth direction, not the illusive one. This plane normal, which is the growth direction for TF nanowires, is calculated as $[\overline{0.292}, \overline{0.292}, 1]$ (See Appendix I).

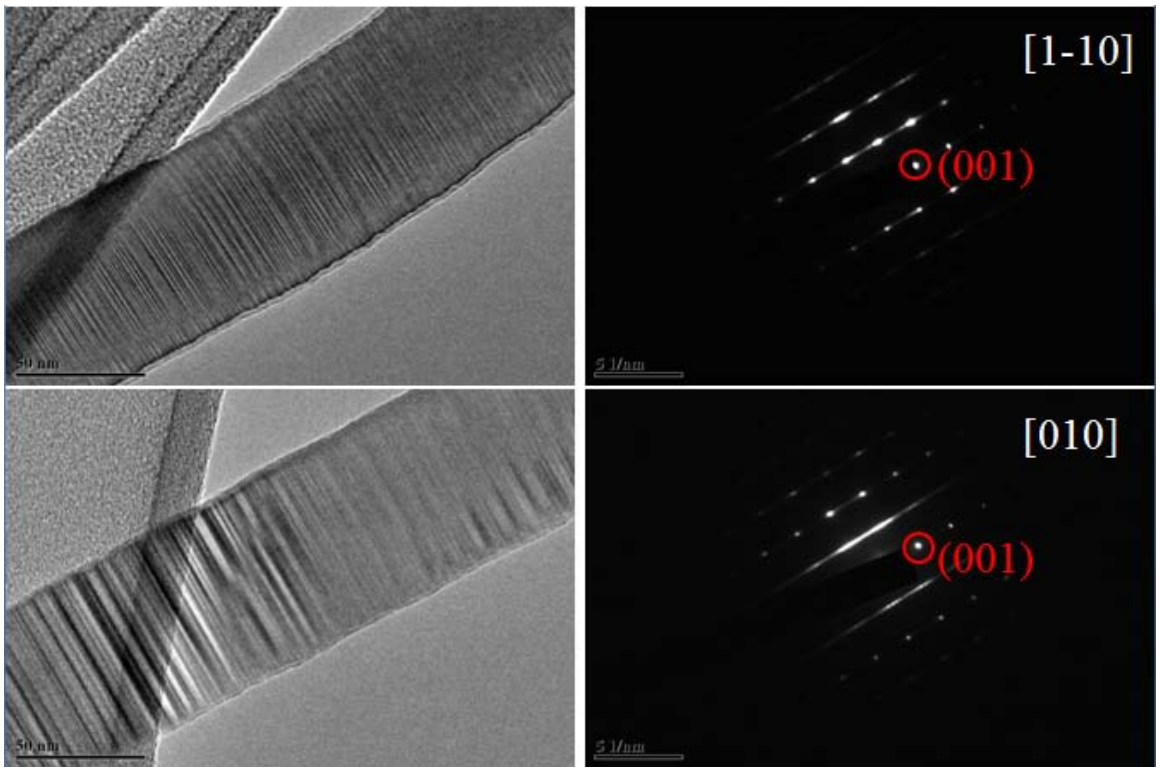

Figure 4.7 TEM images and diffraction patterns taken from the [1-10] and [010] directions of a TF nanowire.

Following the same strategy, an AF nanowire was tilted to [010] and [001] directions (Figure 4.8). The growth direction is within (001) and (010) planes from [010] and [001] directions, respectively. The intersection of those two planes is [100] direction, so that is the growth direction for AF nanowires.

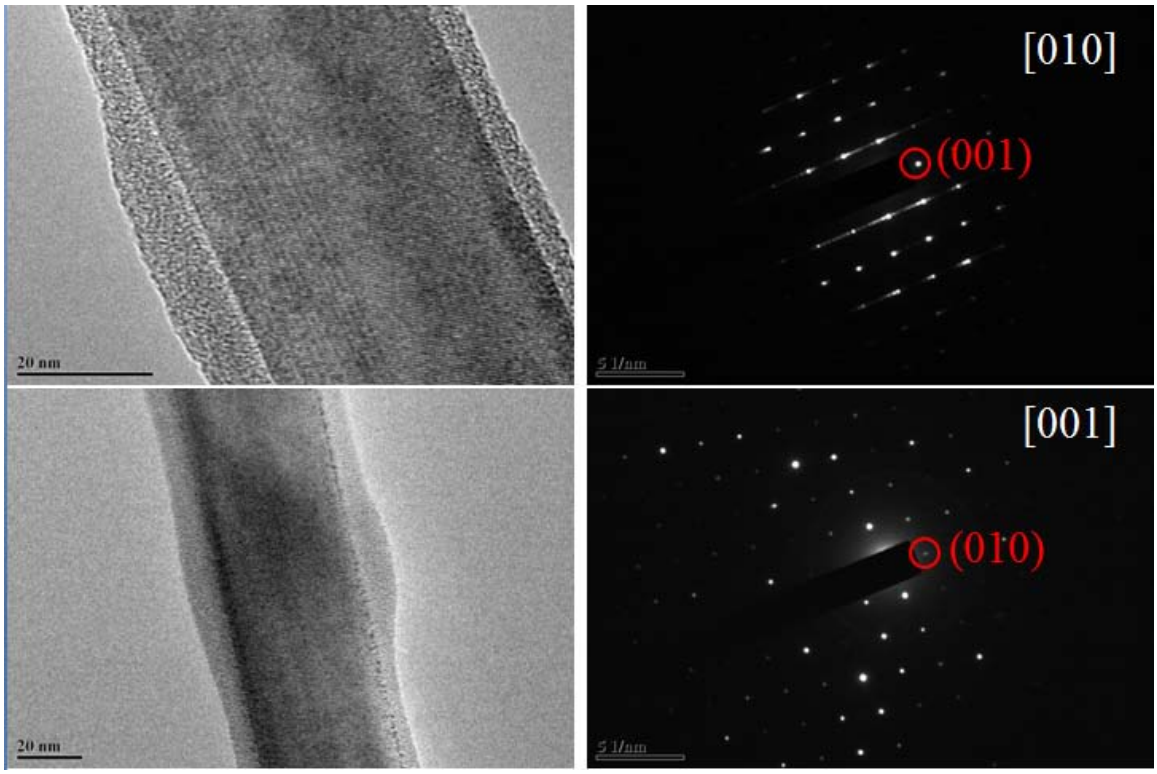

Figure 4.8 TEM images and diffraction patterns taken from the [010] and [001] directions of an AF nanowire.

4.4 Other Structures

Catalyst migration and shrinking during the VLS growth have been observed under SEM or TEM, which leads to tapered nanowires, kinks, and branches.[145-147] A shrinking catalyst over time leads to the tapered nanowires. The ostwald ripening effect was observed for the catalysts. While the smaller ones are being consumed gradually, the diameter of the nanowire decreases as well.[145] If the catalyst migrates from the top to the side wall in a sudden, a kink is triggered. The cause of kinks is considered to be change in temperature,[148-150] high vapor pressure,[141,150,151] and change in vapor pressure.[139,152,153].

Tapering is not observed in boron carbide nanowires, so examples of kinks and branches will be given in the following sections. Sometimes the nanowires change their

growth directions, giving rise to the kinked structures. As discussed above, normally nanowires have only two growth directions (TF and AF). The growth direction changes happened from a TF nanowire to another TF one (TF-TF), or from an AF nanowire to the TF one (AF-TF). It can be seen from Figure 4.9 that for the TF-TF kink, there is a joint area (labeled in red loop) between two arms of TF nanowires. Surprisingly, there is no defect in this area. The (001) and (100) planes of this defect-free crystal are the growth fronts for the two TF arms. The kinking angle is simply the angle between the (001) and (100) planes. That is, as measured, 107°. Kink like this does not have a 90° angle, which implies it is not due to the catalyst migration towards the side wall. Instead, this TF-TF kink comes from the uneven growth rates from different facets. What happened within the joint area is the process of termination of growth normal to the original (001) plane and the initiation of the growth normal to the new (100) direction. A shape change of the catalyst might be involved to accommodate the two planes. This has been recorded by real time TEM[150] and explained by a simulation model.[154]

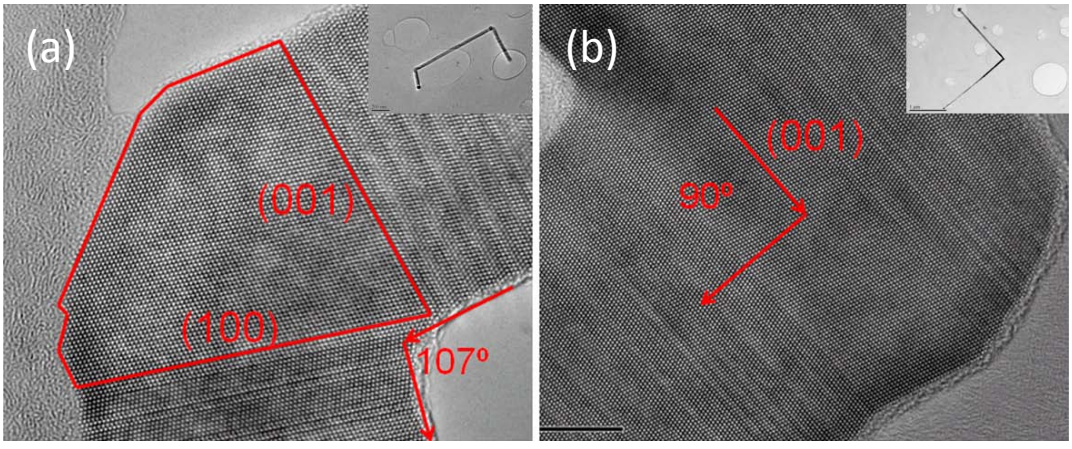

Figure 4.9 Two types of kinks. The arrows are point to the growth direction in each segment. (a) TF-TF kink. (b) AF-TF kink.

On the other hand, the AF-TF kink has a direction change of 90°, which means the TF segment grows directly on the side wall of AF segment. Apparently, this results from the catalyst migration from the top of AF segment to its side wall. If the partially molten catalyst becomes a liquid droplet, it is not stable anymore on the zig-zag supporting interface and can slide along the side wall. That leads to the AF-TF kink, but the orientation of defect plane is not changed. Figure 4.10 gives the evidence of catalyst migration from the top of an AF nanowire to its side wall. The shape of the catalyst has become spherical. If reaction continues, an AF-TF kink will be obtained from the side wall growth.

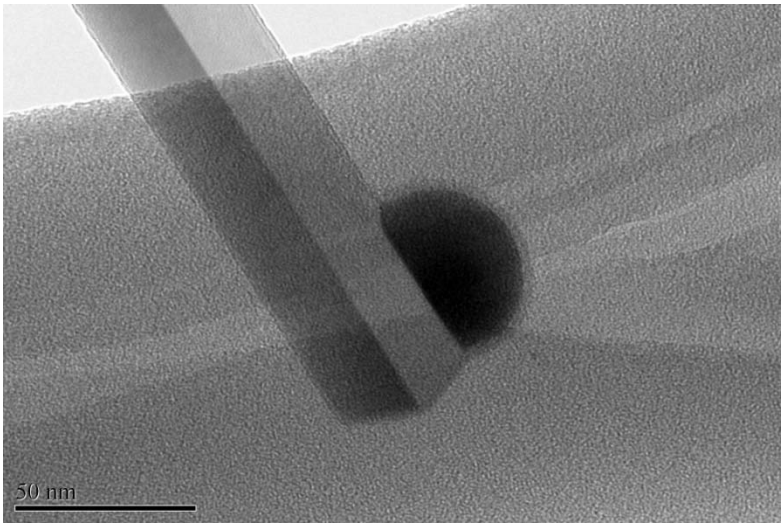

Figure 4.10 Catalyst migration to the side wall of an AF nanowire.

Catalyst can also be spitted at the joint area of the TF-TF kink. As a result, a boron carbide “tripod” is created with a stem growing in the normal direction of (001) plane and two arms growing towards the normal directions of (100) and (010) planes.

The angle between each two segment is 107°, same as TF-TF kink. This could be the building block of boron carbide branches.

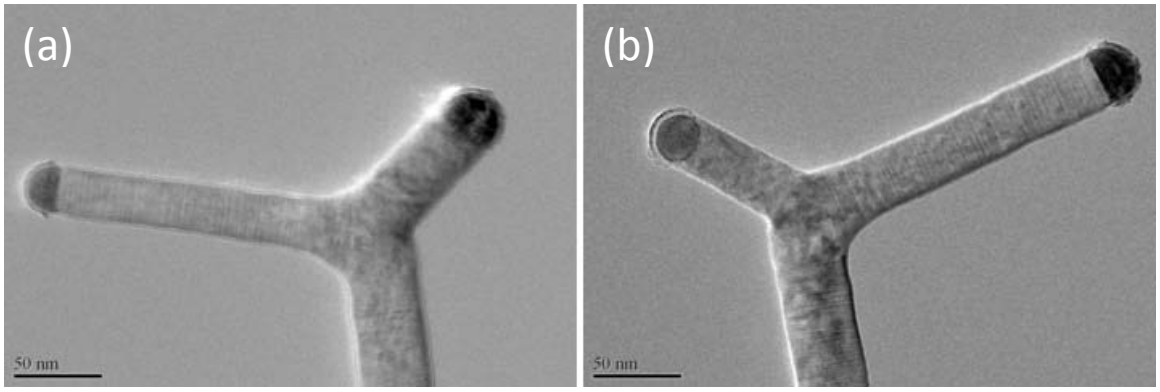

Figure 4.11 Boron carbide “tripod” made of TF-TF kinks. Assume the growth direction of the stem is normal to the (001) plane. (a) Viewing from [100] direction. (b) Viewing from [010] direction.

4.5 Summary

The growth of boron carbide nanowires was achieved by VLS mechanism. The catalysts on the tips of nanowires play an important role on the growth direction. They were identified as two Ni-B phases. The liquid hexagonal phase catalysts lead to the growth of TF nanowires. While the solid orthorhombic phase catalysts lead to the growth of AF nanowires. The growth directions for TF and AF nanowires were specified by TEM observation from more than one direction. The unstable catalyst could give rise to the kinks and branches.

CHAPTER 5 “INVISIBLE DEFECTS”

As discussed in the previous chapters, planar defects were found within the as-synthesized nanowires. This observation is consistent with what people found in bulk boron carbides.[63,68,69,71,72,75] The existence of planar defects with a high density is due to the relatively lower stacking fault energy for the (001) plane.[63] As a result, defects only happen within the (001) plane. Due to the three-fold symmetry of its rhombohedral unit cell, there are three equivalent lattice planes that can be the defect plane: (100), (010), and (001).

The existence of defects would have some major impact on the mechanical,[155] electrical,[156] thermal,[157] and optical[158] properties of 1D nanostructures. Thus, it is crucial to know their nature such as existence, distribution and orientation within each nanowire to establish the structure-property relations.

Transmission electron microscope (TEM) images and the diffraction patterns were used to analyze those nanowires. However, due to the sophistication of the TEM technique, sometimes, experimental artifacts could be erroneously interpreted or lead to controversy.[144,159-162] To date, most planar defect-related studies have been focused on 1D nanostructures made of silicon, silicon carbide, III-V (*e.g.*, GaAs and InP), or II-IV compounds (e.g., ZnO and CdSe), whose crystal structures are either cubic or hexagonal.[160-167]

In this chapter, more TEM examination and a model simulation will be addressed to gain a deeper understanding of the nature of planar defects in boron carbide nanowires to answer to questions. (1) Do planar defect-free boron carbide nanowires really exist? (2) If planar defects exist in all of our as-synthesized boron carbide nanowires, can their orientations be determined from TEM results showing no characteristic features (*i.e.*, results from the "off-zone" directions as discussed later)? It is expected that different orientations of planar defects could have distinctive effects on the properties of these nanowires, similar to that physical properties of superlattices could be very different along their in-plane and cross-plane directions.[33,168] Therefore, it is important to know the fault orientation of each boron carbide nanowire.

The as-synthesized nanowires were first transferred from substrates to a small block of elastomeric polydimethylsiloxane (PDMS) by a gentle stamping process. Individual boron carbide nanowires were selected and picked up by a sharp probe mounted on an in-house assembled micromanipulator and then transferred to a TEM grid layered with lacy carbon support film. This operation was done under an optical microscope equipped with long working distance objective lenses. In each mesh of the TEM grid, only one nanowire was placed. During TEM study, each nanowire was subjected to a full range of tilting examination. The tilting range was set by the configuration of our microscope, as described later. For the nanowire that appeared to be planar defect-free in the initial round of TEM examination, it would be picked up by the sharp probe and repositioned onto another region of the lacy carbon support film for reexamination. This challenging and tedious reposition-reexamination process was

repeated several times for some nanowires to reveal the true nature of planar defects inside them.

A JEOL double-tilt holder was used to realize the wide angle of tilting (±30° in both *X* and *Y* directions). Software packages (CrystalMaker® and SingleCrystal™) were used to construct, display and manipulate three-dimensional models of boron carbide unit cell and nanowires, as well as to simulate corresponding electron diffraction patterns.

5.1 "Hidden" Defects

5.1.1 The Existence of "Hidden" Defects

As described previously,[169] {100}-type planar defects such as stacking faults and twins of variable width are commonly observed from as-synthesized boron carbide nanowires. The planar defects can be further categorized into transverse faults and axial faults, depending on the geometrical relation between the planar defects and the preferred growth direction of a nanowire. Figures 5.1 (a) and (b) show the typical HRTEM images of a TF nanowire with planar defects perpendicular to its preferred growth direction, and an AF nanowire with planar defects parallel to its preferred growth direction, respectively. However, some nanowire seems to be defect-free due to the lack of modulated contrast in the image and streaks in the electron diffraction pattern even after wide angle of tilting, as shown in Figure 5.1 (c). But after tilting the nanowire to a different zone axis, all "hidden" planar defects emerged as clearly shown in Figure 5.1 (d), revealing a TF nanowire. This example undoubtedly demonstrates that one cannot conclude that a nanowire is planar defect-free based on TEM results obtained from one single viewing direction. A full range of tilting examination from multiple zone axes is necessary to obtain a reliable conclusion. Moreover, in specific occasions, even after a full range of tilting examination

limited by the configuration of a microscope, there is still a possibility of neglecting the existence of planar defects. Figure 5.1 (e) is a low magnification TEM image of another boron carbide nanowire. An initial full range of tilting examination suggests that the nanowire is planar defect-free, as shown in Figure 5.1 (f). However, after repositioning the nanowire (Figure 5.1 (g)) and reexamination, the “hidden” planar defects are revealed in Figure 5.1 (h) and the nanowire is identified as an AF nanowire. This example further demonstrates that the existence of planar defects cannot be fully revealed by observation from one single zone axis. In the current study, sixteen planar defect-free-like nanowires were subjected to multiple rounds of reposition and reexamination, and planar defects were seen from all of them eventually. This new finding strongly suggests that planar defects exist in all of our as-synthesized boron carbide nanowires. However, these defects are not always visible from routine characterization.

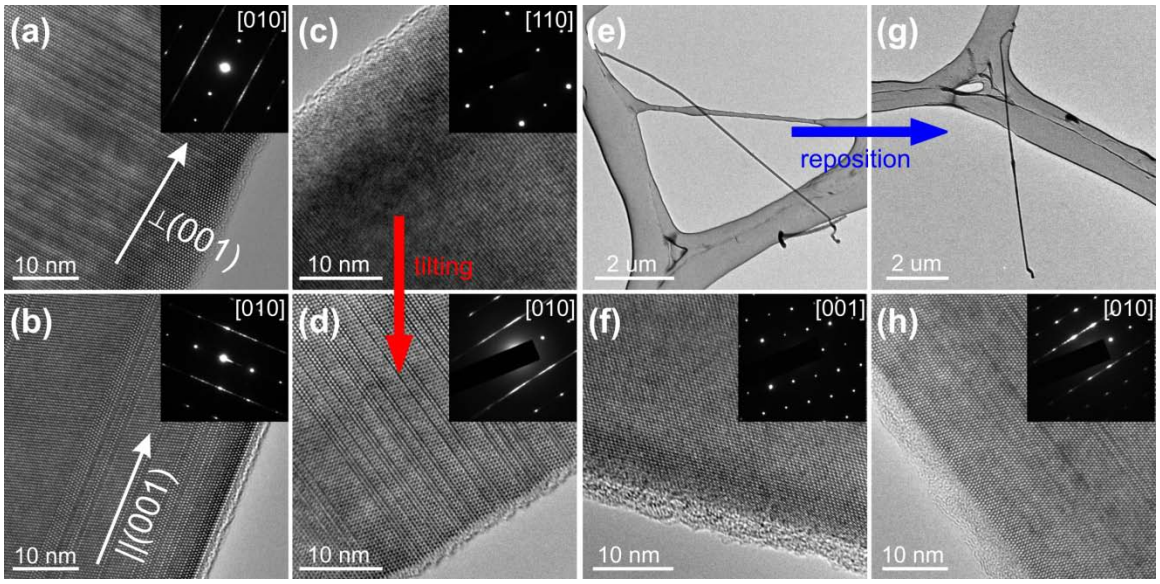

Figure 5.1 Typical TEM results of (a) a TF nanowire whose preferred growth direction is perpendicular to (001) planar defects, and (b) an AF nanowire whose preferred growth direction is parallel to (001) planar defects. TEM results of a nanowire whose planar defects are (c) invisible along the [110] zone axis, but (d) clearly revealed after titling to the [010] zone axis. TEM results of (e) a nanowire whose planar defects (f) are invisible after a full range of tilting examination. The same nanowire (g) was picked up and repositioned by a micromanipulator. Planar defects (h) are now clearly shown.

5.1.2 The Origin of "Hidden" Defects

It is now clear that during TEM examination, planar defects can be easily invisible in boron carbide nanowires. Analysis indicates that the simplified reason for this invisibility is that the viewing direction is not along some specific directions parallel to planar defects.

The crystal structure of boron carbide (Figure 5.2 (a)) can be viewed as a rhombohedral distortion of the cubic close packing (ccp) of B_{12} or $B_{11}C$ icosahedra.[170] The {100} planes of the rhombohedral cell are considered as the close-packed planes in the ccp arrangement. If one stacks the specific close-packed (001) plane (shaded in Figure 5.2 (b)) in an ABCABC… sequence,[169] a planar defect-free structure can be

realized. If this normal stacking sequence is disturbed, planar defects can be formed[169] and designated as the (001)-type. During TEM examination, characteristic features of planar defects can only be seen when the viewing direction is parallel to this (001) plane. In addition, even within the (001) plane, to record TEM characteristic features of planar defects requires viewing along certain lower index zone axes, which further reduces the chance of seeing the defects, as explained below.

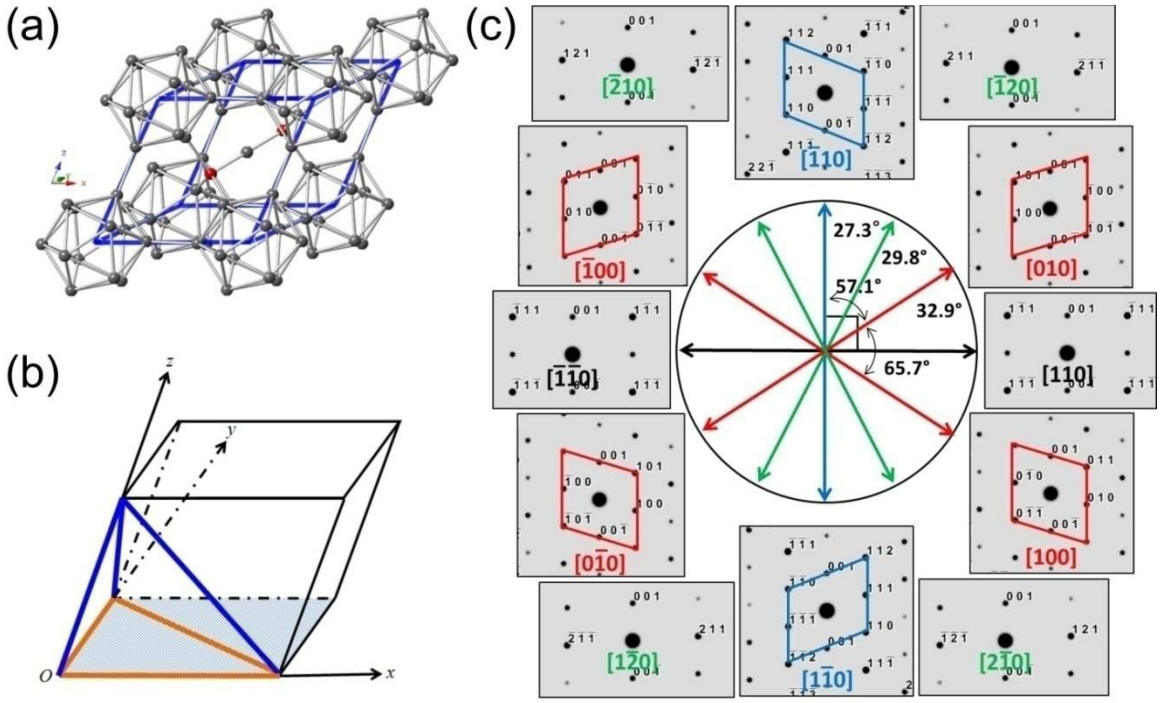

Figure 5.2 (a) The rhombohedral lattice of boron carbide. Eight 12-atom icosahedra locate at the corners and one 3-atom chain occupies the longest diagonal of the rhombohedron. (b) A schematic drawing of the rhombohedral unit cell. The shaded plane is the (001) plane. Within the plane, orange lines represent the three "in-zone" directions: [100], [010] and $[1\bar{1}0]$, along which planar defects can be observed. Blue lines represent the three "off-zone" directions: [001], $[10\bar{1}]$ and $[01\bar{1}]$, from which the planar defects cannot be seen. (c) A roadmap consisting of simulated diffraction patterns of major low index zone axes within the (001) plane. During TEM examination, the roadmap helps the operator to determine whether it is possible to tilt to the desired zone axes.

A roadmap consisting of simulated diffraction patterns of major low index zone axes within the (001) plane is shown in Figure 5.2 (c). During TEM examination, this roadmap can help us to judge if it is possible to tilt to the next zone axis according to the calculated angle between different zone axes. For example, it is nearly impossible to obtain results from both $[\bar{1}10]$ and [010] zone axes on the same nanowire because the calculated inter-axial angle (57.1°) is close to the tilting limit of our TEM specimen holder (60°). In the roadmap, there are four independent patterns such as those from $[\bar{1}10]$, $[\bar{1}20]$, [010], and [110] directions, as grouped in four colors.

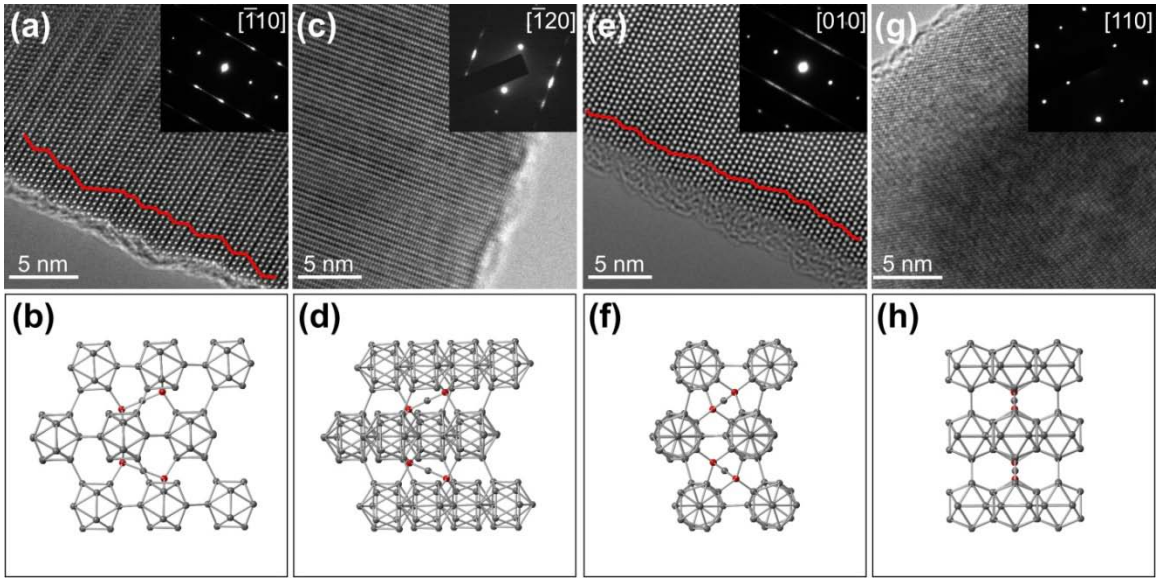

Figure 5.3 Observation of planar defects along the $[\bar{1}10]$, $[\bar{1}20]$, [010] and [110] directions. The four directions are all parallel to planar defects. However, planar defects are clearly visible when viewing along the direction of $[\bar{1}10]$or [010], less distinctive along the $[\bar{1}20]$ direction, and totally invisible from the [110] direction.

During TEM examination, planar defects can be seen along directions of $[\bar{1}10]$, $[\bar{1}20]$ and [010] whose diffraction patterns are asymmetric about (001) plane and with

streaks in them. While viewing along the [110] direction, the layered-faults feature is hidden because of the mirror symmetry (Figure 5.3). In addition, planar defects are more distinctive when viewing along directions of $[\bar{1}10]$ and [010] than that from $[\bar{1}20]$. Therefore, in our real TEM practice, only results from the two independent directions, $[\bar{1}10]$ and [010], are recorded and analyzed.

There are a total of six equivalent $[\bar{1}10]$-type and [010]-type directions in the rhombohedral system, as drawn in orange and blue lines in Figure 5.2 (b). Characteristic features of planar defects can be observed by TEM when the viewing direction is along the rhombohedral axes or the short diagonal within the (001) plane, *i.e.*, the directions of [100], [010] and $[1\bar{1}0]$. These three directions (outlined in orange) are denoted as "in-zone" directions. Meanwhile, the other three directions: [001], $[10\bar{1}]$ and $[01\bar{1}]$, located out of the (001) plane (marked in blue), are denoted as "off-zone" directions, due to the fact that planar defects are invisible from them.

Now the difficulty to visualize planar defects in boron carbide nanowires becomes obvious. If the viewing direction is not parallel to planar defects, the defects will be invisible. In addition, even if the viewing direction is parallel to planar defects, depending on the initial orientation of the viewing direction, planar defects may also not be observed. For example, if the initial viewing direction (*i.e.*, without any tilting of the specimen holder) is along the [110] direction within the (001) plane, it is then impossible to see any characteristic features of planar defects even after a full range of tilting examination. This is due to that approximately ±33° is needed to tilt from the [110] direction to the "in-zone" directions: [010] or [100], according to the roadmap shown in Figure 5.2 (c). This required titling angle exceeds the tilting limit of ±30°for our specimen holder.

5.1.3 Summary

In short, planar defects in boron carbide nanowires are likely "hidden" during TEM examination. There are only three specified "in-zone" directions, along which planar defects can be easily seen. The discussed difficulty of identifying "hidden" planar defects in boron carbide nanowires calls for attention to researchers to pay great cautions when analyzing microstructures of 1Dnanomaterials with a complicated rhombohedral crystal structure. Although planar defects in boron carbide 1D nanostructures were neglected or misinterpreted in some previous publications,[171-174] some research groups have realized this issue just like us. For instance, the two recent papers on α-rhombohedral boron-based nanostructures[175] and five-fold boron carbide nanowires[176] set good examples, in which abnormal weak diffraction spots were specifically studied and a serial tilting electron diffraction method was conducted to reveal cyclic and parallel twinning inside individual nanostructures. Different from these two works, our work focuses on planar defect-free-like nanowires whose experimental results are more deceptive (*i.e.*, showing no clue of defects from either TEM images or electron diffraction patterns), and presents out correct approaches to investigate these nanowires.

5.2 Identification of Fault Orientations from the "Off-Zone" Results

Based on the aforementioned results, we believe that planar defects exist in all of our as-synthesized boron carbide nanowires. During TEM examination, planar defects are invisible in some nanowires even after a full range of tilting examination. Additional manipulation to reposition these nanowires on TEM grids can help to meet the "in-zone" condition and eventually reveal the planar defects and their fault orientations (*i.e.*, AF or TF). However, this process is challenging and tedious, especially if multiple times of

nanowire manipulation are needed. So without the reposition-reexamination process, is it possible to identify the fault orientation from results obtained from the "off-zone" directions? With the help of CrystalMaker® and SingleCrystal™, a new approach has been developed to achieve this.

5.2.1 Simulated Cases along the Three "Off-Zone" Directions

The approach is based on the facts that (1) TF and AF nanowires have different preferred growth directions, and (2) the preferred growth direction of each type of nanowires is unique. Figure 5.4 (a) is a simulated TF nanowire whose preferred growth direction is perpendicular to (001) planes. This direction can be derived geometrically as $[\overline{0.292}, \overline{0.292}, 1]$. Figure 5.4 (b) is a simulated AF nanowire whose preferred growth direction is parallel to (001) planes and can be experimentally determined as the [100] direction, as discussed in section 4.3. To identify the fault orientation of a nanowire under the "off-zone" condition, simulation was done on a unit cell with the growth directions labeled on it (Figure 5.4 (c)). The unit cell was tilted to the three "off-zone" directions, generating corresponding simulated cells and diffraction patterns. At each specific "off-zone" direction, for each type of nanowires, the geometrical relation between the (projected) preferred growth direction of the nanowire and diffraction spots in diffraction patterns is unique. This relation can then be used to identify the fault orientation within a nanowire whose experimental TEM data is only from the "off-zone" directions.

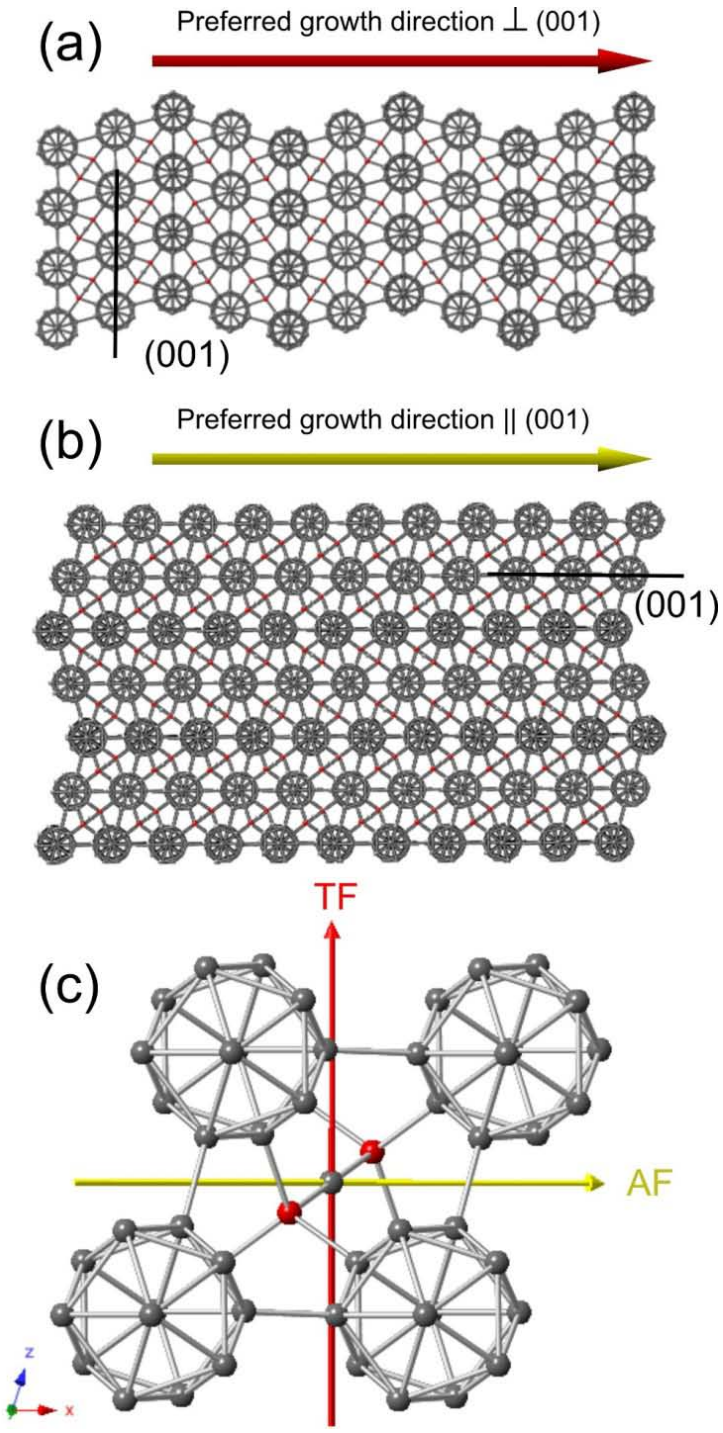

Figure 5.4 (a) A simulated TF nanowire whose preferred growth direction is perpendicular to (001) planes and can be indexed as$[\overline{0.292}, \overline{0.292}, 1]$. (b) A simulated AF nanowire whose preferred growth direction is parallel to (001) planes and can be designated as [100]. (c) A rhombohedral boron carbide lattice viewing along the [010] direction. The aforementioned preferred growth directions are labeled on it. The red line represents the preferred growth direction of a TF nanowire, whereas the yellow line represents that of an AF nanowire.

Simulated unit cells and their corresponding diffraction patterns along the three "off-zone" directions are presented in Figure 5.5. The red and yellow lines indicate the (projected) preferred growth directions for TF and AF nanowires, respectively. Figure 5.5 (a) is the simulated results from the "off-zone" [001] direction. It can be seen that the projected TF nanowire goes through $\bar{1}\bar{1}0$ and 110 spots, while the projected AF nanowire is perpendicular to the line tying the $0\bar{1}0$ and 010 spots in the diffraction pattern. These results are named as "TF case 1" and "AF case 1". Similarly, simulation results were obtained from the "off-zone" $[10\bar{1}]$ (Figure 5.5 (b)) and $[01\bar{1}]$ (Figure 5.5 (c)) directions, respectively. All results are further categorized into five cases, as summarized in Table 5.1.

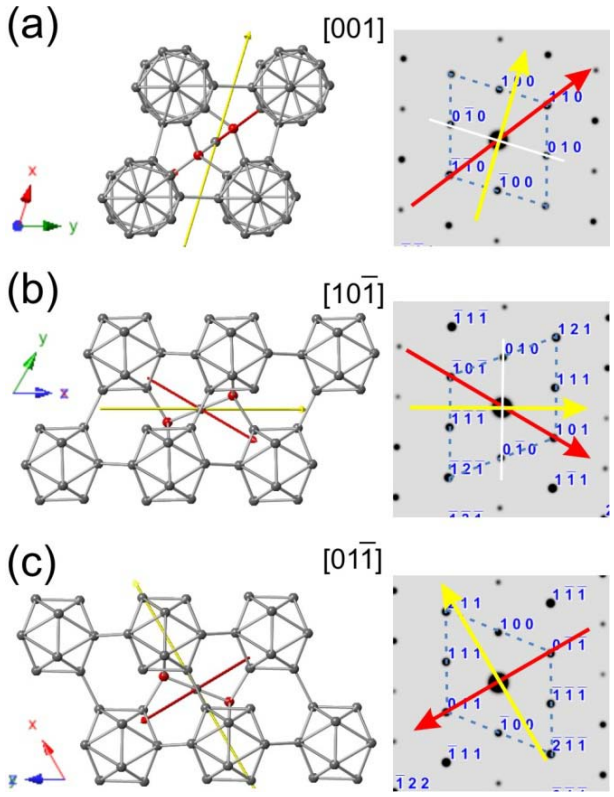

Figure 5.5 Simulated unit cells and corresponding diffraction patterns when viewing along the three "off-zone" directions: (a) [001], (b) $[10\bar{1}]$ and (c) $[01\bar{1}]$. The red and yellow lines represent the (projected) preferred growth directions of TF and AF nanowires, respectively.

Table 5.1 Simulated results for determination of the fault orientation within a nanowire whose TEM results are from the "off-zone" directions

Case No.	Zone Axis	Alignment of the Projected Preferred Growth Direction in the Diffraction Pattern
TF case 1	[001]	Through $\bar{1}\bar{1}0$ and 110 spots
TF case 2	$[10\bar{1}]$	Through $\bar{1}0\bar{1}$ and 101 spots
	$[01\bar{1}]$	Through $0\bar{1}\bar{1}$ and 011 spots
AF case 1	[001]	Perpendicular to the tie line between $0\bar{1}0$ and 010spots
AF case 2	$[10\bar{1}]$	Perpendicular to the tie line between 010 and $0\bar{1}0$ spots
AF case 3	$[01\bar{1}]$	Perpendicular to the tie line between 011 and $0\bar{1}\bar{1}$spots

5.2.2 Experimental Validation of the Simulated Cases

To verify that the above simulation results indeed can be used to predict the fault orientations of boron carbide nanowires, experimental TEM data from both "in-zone" and "off-zone" conditions have to be found on the same nanowire, which turns out to be extremely challenging. It is simply impossible to achieve this goal without multiple rounds of the reposition-reexamination operations on a single nanowire, during which the nanowire could be lost or broken.

For a TF nanowire, the planar defects are perpendicular to its preferred growth direction. When it is laid down on the support film of a TEM grid for examination, most of time the viewing direction is parallel to the planar defects (see Appendix II for illustration). Therefore it could be relatively easy to tilt to the "in-zone" condition to reveal the planar defects, as the typical example shown in Figures 5.1 (c) and (d). In order to see results from the "off-zone" directions of a TF nanowire, the nanowire has to be positioned extruding out of the support film of a TEM grid with a degree of ~60°, which is the angle between [001] and (001) plane, instead of laying on it. This slanting geometry is almost impossible to be realized by manipulation or tilting. Fortunately, there is a tripod-like branched structure, as shown in Figure 5.6, which provides solid evidence

for “TF case 1”. For this branched structure, the three legs grew along the three rhombic planes respectively, and all of them were confirmed to be TF nanowires (see Appendix III for experimental evidence). Figure 5.6 presents the results when the upper leg was tilted to the [001] zone axis. At this viewing direction, the left and right legs are under the “in-zone” condition (Figure 5.6 (a), (c) and (d)), while the upper leg is under the “off-zone” condition (Figure 5.6 (b)). The upper leg appears to be darker because it is pointing out of the image plane. Analyzing the TEM data, the projected preferred growth direction of this leg (label as a red line) is found to go through $\bar{1}\bar{1}0$ and 110 spots, which is consistent with our simulated “TF case 1”.

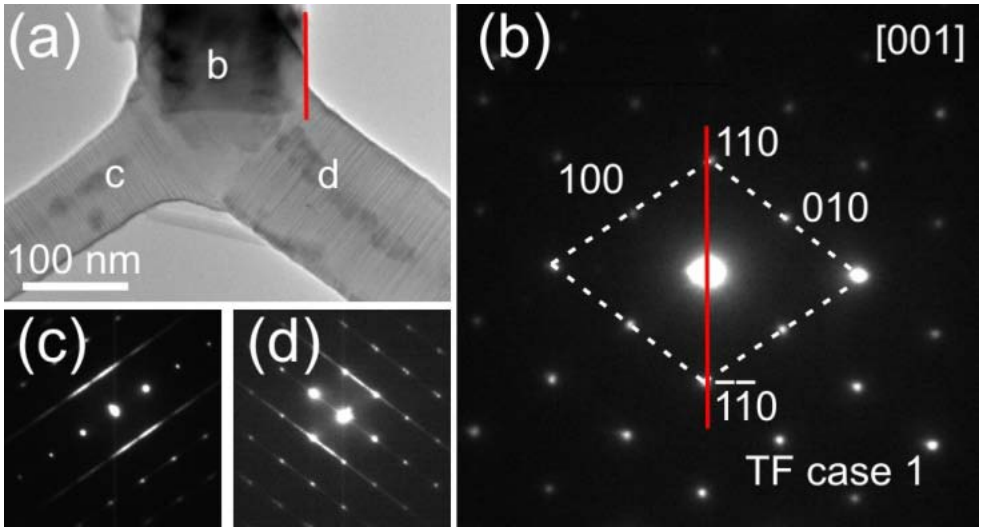

Figure 5.6 Experimental validation of the simulated “TF case 1”. (a) A boron carbide branched nanostructure made of three legs. All legs were confirmed as TF nanowires. When tilting to the [001] zone axis, (b) TEM results of the upper leg show no characteristic features of planar defects. However, the analyzed diffraction pattern agrees with our simulated “TF case 1”. TEM results of the (c) left and (d) right legs show characteristic features of TF planar defects.

For an AF nanowire, the planar defects are parallel to its preferred growth direction. When it is randomly laid down on the support film of a TEM grid for examination, most of time the viewing direction is not parallel to the planar defects (see Appendix II for illustration). In other words, results from the "off-zone" condition are commonly recorded and planar defects would be mostly invisible. With the help of the reposition-reexamination process, the correctness of all three simulated cases for AF nanowires was validated. Figure 5.7 (a)-(c) are results from the same nanowire. As shown in (a) and (b), the projected preferred growth directions labeled as yellow lines are perpendicular to the lines tying the 010 and $0\bar{1}0$ diffraction spots. These experimental results agree with the simulated "AF case 1" and "AF case 2" shown in Figure 5.5 and Table 5.1, indicating this nanowire is an AF nanowire. After reposition, the characteristic features of planar defects are clearly revealed in Figure 5.7 (c) to confirm that this nanowire is an AF one. Figure 5.7 (d) and (e) are experimental results of another nanowire, which confirm the correctness of "AF case 3".

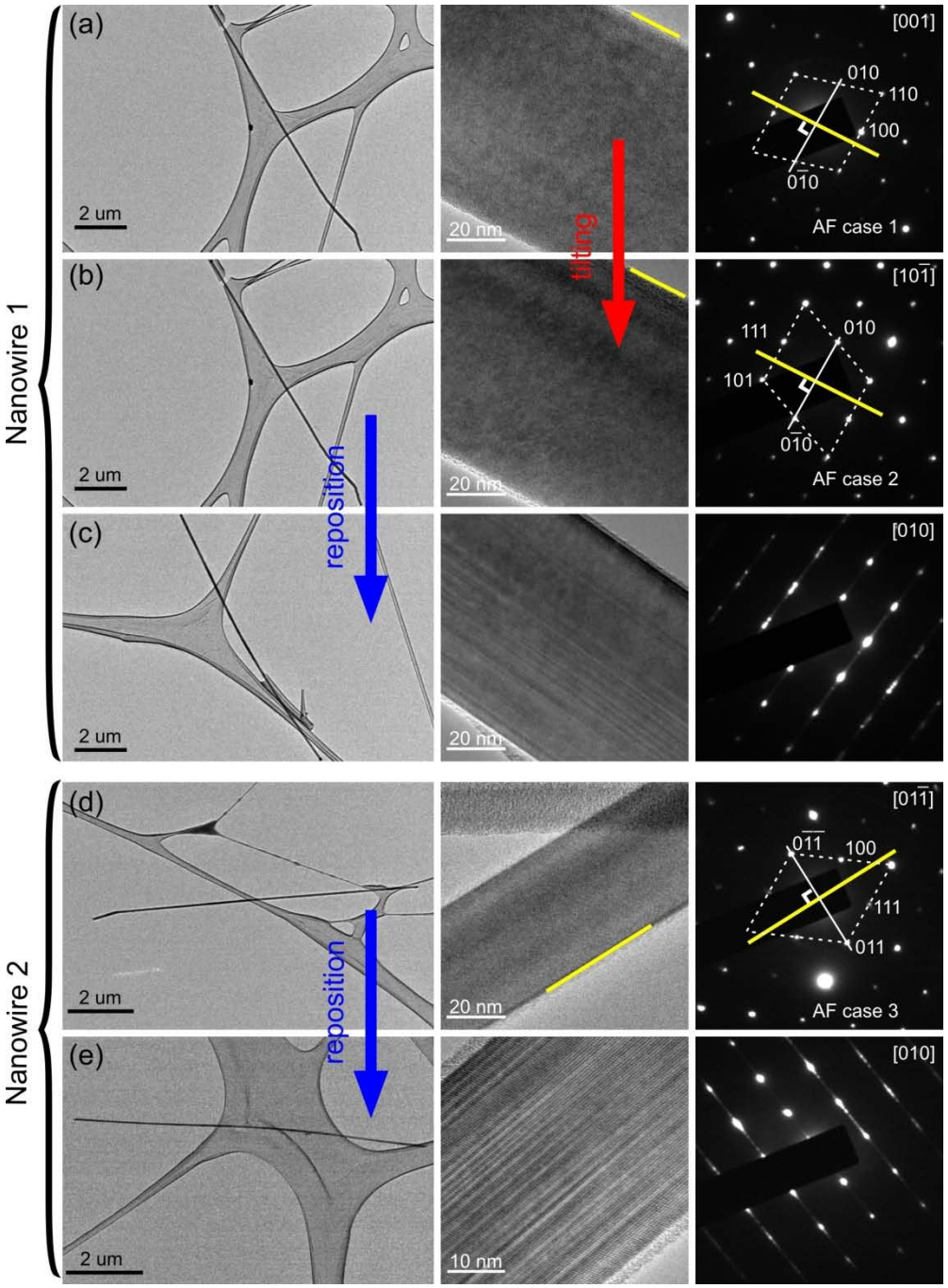

Figure 5.7 Experimental validation of the three simulated AF cases. TEM results of a nanowire whose planar defects are invisible from both (a) [001] and (b) [10$\bar{1}$] zone axes. The analyzed diffraction patterns agree with the simulated "AF case 1" and "AF case 2", indicating the nanowire is an AF one. (c) After the reposition-reexamination process, planar defects are revealed and the nanowire is confirmed to have axial faults. TEM results of another nanowire (d-e), which confirms the "AF case 3".

5.3 Summary

In summary, a thorough discussion on observation of planar defects in boron carbide nanowires is presented. There are two major findings. (1) Planar defects can easily become invisible during TEM examination, in which case observation along different zone axes is a must when studying the nature of planar defects. A roadmap based on simulated diffraction patterns along several low index zone axes parallel to planar defects is constructed to facilitate the practical TEM examination. (2) An approach has been developed to determine the fault orientation (*i.e.*, transverse faults or axial faults) within a nanowire even the planar defects are not revealed by TEM, which could facilitate further examination of the nanowire and help to establish the structure-property relations. Although our discussion is focused on boron carbide nanowires, the above two major findings are useful when studying other 1D nanostructures. This study prompt us to use cautions when drawing the conclusion of “planar defect-free” 1D nanostructures, especially for those made of materials with relatively low stacking fault energy. Last but not the least, it is worth pointing out that the current study is focused on long straight boron carbide nanowires only. For boron carbide nanowires with kinks, new phenomena might be observed in the kinked portions, which is currently under investigation.

CHAPTER 6: PRELIMINARY RESULTS ON ESTABLISHMENT OF STRUCTURE-TRANSPORT PROPERTY RELATIONSHIP

As mentioned in Chapter 1, even though both electron band structure manipulation and thermal conductivity reduction in nanomaterials have been predicted to enhance the thermoelectric figure of merit *ZT*, most experimentally observed *ZT* enhancement comes from thermal conductivity reduction due to phonon scattering at nanostructure surfaces and interfaces. For the synthesized boron carbides, which have very complex crystalline structures with multiple planar defects such as twins and stacking faults, it is of great interest to see whether their thermal conductivity is still lower than the corresponding bulk value. This critical information will help to determine whether these nanowires will possess an advantage over bulk materials for thermoelectric applications.

In order to see whether phonon-boundary scattering still plays an important role in determining the thermal conductivity of the as-synthesized boron carbide nanowires, thermal conductivity measurements of individual boron carbide nanowires with clear structural information. Each nanowire went through three steps to be fully characterized. First, nanowires were picked up from substrates by a micro-manipulator and put onto TEM grids with one nanowire in a single grid. Second, the nanowires were characterized under TEM to find out the orientation of defect. If a clear TEM image is obtainable on certain nanowire, its location is recorded for the thermal measurements and its defect density can be counted. Figure 6.1 gives an AF nanowire with a defect density of 7.95%.

The third step is to send those nanowires with clear TEM images to our collaborators in Vanderbilt University to measure the thermal conductivities. A unique measurement technique was used for the measurement.[177,178] Figure 6.1 (b) shows an SEM micrograph of an individual boron carbide nanowire bridging the two suspended membranes of a microdevice with integrated microheaters, thermometers, and electrodes for property characterization. To reduce the contact thermal resistance between the nanowire sample and the suspended membranes, electron beam-induced deposition (EBID) was used to locally deposit some gold at the two wire–membrane contacts.

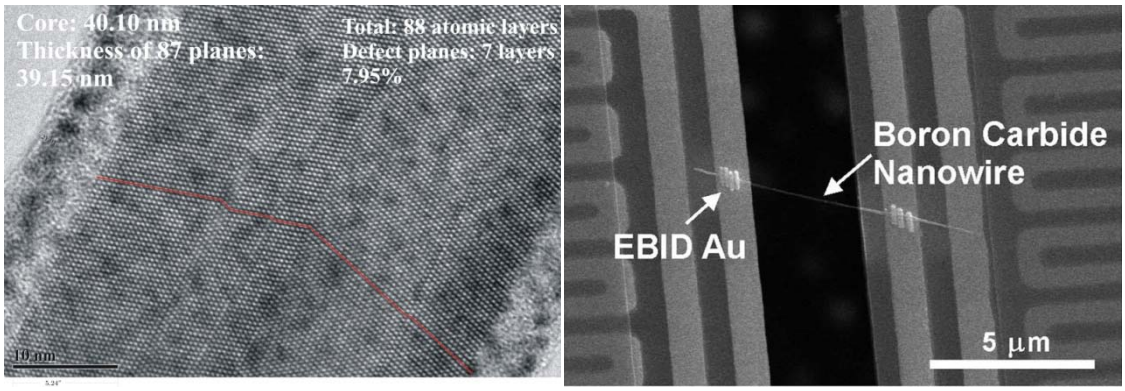

Figure 6.1 (a) An AF nanowire with a defect density of 7.95%. (b) A boron carbide nanowire of 55 nm diameter on a suspended microdevice for measurement of its thermal conductivity.

The measured thermal conductivities are displayed in Figure 6.2. At room temperature the thermal conductivities are ~3-7 W/mK, which is much lower than the value (~30 W/mK) from bulk boron carbide.[57] Moreover, it can be seen that TF nanowires have an even lower thermal conductivity, which means the defect planes normal to the phonon transport direction work better as phonon scattering sites. Another

important factor is the defect density. It can be counted only on AF nanowires because its number is infinite in TF ones. According to the three curves on the top in Figure 6.2, AF nanowire with a lower defect density (blue one) has a higher thermal conductivity. Since planar defects can further scatter the phonons, this result meets the expectation. The work is still on-going since the phonon transport can be affected by many other factors, such as diameter, carbon concentration, and doping elements. More data is needed to draw a whole picture about the dependence of thermal conductivity on nanowire's structure.

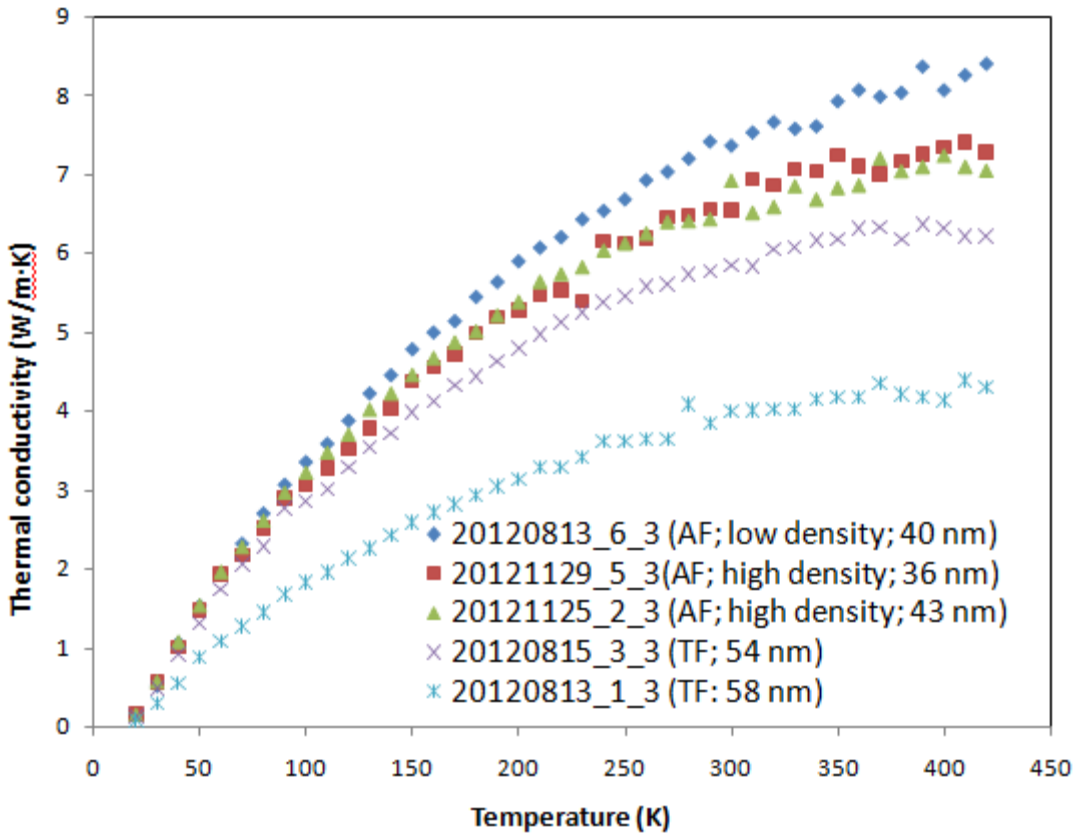

Figure 6.2 Measured thermal conductivities depending on defect orientation and density.

CHAPTER 7: CONCLUSIONS AND FUTURE WORKS

In this dissertation work, crystalline boron carbide nanowires have been synthesized by using a LPCVD system. Intrinsic planar defect can also be observed in the nanowires. Depending on the orientations of the defect plane, they are categorized as TF and AF. The growth habits for TF and AF nanowires are studied, including the growth direction and catalyst identification. To help to tell the defect orientation during TEM characterization, a method based on lattice calculation and simulation was developed and tested. The measured thermal conductivities of boron carbide nanowires are much lower than the value from its bulk counterpart. It was also found that the thermal conductivity is related to the defect orientation and density.

There are some questions to be solved in the future. The ultimate goal for this project is to be able to grow nanowire with controlled structure, so that the thermoelectric performance can be optimized. In the terms of synthesis, the cause of kinks and branches needs to be studied carefully by design of experiments. For identification of the catalysts, all the analyzed data are based on the Al-doped nanowires. Same strategy can be applied on the Si-doped ones. However, in addition to the Ni-B compound, there are also some Ni-Si compounds preferred to form below 1000 °C. That makes the procedure much more complicated. The status of the catalyst greatly depends on the temperature. Other parameters (*e.g.* flow rate, pressure, and the oxide layer) may also have some impact on the catalyst, which could lead to different nanowire structures (TF or AF). More work

needs to be done on the thermal measurements to come up with a convincing conclusion with the structure-transport property relationship studied on each structural factor (*e.g.* diameter, defect, composition, etc.).

REFERENCES

1 Annual energy review 2010. *U.S. Energy Information Administration*.

2 Global Wind Report - Annual market update 2011. *Global Wind Energy Council*.

3 Renewables 2010 - Global Status Report. *Renewable Energy Policy Network for the 21st Century*.

4 Seebeck, T. J. Magnetische Polarisation der Metalle und Erze Durch Temperatur-Differenz. *Abhandlungen der Deutschen Akademie der Wissenschafren zu Berlin*, 265 (1822-1823).

5 Peltier, J. C. Nouvelles experiences sur la caloricite des courants electriques. *Annales de chimie* **56**, 371-386 (1834).

6 Lenz, E. Ueber das Verhalten der Kupfervitriollösung in der galvanischen Kette. *Annalen der Physik* **120**, 349-356 (1838).

7 Thomson, W. On a mechanical theory of thermoelectric currents. *Proc. R. Soc. Edinb.*, 91-98 (1851).

8 Altenkirch, E. Über den Nutzeffekt der Thermosäule. *Physikalische Zeitschrift* **10**, 560-580 (1909).

9 Altenkirch, E. Elektrothermische Kälteerzeugung und reversible elektrische Heizung. *Physikalische Zeitschrift* **12**, 920-924 (1911).

10 Snyder, G. J. & Ursell, T. S. Thermoelectric efficiency and compatibility. *Physical Review Letters* **91** (2003).

11 Glen, S. in *CRC Handbook of Thermoelectrics* (CRC Press, 1995).

12 Brown, S. R., Kauzlarich, S. M., Gascoin, F. & Snyder, G. J. Yb14MnSb11: New high efficiency thermoelectric material for power generation. *Chemistry of Materials* **18**, 1873-1877 (2006).

13 Klemens, P. G. THE SCATTERING OF LOW-FREQUENCY LATTICE WAVES BY STATIC IMPERFECTIONS. *Proceedings of the Physical Society of London Section A* **68**, 1113-1128 (1955).

14 Wright, D. A. THERMOELECTRIC PROPERTIES OF BISMUTH TELLURIDE AND ITS ALLOYS. *Nature* **181**, 834-834 (1958).

15 Sales, B. C., Mandrus, D. & Williams, R. K. Filled skutterudite antimonides: A new class of thermoelectric materials. *Science* **272**, 1325-1328 (1996).

16 Savvides, N. & Goldsmid, H. J. EFFECT OF BOUNDARY SCATTERING ON HIGH-TEMPERATURE THERMAL-CONDUCTIVITY OF SILICON. *Journal of Physics C-Solid State Physics* **6**, 1701-1708 (1973).

17 David, R. & Bhandari, C. in *CRC Handbook of Thermoelectrics* (CRC Press, 1995).

18 Vining, C. B. An inconvenient truth about thermoelectrics. *Nature Materials* **8**, 83-85 (2009).

19 Majumdar, A. Thermoelectricity in semiconductor nanostructures. *Science* **303**, 777-778 (2004).

20 Snyder, G. J. & Toberer, E. S. Complex thermoelectric materials. *Nature Materials* **7**, 105-114 (2008).

21 Hicks, L. D. & Dresselhaus, M. S. Effect of quantum-well structures on the thermoelectric figure of merit. *Physical Review B* **47**, 12727-12731 (1993).

22 Hicks, L. D., Harman, T. C. & Dresselhaus, M. S. Use of quantum-well superlattices to obtain a high figure of merit from nonconventional thermoelectric materials. *Applied Physics Letters* **63**, 3230-3232 (1993).

23 Cutler, M. & Mott, N. F. OBSERVATION OF ANDERSON LOCALIZATION IN AN ELECTRON GAS. *Physical Review* **181**, 1336-& (1969).

24 Chen, G., Dresselhaus, M. S., Dresselhaus, G., Fleurial, J. P. & Caillat, T. Recent Developments in Thermoelectric Materials. *Int. Mater. Rev.* **48**, 45-66 (2003).

25 Shakouri, A. in *Annual Review of Materials Research, Vol 41* Vol. 41 *Annual Review of Materials Research* (eds D. R. Clarke & P. Fratzl) 399-431 (2011).

26 Hicks, L. D., Harman, T. C., Sun, X. & Dresselhaus, M. S. Experimental study of the effect of quantum-well structures on the thermoelectric figure of merit. *Physical Review B* **53**, R10493-R10496 (1996).

27 Venkatasubramanian, R., Siivola, E., Colpitts, T. & O'Quinn, B. Thin-film thermoelectric devices with high room-temperature figures of merit. *Nature* **413**, 597-602 (2001).

28 Venkatasubramanian, R., Colpitts, T., Watko, E., Lamvik, M. & ElMasry, N. MOCVD of Bi2Te3, Sb2Te3 and their superlattice structures for thin-film thermoelectric applications. *Journal of Crystal Growth* **170**, 817-821 (1997).

29 Beyer, H. *et al.* PbTe based superlattice structures with high thermoelectric efficiency. *Applied Physics Letters* **80**, 1216-1218 (2002).

30 Broido, D. A. & Reinecke, T. L. Theory of thermoelectric power factor in quantum well and quantum wire superlattices. *Physical Review B* **64** (2001).

31 Koga, T., Cronin, S. B., Dresselhaus, M. S., Liu, J. L. & Wang, K. L. Experimental proof-of-principle investigation of enhanced Z(3D)T in (001) oriented Si/Ge superlattices. *Applied Physics Letters* **77**, 1490-1492 (2000).

32 Chen, G., Neagu, M. & BorcaTasciuc, T. in *Thermoelectric Materials - New Directions and Approaches* Vol. 478 *Materials Research Society Symposium Proceedings* (eds T. M. Tritt, M. G. Kanatzidis, H. B. Lyon, & G. D. Maham) 85-90 (1997).

33 Yang, B., Liu, W. L., Liu, J. L., Wang, K. L. & Chen, G. Measurements of anisotropic thermoelectric properties in superlattices. *Applied Physics Letters* **81**, 3588-3590 (2002).

34 Capinski, W. S. & Maris, H. J. Thermal conductivity of GaAs/AlAs superlattices. *Physica B-Condensed Matter* **219-20**, 699-701 (1996).

35 Lee, S. M., Cahill, D. G. & Venkatasubramanian, R. Thermal conductivity of Si-Ge superlattices. *Applied Physics Letters* **70**, 2957-2959 (1997).

36 Broido, D. A. & Reinecke, T. L. EFFECT OF SUPERLATTICE STRUCTURE ON THE THERMOELECTRIC FIGURE OF MERIT. *Physical Review B* **51**, 13797-13800 (1995).

37 Hicks, L. D. & Dresselhaus, M. S. THERMOELECTRIC FIGURE OF MERIT OF A ONE-DIMENSIONAL CONDUCTOR. *Physical Review B* **47**, 16631-16634 (1993).

38 Boukai, A. I. *et al.* Silicon nanowires as efficient thermoelectric materials. *Nature* **451**, 168-171 (2008).

39 Hochbaum, A. I. *et al.* Enhanced thermoelectric performance of rough silicon nanowires. *Nature* **451**, 163-U165 (2008).

40 Wu, Y. Y., Fan, R. & Yang, P. D. Block-by-block growth of single-crystalline Si/SiGe superlattice nanowires. *Nano Letters* **2**, 83-86 (2002).

41 Gudiksen, M. S., Lauhon, L. J., Wang, J., Smith, D. C. & Lieber, C. M. Growth of nanowire superlattice structures for nanoscale photonics and electronics. *Nature* **415**, 617-620 (2002).

42 Hu, M. & Poulikakos, D. Si/Ge Superlattice Nanowires with Ultralow Thermal Conductivity. *Nano Letters* **12**, 5487-5494 (2012).

43 Dames, C. & Chen, G. Theoretical phonon thermal conductivity of Si/Ge superlattice nanowires. *Journal of Applied Physics* **95**, 682-693 (2004).

44 Harman, T. C., Walsh, M. P., Laforge, B. E. & Turner, G. W. Nanostructured thermoelectric materials. *Journal of Electronic Materials* **34**, L19-L22 (2005).

45 Hsu, K. F. *et al.* Cubic AgPbmSbTe2+m: Bulk thermoelectric materials with high figure of merit. *Science* **303**, 818-821 (2004).

46 Wood, C. Boron carbides as high temperature thermoelectric materials. *AIP Conference Proceedings* **140**, 362-372 (1986).

47 Bouchacourt, M. & Thevenot, F. THE CORRELATION BETWEEN THE THERMOELECTRIC PROPERTIES AND STOICHIOMETRY IN THE BORON-CARBIDE PHASE B4C-B10.5C. *Journal of Materials Science* **20**, 1237-1247 (1985).

48 Aselage, T. L. High Temperature Thermoelectric Properties of Boron Carbide. *MRS Online Proceedings Library* **234**, null-null (1991).

49 Werheit, H. in *Thermoelectrics, 2006. ICT '06. 25th International Conference on.* 159-163.

50 Emin, D. Unusual properties of icosahedral boron-rich solids. *Journal of Solid State Chemistry* **179**, 2791-2798 (2006).

51 Bouchacourt, M. & Thevenot, F. MELTING OF BORON-CARBIDE AND THE HOMOGENEITY RANGE OF THE BORON-CARBIDE PHASE. *Journal of the Less-Common Metals* **67**, 327-331 (1979).

52 Suri, A. K., Subramanian, C., Sonber, J. K. & Murthy, T. S. R. C. Synthesis and consolidation of boron carbide: a review. *International Materials Reviews* **55**, 4-40 (2010).

53 Tallant, D. R., Aselage, T. L., Campbell, A. N. & Emin, D. BORON-CARBIDE STRUCTURE BY RAMAN-SPECTROSCOPY. *Physical Review B* **40**, 5649-5656 (1989).

54 Kwei, G. H. & Morosin, B. Structures of the boron-rich boron carbides from neutron powder diffraction: Implications for the nature of the inter-icosahedral chains. *Journal of Physical Chemistry* **100**, 8031-8039 (1996).

55 Aselage, T. L., Emin, D. & McCready, S. S. Conductivities and Seebeck coefficients of boron carbides: Softening bipolaron hopping. *Physical Review B* **64** (2001).

56 Aselage, T. L., Emin, D., McCready, S. S. & Duncan, R. V. Large enhancement of boron carbides' seebeck coefficients through vibrational softening. *Physical Review Letters* **81**, 2316-2319 (1998).

57 Gunjishima, I., Akashi, T. & Goto, T. Thermoelectric properties of single crystalline B4C prepared by a floating zone method. *Materials Transactions* **42**, 1445-1450 (2001).

58 Schmechel, R. & Werheit, H. Correlation between structural defects and electronic properties of icosahedral boron-rich solids. *Journal of Physics-Condensed Matter* **11**, 6803-6813 (1999).

59 Werheit, H. Are there bipolarons in icosahedral boron-rich solids? *Journal of Physics-Condensed Matter* **19** (2007).

60 Werheit, H. Present knowledge of electronic properties and charge transport of icosahedral boron-rich solids. *Journal of Physics: Conference Series* **176**, 012019 (2009).

61 Wood, C. & Emin, D. CONDUCTION MECHANISM IN BORON-CARBIDE. *Physical Review B* **29**, 4582-4587 (1984).

62 Wood, C., Emin, D. & Gray, P. E. THERMAL-CONDUCTIVITY OF BORON CARBIDES. *Physical Review B* **31**, 6811-6814 (1985).

63 Ashbee, K. H. G. DEFECTS IN BORON CARBIDE BEFORE AND AFTER NEUTRON IRRADIATION. *Acta Metallurgica* **19**, 1079-& (1971).

64 Ashbee, K. H. G. & Dubose, C. K. H. Dislocation nodes in boron carbide, with special reference to non-stoichiometry. *Acta Metallurgica* **20**, 241-245 (1972).

65 Jostsons, A., Dubose, C. K. H., Copeland, G. L. & Stiegler, J. O. DEFECT STRUCTURE OF NEUTRON-IRRADIATED BORON-CARBIDE. *J. Nucl. Mater.* **49**, 136-150 (1973).

66 Yakel, H. The crystal structure of a boron-rich boron carbide. *Acta Crystallographica Section B* **31**, 1797-1806 (1975).

67 Bandyopadhyay, A. K., Beuneu, F., Zuppiroli, L. & Beauvy, M. THE ROLE OF FREE CARBON IN THE TRANSPORT AND MAGNETIC-PROPERTIES OF BORON-CARBIDE. *Journal of Physics and Chemistry of Solids* **45**, 207-214 (1984).

68 Mackinnon, I. D. R., Aselage, T. & Van Deusen, S. B. High resolution imaging of boron carbide microstructures. *AIP Conference Proceedings* **140**, 114-120 (1986).

69 Miller, M. L. & Mackinnon, I. D. R. A Comparison of Calculated and Experimental Hrtem Images for Twinned Boron Carbide. *MRS Online Proceedings Library* **97**, null-null (1987).

70 Anselmi-Tamburini, U., Ohyanagi, M. & Munir, Z. A. Modeling studies of the effect of twins on the X-ray diffraction patterns of boron carbide. *Chemistry of Materials* **16**, 4347-4351 (2004).

71 Heian, E. M. *et al.* Synthesis of dense, high-defect-concentration B4C through mechanical activation and field-assisted combustion. *Journal of the American Ceramic Society* **87**, 779-783 (2004).

72 Anselmi-Tamburini, U., Munir, Z. A., Kodera, Y., Imai, T. & Ohyanagi, M. Influence of synthesis temperature on the defect structure of boron carbide: Experimental and modeling studies. *Journal of the American Ceramic Society* **88**, 1382-1387 (2005).

73 Chang, B., Gersten, B. L., Szewczyk, S. T. & Adams, J. W. Characterization of boron carbide nanoparticles prepared by a solid state thermal reaction. *Applied Physics a-Materials Science & Processing* **86**, 83-87 (2007).

74 Li, Y. *et al.* Deformation twinning in boron carbide particles within nanostructured Al 5083/B4C metal matrix composites. *Philosophical Magazine* **90**, 783-792 (2010).

75 Zhang, S., Lu, W., Wang, C., Shen, Q. & Zhang, L. Synthesis and characterization of B13C2 boron carbide ceramic by pulsed electric current sintering. *Ceramics International* **38**, 895-900 (2012).

76 Zhang, S., Lu, W., Wang, C., Shen, Q. & Zhang, L. Investigation of planar defects in pulsed electric current sintered B13C2 boron carbide ceramic. *Ceramics International* **38**, 817-819 (2012).

77 Ma, R. Z. & Bando, Y. High purity single crystalline boron carbide nanowires. *Chemical Physics Letters* **364**, 314-317 (2002).

78 Carlsson, M., Garcia-Garcia, F. J. & Johnsson, M. Synthesis and characterisation of boron carbide whiskers and thin elongated platelets. *Journal of Crystal Growth* **236**, 466-476 (2002).

79 Zhang, D., McIlroy, D. N., Geng, Y. & Norton, M. G. Growth and characterization of boron carbide nanowires. *Journal of Materials Science Letters* **18**, 349-351 (1999).

80 Bao, L.-H. *et al.* Synthesis and photoluminescence property of boron carbide nanowires. *Chinese Physics B* **17**, 4585-4591 (2008).

81 Fu, X., Jiang, J., Liu, C. & Yuan, J. Fivefold twinned boron carbide nanowires. *Nanotechnology* **20**, 365707-365707 (2009).

82 Han, W. Q. Silicon doped boron carbide nanorod growth via a solid-liquid-solid process. *Applied Physics Letters* **88** (2006).

83 Velamakanni, A., Ganesh, K. J., Zhu, Y., Ferreira, P. J. & Ruoff, R. S. Catalyst-Free Synthesis and Characterization of Metastable Boron Carbide Nanowires. *Advanced Functional Materials* **19**, 3926-3933 (2009).

84 Tao, X. *et al.* B4C-Nanowires/Carbon-Microfiber Hybrid Structures and Composites from Cotton T-shirts. *Advanced Materials* **22**, 2055-+ (2010).

85 Ma, R. & Bando, Y. Investigation on the growth of boron carbide nanowires. *Chemistry of Materials* **14**, 4403-4407 (2002).

86 Huang, Y. *et al.* Fabrication of patterned boron carbide nanowires and their electrical, field emission, and flexibility properties. *Nano Research* **5**, 896-902 (2012).

87 Tian, J.-F. *et al.* Probing field emission from boron carbide nanowires. *Chinese Physics Letters* **25**, 3463-3466 (2008).

88 Fu, X. *et al.* Re-entrant-Groove-Assisted VLS Growth of Boron Carbide Five-Fold Twinned Nanowires. *Chinese Physics Letters* **26** (2009).

89 Song, D. Effects of rf power on surface-morphological, structural and electrical properties of aluminium-doped zinc oxide films by magnetron sputtering. *Applied Surface Science* **254**, 4171-4178 (2008).

90 Swann, S. MAGNETRON SPUTTERING. *Physics in Technology* **19**, 67-75 (1988).

91 Cullity, B. D. *Elements of X-ray diffraction*. (Addison-Wesley Pub. Co., 1956).

92 Williams, D. B. C. C. B. *Transmission electron microscopy : a textbook for materials science*. (Springer, 2009).

93 Brandon, D. G. & Kaplan, W. D. *Microstructural characterization of materials*. (John Wiley, 2008).

94 Goodhew, P. J. H. F. J. *Electron microscopy and analysis*. (Taylor & Francis, 1988).

95 Wagner, R. S. & Ellis, W. C. VAPOR-LIQUID-SOLID MECHANISM OF SINGLE CRYSTAL GROWTH. *Applied Physics Letters* **4**, 89-90 (1964).

96 Suri, A. K., Subramanian, C., Sonber, J. K. & Murthy, T. Synthesis and consolidation of boron carbide: a review. *Int. Mater. Rev.* **55**, 4-40 (2010).

97 Xu, T. T., Nicholls, A. W. & Ruoff, R. S. Boron nanowires and novel Tube-catalytic particle-wire hybrid boron nanostructures. *Nano* **1**, 55-63 (2006).

98 Matkovich, V. I. *Boron and Refractory Borides*. (Springer-Verlag, 1977).

99 Ashbee, K. H. G. DEFECTS IN BORON CARBIDE BEFORE AND AFTER NEUTRON IRRADIATION. *Acta Metall.* **19**, 1079-& (1971).

100 Kuzenkova, M. A., Kislyi, P. S., Grabchuk, B. L. & Bodnaruk, N. I. Structure and Properties of Sintered Boron Carbide. *J. Less Common Met.* **67**, 217-223 (1979).

101 Mackinnon, I. D. R., Aselage, T. & Ban Deusen, S. B. in *AIP Conf. Proc.* (eds D. Emin *et al.*) 114 (Amerian Institute of Physics).

102 Miller, M. L. & Mackinnon, I. D. R. in *Mater. Res. Soc. Symp. Proc.* 133.

103 Li, Y. *et al.* Deformation twinning in boron carbide particles within nanostructured Al 5083/B4C metal matrix composites. *Philos. Mag.* **90**, 783-792 (2010).

104 Carlsson, M., Garcia-Garcia, F. J. & Johnsson, M. Synthesis and characterisation of boron carbide whiskers and thin elongated platelets. *J. Cryst. Growth* **236**, 466-476 (2002).

105 Gatti, A., Mancuso, C., Feingold, E. & Mehan, R. L. in *Proceedings of an International Conference on Crystal Growth.* 317-323 (Pergamon, Oxford).

106 Mackinnon, I. D. R. & Smith, K. L. in *Mater. Res. Soc. Symp. Proc.* 127-132.

107 Ma, R. & Bando, Y. Investigation on the growth of boron carbide nanowires. *Chem. Mater.* **14**, 4403-4407 (2002).

108 Zhu, M. *et al.* Si enhances the growth of B4C nanowires. *J. Cryst. Growth* **311**, 3721-3725 (2009).

109 Xu, F. & Bando, Y. Formation of Two-Dimensional Nanomaterials of Boron Carbides. *J. Phys. Chem. B* **108**, 7651-7655 (2004).

110 Jiang, J., Cao, M. H., Sun, Y. K., Wu, P. W. & Yuan, J. Star-Shaped Cyclic-Twinning Nanowires. *Appl. Phys. Lett.* **88**, 163107 (2006).

111 Wagner, R. S. & Ellis, W. C. VAPOR-LIQUID-SOLID MECHANISM OF CRYSTAL GROWTH AND ITS APPLICATION TO SILICON. *Transactions of the Metallurgical Society of Aime* **233**, 1053-& (1965).

112 Borel, J. P. THERMODYNAMICAL SIZE EFFECT AND THE STRUCTURE OF METALLIC CLUSTERS. *Surface Science* **106**, 1-9 (1981).

113 Wang, N., Cai, Y. & Zhang, R. Q. Growth of nanowires. *Materials Science & Engineering R-Reports* **60**, 1-51 (2008).

114 Pan, Z. W., Dai, Z. R. & Wang, Z. L. Nanobelts of semiconducting oxides. *Science* **291**, 1947-1949 (2001).

115 Dai, Z. R., Pan, Z. W. & Wang, Z. L. Novel nanostructures of functional oxides synthesized by thermal evaporation. *Advanced Functional Materials* **13**, 9-24 (2003).

116 Xia, Y. N. *et al.* One-dimensional nanostructures: Synthesis, characterization, and applications. *Advanced Materials* **15**, 353-389 (2003).

117 Yao, B. D., Chan, Y. F. & Wang, N. Formation of ZnO nanostructures by a simple way of thermal evaporation. *Applied Physics Letters* **81**, 757-759 (2002).

118 Wang, Z. L., Kong, X. Y. & Zuo, J. M. Induced growth of asymmetric nanocantilever arrays on polar surfaces. *Physical Review Letters* **91** (2003).

119 Holmes, J. D., Johnston, K. P., Doty, R. C. & Korgel, B. A. Control of thickness and orientation of solution-grown silicon nanowires. *Science* **287**, 1471-1473 (2000).

120 Tuan, H. Y., Lee, D. C., Hanrath, T. & Korgel, B. A. Catalytic solid-phase seeding of silicon nanowires by nickel nanocrystals in organic solvents. *Nano Letters* **5**, 681-684 (2005).

121 Schonenberger, C. *et al.* Template synthesis of nanowires in porous polycarbonate membranes: Electrochemistry and morphology. *Journal of Physical Chemistry B* **101**, 5497-5505 (1997).

122 Gates, B., Mayers, B., Cattle, B. & Xia, Y. N. Synthesis and characterization of uniform nanowires of trigonal selenium. *Advanced Functional Materials* **12**, 219-227 (2002).

123 Wu, Y. Y. & Yang, P. D. Direct observation of vapor-liquid-solid nanowire growth. *Journal of the American Chemical Society* **123**, 3165-3166 (2001).

124 Kodambaka, S., Tersoff, J., Reuter, M. C. & Ross, F. M. Diameter-independent kinetics in the vapor-liquid-solid growth of Si nanowires. *Physical Review Letters* **96** (2006).

125 Wen, C. Y. *et al.* Formation of Compositionally Abrupt Axial Heterojunctions in Silicon-Germanium Nanowires. *Science* **326**, 1247-1250 (2009).

126 Oh, S. H. *et al.* Oscillatory Mass Transport in Vapor-Liquid-Solid Growth of Sapphire Nanowires. *Science* **330**, 489-493 (2010).

127 Petkov, N. In Situ Real-Time TEM Reveals Growth, Transformation and Function in One-Dimensional Nanoscale Materials: From a Nanotechnology Perspective. *ISRN Nanotechnology* **2013**, 21 (2013).

128 Kodambaka, S., Tersoff, J., Reuter, M. C. & Ross, F. M. Germanium nanowire growth below the eutectic temperature. *Science* **316**, 729-732 (2007).

129 Sutter, E. & Sutter, P. Phase diagram of nanoscale alloy particles used for vapor-liquid-solid growth of semiconductor nanowires. *Nano Letters* **8**, 411-414 (2008).

130 Ross, F. M. Controlling nanowire structures through real time growth studies. *Reports on Progress in Physics* **73** (2010).

131 Fortuna, S. A. & Li, X. Metal-catalyzed semiconductor nanowires: a review on the control of growth directions. *Semiconductor Science and Technology* **25** (2010).

132 Cui, Y., Lauhon, L. J., Gudiksen, M. S., Wang, J. F. & Lieber, C. M. Diameter-controlled synthesis of single-crystal silicon nanowires. *Applied Physics Letters* **78**, 2214-2216 (2001).

133 Chan, Y. F. *et al.* ZnSe nanowires epitaxially grown on GaP(111) substrates by molecular-beam epitaxy. *Applied Physics Letters* **83**, 2665-2667 (2003).

134 Wu, Y. *et al.* Controlled growth and structures of molecular-scale silicon nanowires. *Nano Letters* **4**, 433-436 (2004).

135 Schmidt, V., Senz, S. & Gosele, U. Diameter-dependent growth direction of epitaxial silicon nanowires. *Nano Letters* **5**, 931-935 (2005).

136 Cai, Y. *et al.* The size-dependent growth direction of ZnSe nanowires. *Advanced Materials* **18**, 109-114 (2006).

137 Cai, Y. *et al.* Temperature-dependent growth direction of ultrathin ZnSe nanowires. *Small* **3**, 111-115 (2007).

138 Shan, C. X., Liu, Z. & Hark, S. K. CdSe nanowires with controllable growth orientations. *Applied Physics Letters* **90** (2007).

139 Lugstein, A. *et al.* Pressure-induced orientation control of the growth of epitaxial silicon nanowires. *Nano Letters* **8**, 2310-2314 (2008).

140 Hyun, Y.-J., Lugstein, A., Steinmair, M., Bertagnolli, E. & Pongratz, P. Orientation specific synthesis of kinked silicon nanowires grown by the vapour-liquid-solid mechanism. *Nanotechnology* **20** (2009).

141 Westwater, J., Gosain, D. P., Tomiya, S., Usui, S. & Ruda, H. Growth of silicon nanowires via gold/silane vapor-liquid-solid reaction. *Journal of Vacuum Science & Technology B* **15**, 554-557 (1997).

142 Jagannathan, H. *et al.* Nature of germanium nanowire heteroepitaxy on silicon substrates. *Journal of Applied Physics* **100** (2006).

143 Schmid, H. *et al.* Patterned epitaxial vapor-liquid-solid growth of silicon nanowires on Si(111) using silane. *Journal of Applied Physics* **103** (2008).

144 Ding, Y. & Wang, Z. L. Structure analysis of nanowires and nanobelts by transmission electron microscopy. *Journal of Physical Chemistry B* **108**, 12280-12291 (2004).

145 Hannon, J. B., Kodambaka, S., Ross, F. M. & Tromp, R. M. The influence of the surface migration of gold on the growth of silicon nanowires. *Nature* **440**, 69-71 (2006).

146 Kodambaka, S., Hannon, J. B., Tromp, R. M. & Ross, F. M. Control of Si nanowire growth by oxygen. *Nano Letters* **6**, 1292-1296 (2006).

147 Kawashima, T. *et al.* Control of surface migration of gold particles on Si nanowires. *Nano Letters* **8**, 362-368 (2008).

148 Wagner, R. S. & Doherty, C. J. MECHANISM OF BRANCHING AND KINKING DURING VLS CRYSTAL GROWTH. *Journal of the Electrochemical Society* **115**, 93-& (1968).

149 Lee, G. *et al.* Directionally Integrated VLS Nanowire Growth in a Local Temperature Gradient. *Angewandte Chemie-International Edition* **48**, 7366-7370 (2009).

150 Madras, P., Dailey, E. & Drucker, J. Kinetically Induced Kinking of Vapor-Liquid-Solid Grown Epitaxial Si Nanowires. *Nano Letters* **9**, 3826-3830 (2009).

151 Shen, G., Liang, B., Wang, X., Chen, P.-C. & Zhou, C. Indium Oxide Nanospirals Made of Kinked Nanowires. *Acs Nano* **5**, 2155-2161 (2011).

152 Tian, B., Xie, P., Kempa, T. J., Bell, D. C. & Lieber, C. M. Single-crystalline kinked semiconductor nanowire superstructures. *Nature Nanotechnology* **4**, 824-829 (2009).

153 Kim, J. H. *et al.* Taper-free and kinked germanium nanowires grown on silicon via purging and the two-temperature process. *Nanotechnology* **23** (2012).

154 Schwarz, K. W. & Tersoff, J. Elementary Processes in Nanowire Growth. *Nano Letters* **11**, 316-320 (2011).

155 Wu, B. *et al.* Microstructure-Hardened Silver Nanowires. *Nano Letters* **6**, 468-472 (2006).

156 Dick, K. A., Thelander, C., Samuelson, L. & Caroff, P. Crystal Phase Engineering in Single InAs Nanowires. *Nano Letters* **10**, 3494-3499 (2010).

157 Guthy, C., Nam, C. Y. & Fischer, J. E. Unusually Low Thermal Conductivity of Gallium Nitride Nanowires. *Journal of Applied Physics* **103**, 064319 (2008).

158 Bao, J. M. *et al.* Optical Properties of Rotationally Twinned InP Nanowire Heterostructures. *Nano Letters* **8**, 836-841 (2008).

159 Cayron, C. *et al.* Odd Electron Diffraction Patterns in Silicon Nanowires and Silicon Thin Films Explained by Microtwins and Nanotwins. *Journal of Applied Crystallography* **42**, 242-252 (2009).

160 Lopez, F. J., Hemesath, E. R. & Lauhon, L. J. Ordered Stacking Fault Arrays in Silicon Nanowires. *Nano Letters* **9**, 2774-2779 (2009).

161 den Hertog, M. I. *et al.* Hidden Defects in Silicon Nanowires. *Nanotechnology* **23**, 025701 (2012).

162 Hemesath, E. R., Schreiber, D. K., Kisielowski, C. F., Petford-Long, A. K. & Lauhon, L. J. Atomic Structural Analysis of Nanowire Defects and Polytypes Enabled Through Cross-Sectional Lattice Imaging. *Small* **8**, 1717-1724 (2012).

163 Davidson, F. M., Lee, D. C., III, Fanfair, D. D. & Korgel, B. A. Lamellar Twinning in Semiconductor Nanowires. *Journal of Physical Chemistry C* **111**, 2929-2935 (2007).

164 Algra, R. E. *et al.* Twinning Superlattices in Indium Phosphide Nanowires. *Nature* **456**, 369-372 (2008).

165 Wang, D. H. *et al.* Periodically Twinned SiC Nanowires. *Nanotechnology* **19**, 215602 (2008).

166 Caroff, P. *et al.* Controlled Polytypic and Twin-Plane Superlattices in III-V Nanowires. *Nature Nanotechnology* **4**, 50-55 (2009).

167 Ding, Y. & Wang, Z. L. Structures of Planar Defects in ZnO Nanobelts and Nanowires. *Micron* **40**, 335-342 (2009).

168 Bottner, H., Chen, G. & Venkatasubramanian, R. Aspects of Thin-Film Superlattice Thermoelectric Materials, Devices, and Applications. *Mrs Bulletin* **31**, 211-217 (2006).

169 Guan, Z. *et al.* Boron carbide nanowires: low temperature synthesis and structural and thermal conductivity characterization. *J. Mater. Chem.* **22**, 9853-9860 (2012).

170 Matkovich, V. I. (Springer-Verlag, Berlin, 1977).

171 Han, W. Q. Silicon doped boron carbide nanorod growth via a solid-liquid-solid process. *Appl. Phys. Lett.* **88** (2006).

172 Tian, J. F. *et al.* Boron carbide and silicon oxide hetero-nanonecklaces via temperature modulation. *Crystal Growth & Design* **8**, 3160-3164 (2008).

173 Bao, L. H. *et al.* Synthesis and photoluminescence property of boron carbide nanowires. *Chinese Phys. B* **17**, 4585-4591 (2008).

174 Huang, Y. *et al.* Fabrication of patterned boron carbide nanowires and their electrical, field emission, and flexibility properties. *Nano Res.* **5**, 896-902 (2012).

175 Yu, Z. *et al.* Correlating Growth Habit of Boron-Rich Low-Dimensional Materials with Defect Structures by Electron Microscopy. *Crystal Growth & Design* **13**, 2269-2276 (2013).

176 Fu, X. & Yuan, J. Cyclic twinning and internal defects of boron-rich nanowires revealed by three-dimensional electron diffraction mapping. *Nanoscale* (2013).

177 Li, D. Y. *et al.* Thermal conductivity of individual silicon nanowires. *Applied Physics Letters* **83**, 2934-2936 (2003).

178 Shi, L. *et al.* Measuring thermal and thermoelectric properties of one-dimensional nanostructures using a microfabricated device. *Journal of Heat Transfer-Transactions of the Asme* **125**, 881-888 (2003).

APPENDIX I: CALCULATION OF THE NORMAL DIRECTION OF THE (001) DEFECT PLANE

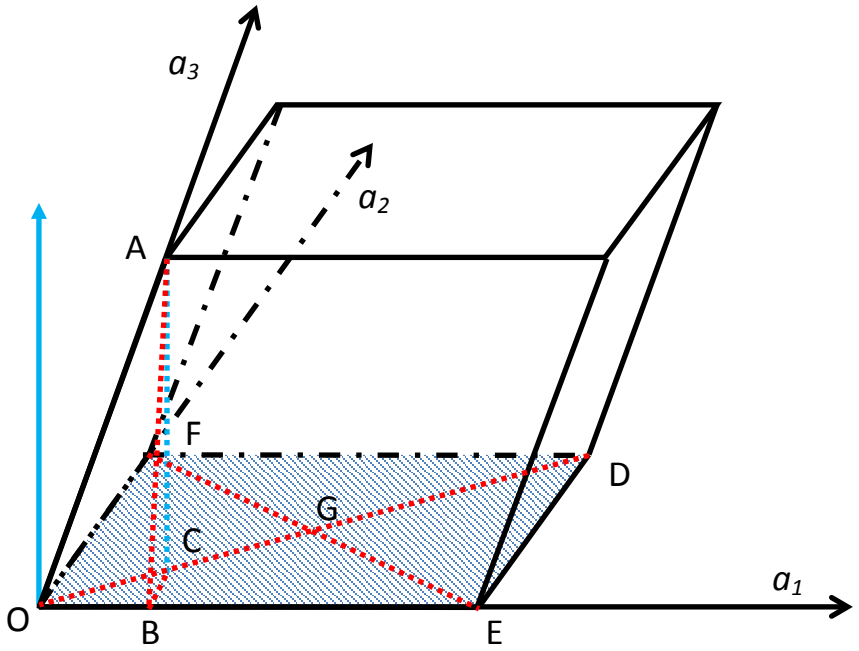

Figure A1 The geometry calculation within the rhombohedral unit cell of boron carbide.

To represent the normal direction ($\overline{\mathrm{CA}}$) in terms of three unit vectors a_1, a_2, and a_3, some dotted lines are added to help the calculation.

OD and *EF* are the diagonals in the bottom (001).

AC is parallel with the normal direction of (001) plane. It intersects *OD* at point *C*.

AB is perpendicular to *OE*, so is *CB*.

In the unit cell,

$$\begin{cases} \mathrm{OF} = \mathrm{OE} = a \\ \angle\mathrm{FOE} = \alpha;\ \angle\mathrm{COB} = \alpha/2 \\ \angle\mathrm{ABO} = \angle\mathrm{ACO} = \angle\mathrm{CBO} = \angle\mathrm{OGE} = 90° \end{cases}$$

We know that

$$\overline{\mathrm{CA}} = \overline{\mathrm{OA}} - \overline{\mathrm{OC}}$$

Since $\overline{\mathrm{OA}}$ is the unit vector, $\overline{\mathrm{OC}}$ is what we are looking for.

In the triangle AOB,

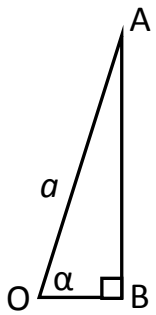

$$\mathrm{OA} = a, \angle ABO = 90°$$

So

$$\mathrm{OB} = a\cos\alpha, AB = a\sin\alpha$$

In the triangle COB,

$$\mathrm{OA} = a, \angle ABO = 90°$$

So

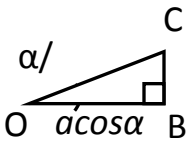

$$\mathrm{OC} = a\cos\alpha/(\cos\alpha/2)$$

Now we know the length of OC, thus its vector can be written as

$$\overline{\mathrm{OC}} = \frac{\left|\overline{\mathrm{OC}}\right|}{\left|\overline{\mathrm{OD}}\right|} \cdot (\overline{a_1} + \overline{a_2}) = \frac{\left|\overline{\mathrm{OC}}\right|}{2\left|\overline{\mathrm{OG}}\right|} \cdot (\overline{a_1} + \overline{a_2})$$

In the triangle OGE

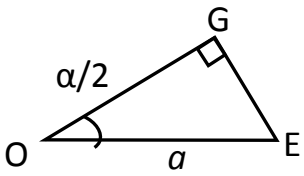

$$\left|\overline{\mathrm{OG}}\right| = a \cdot \cos\frac{\alpha}{2}$$

Then $\overline{\mathrm{OC}}$ can be represented by unit vectors

$$\overline{\mathrm{OC}} = \frac{\cos\alpha}{2\cos^2\frac{\alpha}{2}} \cdot (\overline{a_1} + \overline{a_2})$$

$$\overline{\mathrm{CA}} = \overline{\mathrm{OA}} - \overline{\mathrm{OC}} = \overline{a_3} - \frac{\cos\alpha}{2\cos^2\frac{\alpha}{2}} \cdot (\overline{a_1} + \overline{a_2})$$

So the normal direction is

$$[-\frac{\cos\alpha}{2\cos^2\frac{\alpha}{2}}, -\frac{\cos\alpha}{2\cos^2\frac{\alpha}{2}}, 1]$$

Taking $\alpha = 65.7°$ (based on JCPDS 04-007-1018), the normal direction will be

$$[-0.292, -0.292, 1]$$

APPENDIX II: ILLUSTRATION OF THE GEOMETRICAL ORIENTATIONS OF TF AND AF NANOWIRES ON TEM GRIDS

In practical observation, “in-zone” directions generally are easier to be reached on TF nanowires than AF ones, due to the fact that planar defects are in different orientations inside these nanowires. For TF wires, planar defects are always perpendicular to the preferred growth directions (*i.e.,* axial directions). When a TF nanowire is randomly positioned on the flat support film of a TEM grid, in most cases, its planar defects would be nearly parallel to the incident electron beam, as shown in Figure S6(a). As a result, by only tilting the nanowire with respect to its axial direction, “in-zone” directions can be relatively easily reached. However, for the case of AF nanowires, planar defects are along their axial directions. When an AF nanowire is put on a TEM grid randomly, there are a few chances that the planar defects are right parallel to the electron beam. One extreme example is shown in Figure A2, in which the electron beam is normal to the planar defects. Thus, to reach the “in-zone” directions of an AF nanowire, two steps are necessary. First, have the (001) plane parallel to the electron beam by tilting the nanowire with respect to its axial direction. Second, tilt within the (001) plane to reach the “in-zone” directions. As a result, it is relatively difficult and tedious to reach the “in-zone” directions of AF nanowires than that of TF nanowires.

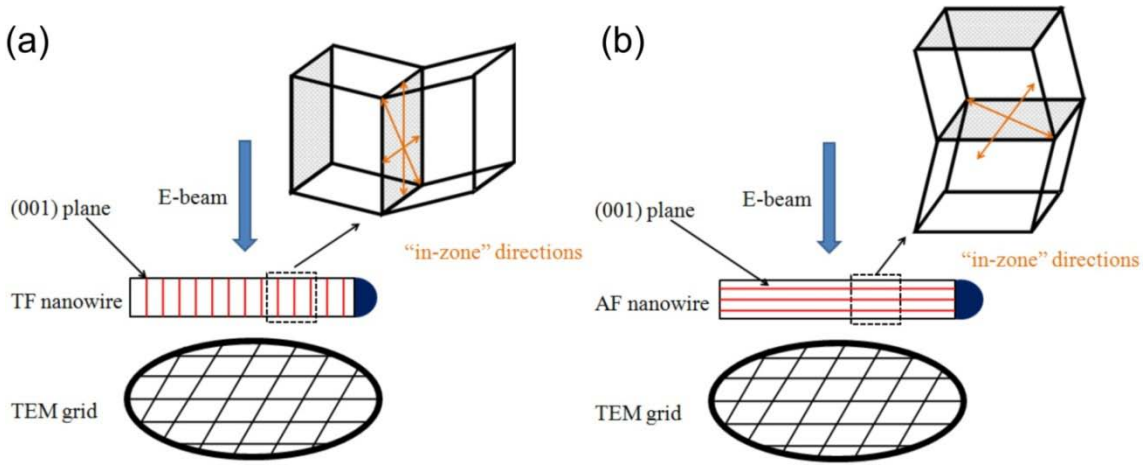

Figure A2 The relation between the incident electron beam and TF and AF nanowire positions on TEM grids

APPENDIX III: DETAILED RESULTS FROM THE TRIPOD-LIKE BRANCHED NANOSTRUCTURES

The tripod-like branched nanostructure discussed in the main paper has transverse faults in all three legs. For the left and right legs, the characteristic features of planar defects were observed, as clearly shown in Figures 5.6 (b) and (c). For the upper leg, no characteristic features were revealed even after a full range of tilting examination. However, a new feature so-called “fused rings” (Figure A3 (a)) was discovered during the titling observation. This new feature has been proved as another indicator of transverse faults.

Figures A3 (b) and (c) are TEM results from another nanowire, demonstrating why “fused rings” is an indicator of transverse faults. Figure A3 (b) presents results recorded from the $[\bar{1}12]$ direction, from which “fused rings” are shown in the image while no other characteristic features of planar defects can be seen. The nanowire was then tilted to the [010] “in-zone” direction as shown in Figure A3 (c), from which the transverse faults are clearly revealed. Based on these results, it is reasonable to say that “fused rings” is one kind of indicators for transverse faults.

Therefore, the upper leg of the tripod-like nanostructure is a TF nanowire.

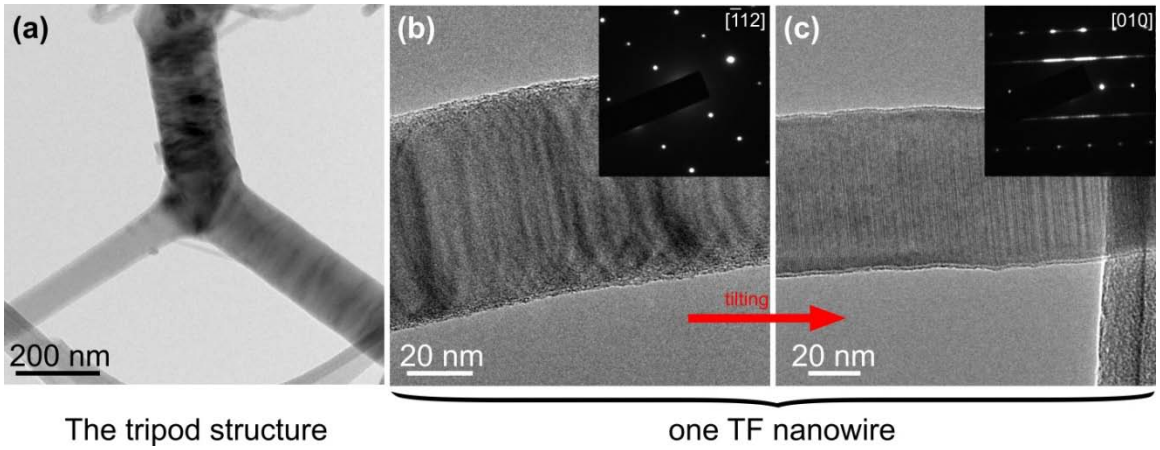

Figure A3 (a) A low magnification TEM image of the tripod-like branched nanostructure discussed in the main paper. At this viewing direction, “fused rings” are observed from the upper and right legs, whereas no special features are seen from the left leg. When viewing from other directions, the characteristic features of planar defects are shown in the left and right legs, as presented in Figure 5.6. Evidence on why “fused rings” is an indicator of transverse faults is presented in (b) and (c). One nanowire originally showing “fused rings” when viewed along the [$\bar{1}$12] direction (b) was tilted to the [010] direction (c), from which the transverse faults are clearly revealed.